University of Alberta

Solids Transport with Turbulent Flow of a Drag Reducing Fluid in the Horizontal Annuli

by

Fabio Ernesto Rodriguez Corredor

A thesis submitted to the Faculty of Graduate Studies and Research
in partial fulfillment of the requirements for the degree of

Master of Science
in
Petroleum Engineering

Civil and Environmental Engineering

Fall 2013
Edmonton, Alberta

ABSTRACT

Fully developed turbulent flow of water and drag reducing fluids through a horizontal flow loop with concentric annular geometry (inner to outer pipe radius ratio = 0.4) was investigated using the Particle Image Velocimetry technique. Experiments were conducted at solvent Reynolds numbers ranged from 17,700 to 66,900. Initially, the study was focused on analyses of the mean flow and turbulence statistics such as near wall velocity profile, Reynolds stress distribution, axial and radial velocity fluctuations, vorticity fluctuations and turbulent kinetic energy budget.

The hole cleaning experiments were also conducted using water and drag reducing fluids. Critical velocities for the initiation of cuttings movement with rolling, saltation/dunes, and suspension modes were determined and compared when using water and drag reducing fluids as a carrier fluid. Critical velocities for the initiation of cuttings movement were found to be lower with water than that of drag reducing fluid in all transport modes.

ACKNOWLEDGEMENTS

I would like to thank my supervisor, Prof. Dr Ergun Kuru, for the patient guidance, encouragement, commitment, immense knowledge, advice and financial support that he has provided throughout my time as his student. His guidance helped me in all the time of research and writing of this thesis.

I would like to thank my lab-mate Majid Bizhani for the immense help he provided me during this research. I would also like to thank Todd Kinnee for all the help and suggestions he gave me during the experiments.

To my family, particularly my parents thank you for your love, support, and unwavering belief in me. Without you, I would not be the person I am today.

Finally, I would like to thank the Natural Sciences and Engineering Research Council of Canada (NSERC RGPAS 411966 KURU and NSERC RGPIN 238623 KURU) for supporting financially this research. I am also thankful to M-I SWACO Canada for providing us the PHPA (Poly Plus RD).

TABLE OF CONTENTS

LIST OF TABLES

LIST OF FIGURES

NOMENCLATURE

a	Inner to outer radius ratio ($=r_1/r_2$)
ρ	Fluid density
D_1	Outer diameter of the inner pipe
D_2	Inner diameter of the outer pipe
d_l	Equivalent diameter
d_p	Particle diameter
d_{50}	Median particle diameter
e_{xy}	Fluctuating strain rate
f	Friction factor
L	Pipe length
P	Pressure
r	Pipe radius
r_o	Radius of zero shear stress
r_m	Radius of maximum velocity
r_1	Outer radius of the inner pipe
r_2	Inner radius of the outer pipe
Res	Solvent Reynolds number
Re^*	Modified Reynolds number
τ_A	Weighted average wall shear stress
τ_{xy}	Total shear stress
τ_{xy}^s	Solvent shear stress
τ_{xy}^p	Polymer shear stress
U	Bulk velocity
u	Actual velocity in the x direction

u'	Fluctuation velocity in the x direction
$\bar{u}$	Time average velocity in the x direction
u_τ	Shear velocity
v	Actual velocity in the y direction
v'	Fluctuation velocity in the y direction
$\bar{v}$	Time average velocity in the y direction
u^*	Friction velocity
u^+	Dimensionless velocity
ω_{xy}	Vorticity in the xy plane
y	Distance from the wall
y^+	Dimensionless Distance from the wall
Δx	Tracer displacement in the x direction
Δy	Tracer displacement in the y direction
Δt	Time between two laser illuminations
ΔP_s	Pressure drop for only solvent
ΔP_p	Pressure drop for polymer solution
$\%DR$	Percentage of drag reduction
$\emptyset$	Geometric shape factor
μ	Fluid viscosity
ϑ	Kinematic viscosity of the solvent
γ_{xy}	Fluctuation velocity gradient tensor

1 INTRODUCTION

1.1 Overview

The flow of fluids through pipes and annular spaces is commonly experienced in the oil and gas well drilling and well completion operations. High frictional pressure losses are anticipated when drilling long horizontal and extended reach wells causing operational problems (i.e., pipe stuck, lost circulation, etc.) as well as high pumping costs . Therefore, efforts are commonly spent to minimize frictional pressure losses as part of the requirements of optimum drilling hydraulic design [1].

Use of polymer additives in well fluids has been proven to be an effective strategy to reduce frictional pressure losses [2], in particular, when drilling long horizontal and extended reach wells where the circulating system pressure losses are extremely high. However, addition of the drag reducer to the drilling fluid may interfere with some other functions of drilling fluids such as solids removal performance.

When analyzing the drag reduction phenomenon in concentric annulus, it is necessary to study the effect of adding drag reducers on the velocity profile, second order statistics (turbulent intensities and Reynolds stresses), mean vorticity and root mean square (rms) of vorticity, in order to be able to better explain why drag reduction is taking place [3]. Many experimental studies analyzing drag reduction phenomenon in channel and pipe flow have been presented in the past; however, only few experimental work has been reported for the annular geometry case [4].

In the past, intrusive techniques such as the hot wire anemometry have been commonly used to study turbulent flow through concentric annulus, [5]. Other experimental

techniques such as laser doppler anemometry has also been used to study turbulent of Newtonian and drag reducer fluid through concentric annulus [6]. Particle Image Velocimetry (PIV) technique has been successfully used for different fluid dynamics applications [7]. One of the main advantages of PIV is being a non-intrusive technique; therefore, data can be collected without disturbing the flow in the flow area generated by the measurements techniques instruments [7]. PIV has not been used to study turbulent flow of Newtonian and drag reducing fluids in annular geometry yet.

In this study, the nature of turbulent flow through horizontal concentric annulus is experimentally analyzed using the particle image velocimetry (PIV) technique. The influence of adding drag reducer additives on the nature of turbulence is analyzed. The velocity profile, second order turbulence statistics, mean vorticity and rms of vorticity in the region close to the inner and outer walls are presented.

When drilling horizontal and extended reach wells, effective transport of drilled solids becomes a challenge. Insufficient cutting transport can result in stuck pipe problems, early bit wear, slow drilling rate, high drag and force and fracture of the formation. The efficiency of solids removal in any drilling operations depends upon many factors such as nature of the fluid used, particle diameter and density, and wellbore geometry [8].

In order to analyze the influence of using drag reducing additives on the solids transport performance, an experimental study involving different particles diameters and fluids with different drag reducing polymer concentrations, and horizontal concentric annular geometry have been conducted.

1.2 Statement of the Problem

Drag reduction only occurs when the flow is in turbulent regime [9]. Therefore, the study of turbulent flow is required. Many experimental studies have been conducted to analyze the turbulent flow in horizontal concentric annulus. Yet, there are still many unanswered questions regarding the nature of the turbulent flow in the annular geometry. For example, there is no consensus on questions such as whether the position of maximum velocity and zero shear stress coincide at the same radial location or not. Additionally, it is not clear if the characteristics of the velocity profile in the logarithmic zone follow the log law explained by Bernard and Wallace [10] for pipe flow. Also, it is not clear if the velocity profile is identical at both inner and outer walls.

Experimentally, Brighton and Jones et al. [5] and Kjellstrom and Hedberg et al. [11] shown that the position of maximum velocity and zero shear did coincide at the same radial location. Boersma and Breugem et al. [12] also reached the same conclusion using direct numerical simulations (DNS).

On the other hand, Lawn and Elliott et al. [13], Rehme [14], and Nouri et al. [15] provided experimental data showing that the radial location of maximum velocity and zero shear stress did not coincide at the same point. Chung et al. [16] and Ould–Rouiss et al. [17] also provided supporting data in this respect by using direct numerical simulations (DNS).

Clearly, there is no consensus on the question of whether the radial location of maximum velocity and zero shear stress coincide at the same radial point or not. Therefore, more experimental data, perhaps using different experimental techniques than that of used in the past studies, would be helpful to answer the question in this respect.

Previous experimental studies have been conducted using experimental techniques such as double pitot-tube, hot wire anemometry, and laser doppler anemometry. The use of particle image velocimetry (PIV) to measure velocity distribution in horizontal concentric annuli is novel in this sense that it has not been used before for this type of flow geometry.

Additionally, some of the characteristic properties of the turbulent flow such as mean vorticity, rms of vorticity and turbulent kinetic energy budget, have not been analyzed in details for the case of concentric annulus yet.

Few experimental works have been conducted in the past to study the drag reduction phenomenon in concentric annulus (Japper-Jaafar et al., [6] and Escudier et al. [18]). Japper-Jaafar et al., [6] studied the effect of adding drag reducers on the velocity profile, turbulent intensities and Reynolds stresses. However, they did not provide any results showing the influence of adding drag reducer on the location of maximum velocity, mean vorticity, rms of vorticity and turbulent kinetic energy budget for the case of concentric annulus.

When adding drag reducing polymer to the drilling fluid, a benefit of decreasing the frictional pressure drop is obtained. However, the drag reducing fluid may have some secondary effects on the solids transport. Therefore, cuttings transport performance of drag reducing fluids when flowing through annular geometries should be analyzed and quantified.

Many studies have been conducted in the past for cuttings transport in pipes and annular spaces (Ramadan et al., [19], Clark [20], Lasen et al [21], Duan et al [22], Gao et al [23], among others. However, questions still exist such as under which circumstances the particles movement is initiated and also what kind of particles are removed easier, the

finer or the coarser particles? Therefore, it is necessary to provide more experimental data, showing the effect of changing parameters such as particle diameter, nature of the fluid (drag reducing fluid versus water) and viscosity on the solids transport performance in horizontal annular geometries.

1.3 Objectives of the Research

The objectives of the present research are summarized as follows:

- Conduct an experimental study of turbulent flow of water and drag reducing fluids through horizontal concentric annulus. In particular, analyze the second order turbulence statistics (turbulent intensities and Reynolds stresses), mean vorticity, rms of vorticity and turbulent kinetic energy budget in the region close to the inner and outer walls.
- Develop an experimental procedure for using Particle Image Velocimetry (PIV) Technique to measure the velocity profile in the whole annular space and in the region close to the inner and outer walls during turbulent water and drag reducing polymer fluid flow through horizontal concentric annulus.
- Study the drag reduction phenomenon through horizontal concentric annulus. Conduct experiments to find the optimum drag reducer concentration which would yield the lowest frictional pressure drop.
- Experimentally study the effect of using drag reducer additives on the turbulence nature ; i.e., position of maximum velocity, velocity profile in the whole annular space and close to the pipe walls, second order turbulence statistics, mean vorticity, rms of vorticity and turbulent kinetic energy budget)
- Conduct solids transport experiments to compare the solids transport performances of water and drag reducing polymer fluid.

- Identify the various flow patterns under which the solids are transported using water and drag reducing fluid.
- Determine the critical velocity to initiate particle movement when water and drag reducing fluid are used to remove particles of two different mean particle diameters (coarse versus fine particle).

1.4 Methodology

An experimental study has been conducted to achieve research objectives.

Particle image velocimetry (PIV) technique was the main tool used to obtain velocity measurements which were essential for all turbulent flow analyses. Some factors should be considered when implementing the PIV technique. First of all, both pipe walls and fluids need to be totally transparent. Therefore, the horizontal flow loop made of clear colorless Borosilicate glass pipes was used. Additionally, in order to minimize the distortion of light at the pipe walls, the use of a fluid with a refractive index similar to the refractive index of the glass is necessary. A rectangular box surrounding the pipes in the test section is filled up with glycerin to minimize the light distortion

Literature review reveals that there exist some very effective drag reducers which can result giving drag reduction as high as 80% [24]. However, in order to use the PIV technique, the fluid should be transparent. Therefore, a fluid meeting the transparency requirement and drag reduction effectiveness needs to be used. For this research, a commercially available high molecular weight partially hydrolyzed polyacrylamide (PHPA) giving a drag reduction up to 40% in the concentric annular geometry was used.

Moreover, PIV requires the use of seed particles as tracer. Seed particles should have the density same as the fluid density so that they can be tracked as the representative of fluid

particle movement. In this research, hallow glass spheres with a density equal to 1.1±0.5 g/cc and mean diameter of 10 microns are used.

In order to find the optimum concentration of drag reducer, the fluid flow rate and the associated frictional pressure drop were measured.

When analyzing the particle removal performance in concentric annulus, a film photographic system is required. This allowed us to monitor the particle movement at each flow velocity tested. Additionally, a light contrast between the particles and the fluid was required in order to have a better view of the particle movement. Therefore, a photography tool such as the professional quartz light was used.

Finally, as established in the last objective of this research, two different particle diameters were tested in the solids transport experiments. The particles should have the same physical properties in order to be able to compare the results obtained by using each particle diameter. Therefore, quartz particles with the same density and same shape were used in this study.

1.5 Contribution of the Present Research

In the statement of the problem, it was discussed that there is no consensus about radial location of maximum velocity and zero shear stress in turbulent flow through horizontal concentric annulus. All the experimental data provided previously have been acquired by means of measurement techniques such as hot wire anemometry and laser Doppler anemometry LDA. This study provides more experimental data to the discussion using a different measurement technique, which is the particle image velocimetry (PIV) technique. It was the first time that PIV technique was used to study the turbulent flow through concentric annulus.

Detailed turbulence analyses such as the mean vorticity, rms of vorticity, and turbulent kinetic energy budget that have not been provided in the past for the flow in concentric annulus geometry are provided. .

New experimental data on the effect of adding drag reducer on the nature of turbulence is provided. More specifically, experimental analyses of the effect of adding drag reducers on the velocity profile, location of maximum velocity, second order turbulence statistics (turbulent intensities and Reynolds stresses), mean vorticity, rms of vorticity and turbulent kinetic energy budget are presented. Moreover, the optimum concentration, which is the concentration yielding to the lowest pressure drop is found in this study.

Finally, this study provides some new data showing the influence of adding drag reducers on the critical velocity to commence particle movement, flow patterns, pressure drops and dunes velocity.

1.6 Structure of the Thesis

Chapter 1: An overview, statement of the problem, thesis objectives, methodology and contribution of the research to the literature are presented in this chapter.

Chapter 2: This chapter includes the description of the experimental flow loop facilities and associated equipment. Additionally, a description of the PIV equipment components and film photography system is presented in this chapter.

Chapter 3: This chapter describes the particle image velocimetry (PIV) data acquisition and processing. PIV calibration and direct cross correlation method used to calculate the vector field are described. Additionally, the subsequent PIV post-processing and fluctuation field calculations are described in this chapter.

Chapter 4: This chapter is focused to analyze the water turbulent flow in concentric annulus. Data showing the position of maximum velocity and zero shear stress at different Reynolds numbers is presented. Moreover, velocity profiles, turbulence second order statistics, mean vorticity, rms of vorticity and turbulent kinetic energy budget close to the inner and outer walls are presented.

Chapter 5: Pressure drop, friction factors and PIV measurements for water and drag reducing fluid are presented in this chapter. Data showing the effect of adding drag reducer on the velocity profiles, second order turbulence statistics, mean vorticity, rms of vorticity and turbulent kinetic energy budget close to the inner and outer walls are presented.

Chapter 6: Solids transport experiments showing the effect of adding drag reducer on the critical velocity to commence particle movement, flow patterns, pressure drops and dunes velocity are also presented.

Chapter 7: This chapter presents conclusions of the research and the recommendations for future work.

1.7 References

[1] Ercan, C., and Ozbayoglu M.E., 2009, ""PHPA" as a Frictional Pressure Reducer and its Pressure Loss Estimation," *SPE/IADC middle east drilling theology conference & exhibition*, Manama, Bahrain.

[2] Shah, S.N., Kamel, A., and Zhou., 2006, "Drag reduction characteristics in straight and coiled tubing — An experimental study," *Journal of Petroleum Science and Engineering*, 53, 179–188.

[3] Ptasinski, P.K., Nieuwstadt, F.T.M., Van den brule, B.H.A.A., and Hulsen, M.A., 2001, "Experiments in Turbulent Pipe Flow with Polymer Additives at Maximum Drag Reduction," J. *Flow, Turbulence and Combustion*, 66, pp. 159–182.

[4] Rodriguez-Corredor, F.E., Bizhani, M., and Kuru, E., 2013, "An experimental study of the effect of drag reducing additive on the structure of turbulence in concentric annular pipe flow using particle image velocimetry technique," ASME 2013 International Mechanical Engineering Congress & Exposition (IMECE), Technical paper. San Diego, California, US.

[5] Brighton, J.A. and Jones, J.B., 1964, "Fully developed turbulent flow in annuli," J. Basic Eng, D86, pp. 835.

[6] Japper-Jaafar, A., Escudier, M.P., and Poole, R.J., 2010, "Laminar, transitional and turbulent annular flow of drag-reducing polymer solutions," J. Non-Newtonian Fluid Mech, 165, pp. 1357–1372.

[7] Zeinali, H., 2012, "Effect of Near-wall Turbulence on Selective Removal of Particles from Sand Beds Deposited in Pipelines," Ph.D. thesis, University of Alberta, Edmonton, Canada.

[8] Goharzadeh, A., Rodgers, P., and Touati, C., 2008, "Influence Of Slug Flow on Hydraulic Sand Dune Migration in Horizontal Pipelines," Proceedings of ASME 2008 International Mechanical Engineering Congress & Exposition, Boston, Massachusetts, USA.

[9] Virk, P.S., 1975, "Drag reduction fundamentals," AIChE J. 21, 625–656.

[10] Bernard, P.S., Wallace, J.M., 2002, "Turbulent Flow, Analysis, Measurement and Prediction," John Wiley & Sons, New Jersey, U.S, Chap 4.

[11] Kjellstrom, B., and Hedberg, S., 1966, " On Shear Stress Distributions for Flow in Smooth or Partially Rough Annuli," Technical Report AE-243, Aktiebolaget Atomenergie, Stockholm, Sweden.

[12] Boersma, B.J.,Breugem, W. P, 2011, "Numerical Simulation of Turbulent Flow in Concentric Annuli," Flow Turbulence Combustion, 86, pp. 113-117.

[13] Lawn, C.J., and Elliott, C.J., 1972, "Fully Developed Turbulent Flow Through Concentric Annuli," J. of Mechanical Eng. Science, 14(3), pp. 195-204.

[14] Nouri, J.M., Umur, H., Whitelaw, J.H., 1993, "Flow of Newtonian and non-Newtonian Fluids in concentric and eccentric annuli," J. Fluid Mech., 253, pp. 617-641.

[15] Chung, S.Y., Rhee, G.H., Sung, H.J., 2002, "Direct numerical simulation of turbulent concentric annular pipe flow Part 1: Flow field," Int. J. Heat and Fluid Flow, 23, pp. 426-440.

[16] Ould-Rouiss, M., Redjem-saad, L., and Lauriat, G., 2009, "Direct numerical simulation of turbulent heat transfer in annuli: Effect of heat flux ratio," International Journal of Heat and Fluid Flow, 30, pp. 579-589.

[17] Escudier, M. P., Gouldson, I. W., and Jones D. M., 1995, "Flow of shear-thinning fluids in a concentric annulus," Experiments in Fluids, 18, pp. 225–238.

[18] Ramadan, A., Skalle, P., and Johansen, S.T., 2003, "A Mechanistic model to determine the critical flow velocity required to initiate the movement of spherical bed particles in inclined channels," Chemical Engineering Science, 58 pp. 2153-2263.

[19] Clark, R.K and Bickham, K.L., 1994, "A Mechanistic Model for Cuttings Transport," Proceedings of the 1999 SPE 69th Annual Technical Conference and Exhibition, New Orleans, LA, USA.

[20] Larsen, T.I., Pilehvari, A.A., and Azar, J.J., 1997, "Development of a New Cuttings-Transport Model for High-Angle Wellbores Including Horizontal Wells," *SPE Journal of Drilling & Completion*, V(2), Number 2, 129-136.

[21] Duan, M., Miska, M., Yu, M., Takach, N., Ahmed, R., and Zettner, C., 2008, "Transport of Small Cuttings in Extended-Reach Drilling," *SPE Journal of Drilling & Completion*, V(23), Number 3, 258-265.

[22] Gao E., and Young, A.C., 1995, "Hole Cleaning in Extended Reach Wells: Field Experience using and Theoretical Analysis Using a Pseudo-Oil (Acetal) Based Mud," SPE/IADC Drilling Conference, Amsterdam. DOI: 10.2118/29425-MS.

[23] Kamel, A., and Shah, S.N., 2009, "Effects of salinity and temperature on drag reduction characteristics of polymers in straight circular pipes," *Journal of Petroleum Science and Engineering*, 67, 23–33.

2 EXPERIMENTAL FACILITIES

All the experiments were conducted in a horizontal flow loop facility with concentric annular geometry. Two types of experiments were conducted: i-) Turbulent flow of water and drag reducing fluid in concentric annuli where Particle Image Velocimetry (PIV) system was used to measure velocity distribution and, ii-) solids transport experiments. This chapter is dedicated to describe flow loop facility, materials and other related equipments used in the experimental program.

2.1 Description of the Main Components of the Flow Loop

A picture showing the general view of the facility is shown in figure 2-1. A schematic showing the individual equipment associated with flow-loop is shown in figure 2-2. The horizontal annular section has a total length of 9 meters. This section is composed of high quality, optic grade glass tubes connected by specially designed joints to ensure smooth wall. The inner diameter of the outer pipes is 95 mm and the outer diameter of the inner pipes is 38 mm. The inner to outer wall radius ratio for this study is equal to 0.4 and the hydraulic diameter obtained is 57 mm. The pipes are made of clear colorless Borosilicate glass. The refractive index at 532 nm wavelength is 1.47. To minimize sagging and vibration of the inner pipe, the proper pipe wall thickness was selected.

The test fluids (water and the aqueous polymer solution) are stored in a mixing tank with a total capacity of 500 liters. The fluid is circulated through the loop using a centrifugal pump equipped with a variable frequency drive (VFD). A picture of the pump and the mixing tank is presented in figure 2-3.

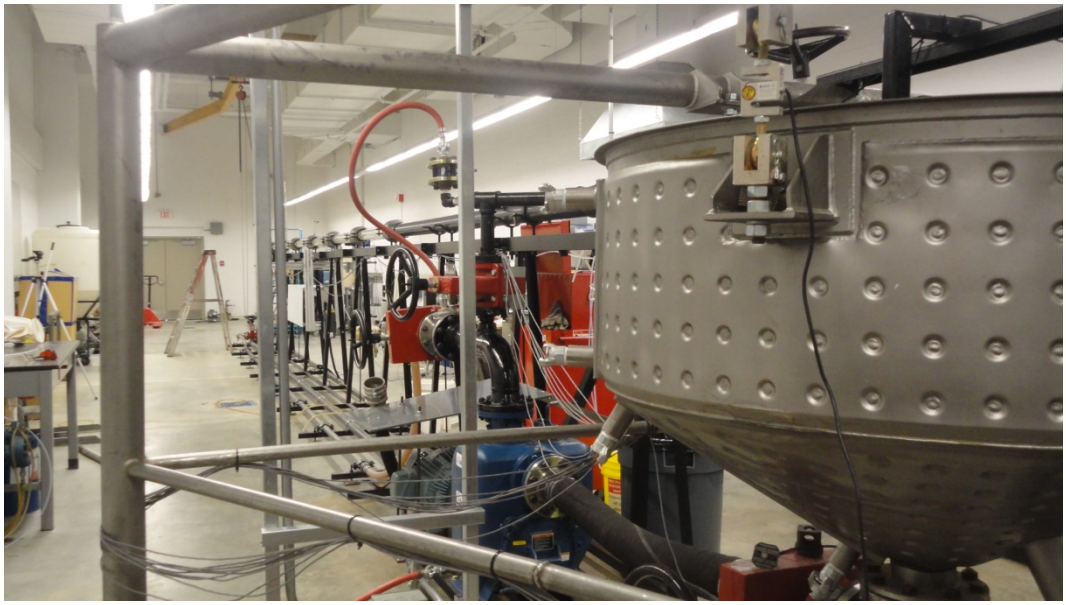

Figure 2 - 1. Picture of the Flow Loop Facility

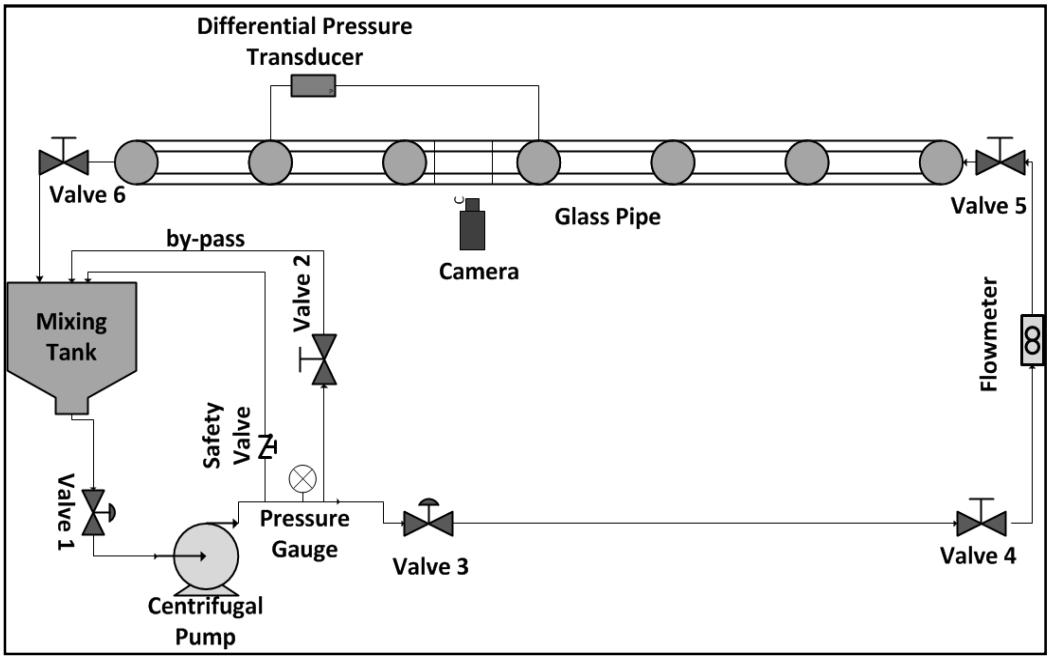

Figure 2 - 2. Schematic of the Flow Loop Facility

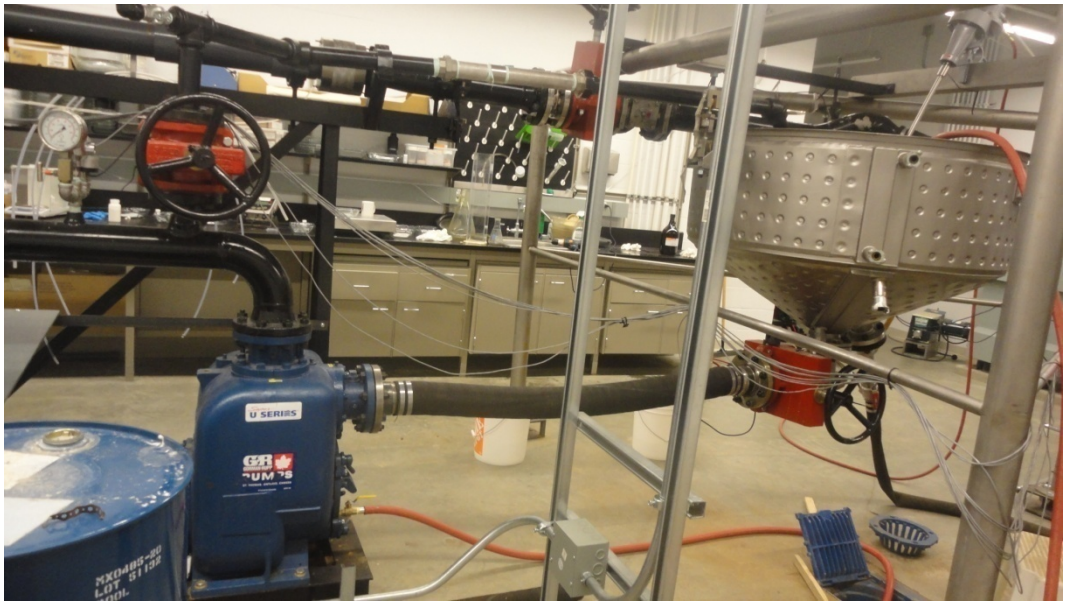

Figure 2 - 3. Pump and Mixing Tank in Place

A magnetic flowmeter is installed at the inlet of the horizontal annular section for measuring the flow rate. The pressure drop along the flow loop is measured using a differential pressure transducer (Omega PX769) acting over 3.0 meters. The differential pressure transducer has a range of 0 to 1500 Pa with a nominal accuracy of ±0.17%. Probes of the differential pressure transducer are located at distances of 5.5 and 8.5 meters away from the inlet (>88 hydraulic diameters). A picture of the flow loop section showing the location of the pressure transducer's probes is presented in figure 2-4. The distance of 88 hydraulic diameters from the inlet is assumed to be sufficiently long to eliminate the end effect and allow turbulent flow to be fully developed. This calculation was performed using the criteria suggested by earlier studies [1,2]. All the data such as pressure drop, flow rate, atmospheric and fluid temperature are recorded by a computerized data acquisition system equipped with Labview software provided by National Instruments.

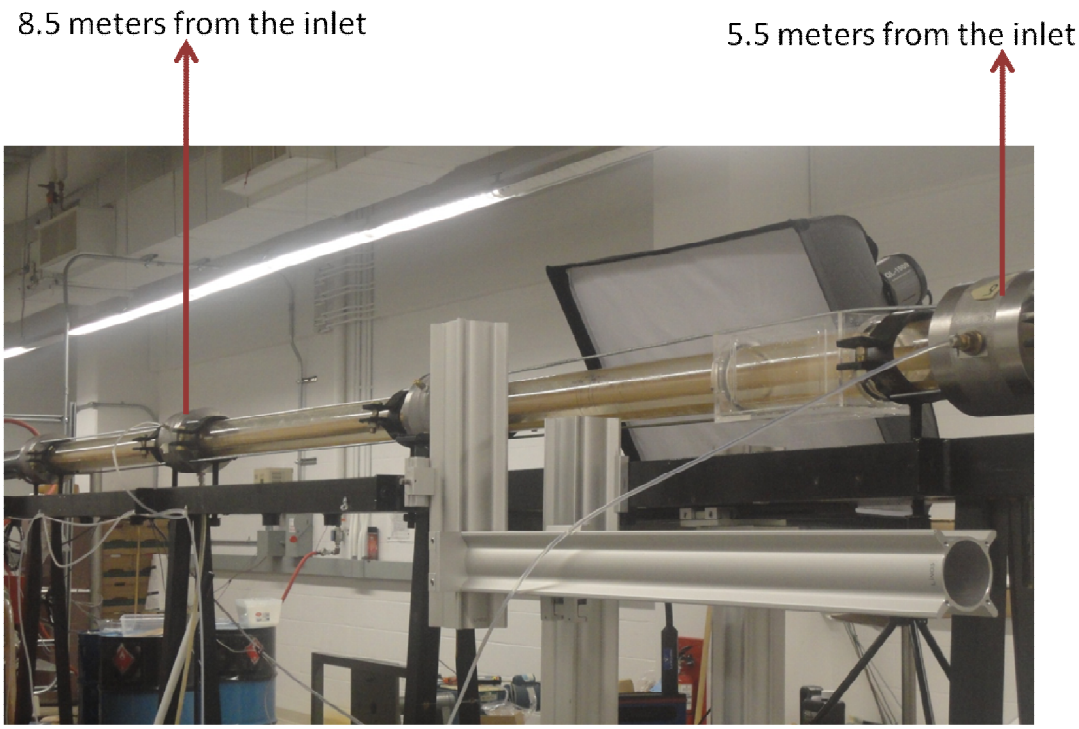

Figure 2 - 4. Flow Loop Section with Pressure Transducer's probes in Place

2.2 Description of the Main Components of Particle Image Velocimetry (PIV) System

All the PIV measurements were taken at 5.5 meters from the inlet (100 hydraulic diameters). At this location, an observation window was installed. The observation window is consisting of a rectangular box surrounding the circular pipe. In order to minimize dispersion and refraction of the laser beams, the box is filled up with glycerin, which has a refractive index value very similar to the glass pipe. This helps to decrease the distortion of the pictures especially in the zone close to the pipe wall. The refractive index value of glycerin is 1.46991. A picture of the observation window is presented in figure 2-5.

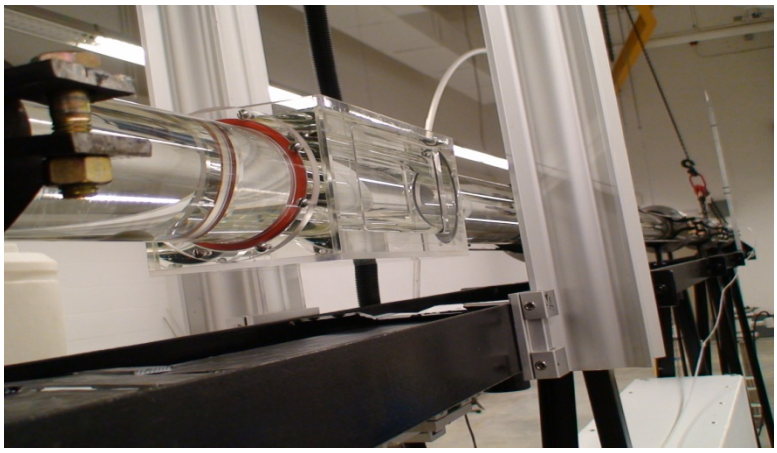

Figure 2 - 5. Observation Window in Place

The PIV components (camera and laser) are connected to the PIV computer provided by LaVision. This computer has installed the software Davis 7.2, which is used to control camera and laser, record the images and process the data. The proper positioning of the camera and the laser is shown in figure 2-6.

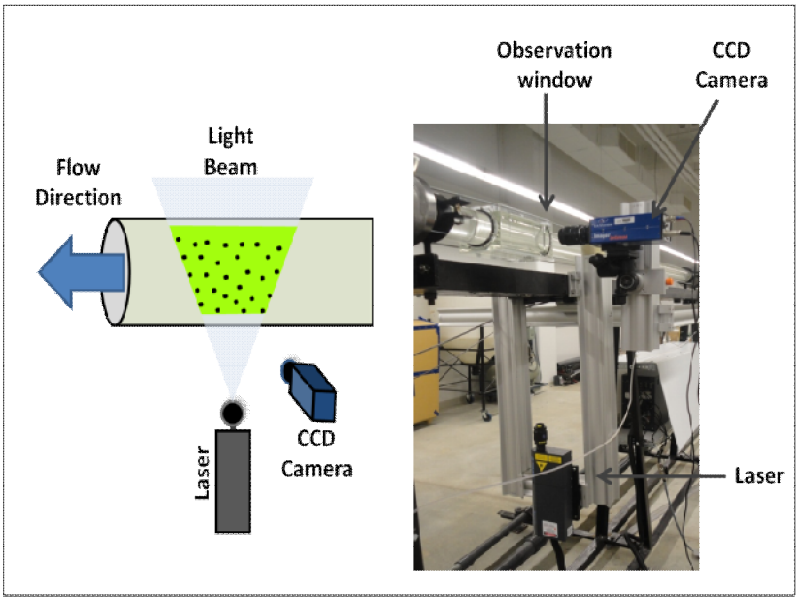

Figure 2 - 6. Test Section with PIV Setup in Place [3].

The laser sheet should be oriented parallel to the highest component of the velocity vector and the camera should be normal to the plane of the laser sheet [4]. For this study, the laser is installed underneath the pipeline. The vertical laser sheet is located horizontally in the center of the pipes and therefore, the camera is installed in front of the observation window making a 90º angle with the laser sheet plane. Since the 2D-PIV technique evaluates instantaneous fluid velocities by measuring the displacement of tracers suspended within the flowing fluid, three different components are required. These components are a light source (laser), tracers (seed particles) and a camera [5]. The laser produces two illuminations in a small interval of time while the camera captures the displacement of the tracers during this time [5].

The camera used is a CCD imager intense camera provided by LaVision. This is a high resolution, high sensitive camera which in double shutter mode can capture a pair of images in a time as short as 500 ns. The exposure time is adjustable by using software and can be varied between 500 ns and 1ms [6]. The camera has a framing of 5 frames/second and a 12 bit CCD sensor with a resolution of 1376 x 1040 pixels [6]. The micro, Nikon AF Micro-Nikkor 60 mm, f/2.8 lens equipped with a 30 mm extension tube was installed to the camera. This configuration allows us to obtain a field of view (FOV) equal to 10 x10 mm^2. In order to find the location of maximum velocity and the Reynolds stress distribution in the whole annular gap, the normal, Nikon AF Nikkor 50mm 1:1.4D was installed to the camera.

The laser used was a 50 mJ double pulsed Nd:YAG laser solo PIV. The laser beam thickness is adjustable and in this case it is kept at the minimum value of 0.5 mm. The light produced is a pulsed green beam. It has a wavelength equal to 532 nm and it is produced at a repetition rate of 50 Hz [7]. The error related to the laser beam thickness is insignificant. This can be explained taking into account that in this specific 2D

application, the highest fluctuations in the flow occurs in the axial and radial direction. Also, because after adjusting the camera and fixing the focal length, the camera only captures particles on a single plane. This may result in appearance of out of focus particles. However, they are not counted in the cross correlation calculation, as they are removed during the image processing.

Glass hallow spheres were used as a tracers. These particles have a white powder appearance and a density equal to 1.1±0.5 g/cc. The mean diameter of the particles is 10 microns. The Stokes number was found to be 0.019 for the worst case scenario. This calculation was done following the suggestions of Marchioli et al. [8]. Since this value is much less than one, the interaction between the particles and the flow is high. Therefore, the particles will represent the flow behavior properly.

2.3 Additional Equipment Used for Solids Transport Experiments

As in the PIV measurements case, the film photography system used to perform the solids transport experiments was installed at 5.5 meters from the inlet to allow the flow to become totally developed. Figure 2-7 shows the film photography system in place. The system is composed of a high definition camera and a professional quartz light (QL-1000). The professional quartz light is used to guarantee uniform background in the field of view and high contracts between the background and the bed of particles. The camera used is a Handycam Camcorder HDR-SR5 Sony Camera. The camera has a Carl Zeiss Vario-Sonnar T lens (10x Zoom lens, 5.1mm - 51mm, F/1.8-2.9) and a 1/3" ClearVid™ CMOS Sensor which allows us to record videos at 1080i HD (1,440x1,080 pixels).

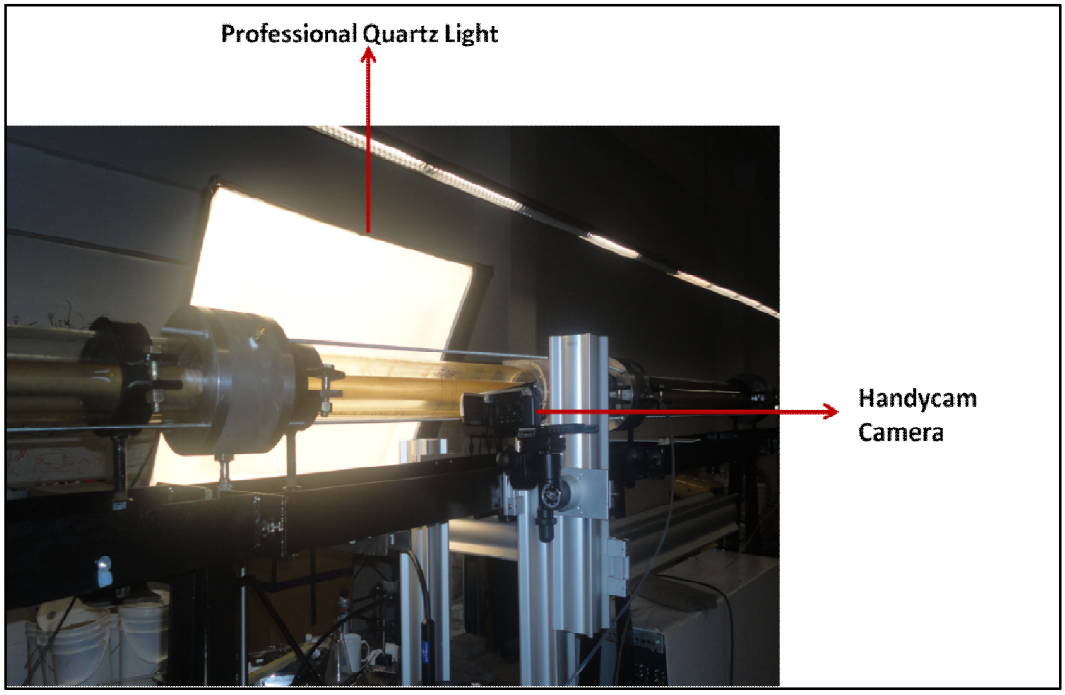

Figure 2 - 7. Film Photography System in Place.

2.4 References

[1] Poole, R.J., 2010, "Development-Length Requirements for Fully Developed Laminar flow in Concentric Annuli," J. Fluids Engineering, 132, pp. 64501:1-4.

[2] Munson, B.R., Young, D.F and Okiishi, T.H., 2002, "Fundamentals of Fluid Mechanics," 4th. ed., John Wiley and Sons, Inc.

[3] LaVision., "Flow Master," Product Catalogue, 2006.

[4] LaVision. "Flow Master Getting Started," Product manual ,2006.

[5] Nezu, I., and Sanjou, M., 2011, "PIV and PTV measurements in hydro-sciences with focus on turbulent open-channel flows," Journal of Hydroenvironment Research, 5, pp. 215-230.

[6] LaVision., "Imager intense. Product catalogue," 2006.

[7] Solo PIV., 2003, "Nd:YAG Laser System," Operator's Manual.

[8] Marchioli, C., Armenio, C., Salvetti, M.V., and Soldati, A., 2006, “Mechanisms for deposition and resuspension of heavy particles in turbulent flow over wavy interfaces,” Physics of fluids, 18, 025102.

3 METHODOLOGY OF PARTICLE IMAGE VELOCIMETRY (PIV) DATA

3.1 Acquisition and Analysis

PIV system was used to acquire 2-D velocity distribution in annular space required for turbulent flow analyses. Calibration of PIV measurements, methodology of PIV data acquisition and analysis are discussed in the following sections.

3.2 Calibration of PIV Measurements

The raw images obtained by PIV camera must be scaled and also need to be corrected based on a spatial calibration in order to remove image distortions generated by camera lens errors and perspective projections [1]. Therefore, a grid of equidistant dots with the same diameter is used as calibration target. The dots are white with a diameter of 0.8mm and the distance between dots is 1.5 mm. The background of the calibration grid is black. After adjusting the camera lens and light, the Field of View (FOV) is kept constant and the calibration target is placed in the light beam plane. After that, a picture of the target is acquired as shown in figure 3-1.

Using Davis 7.2 a reference dot is identified and its neighbours to the right and to the top as well. Finally, the program itself finds the rest of the dots in the picture as shown in figure 3-2.

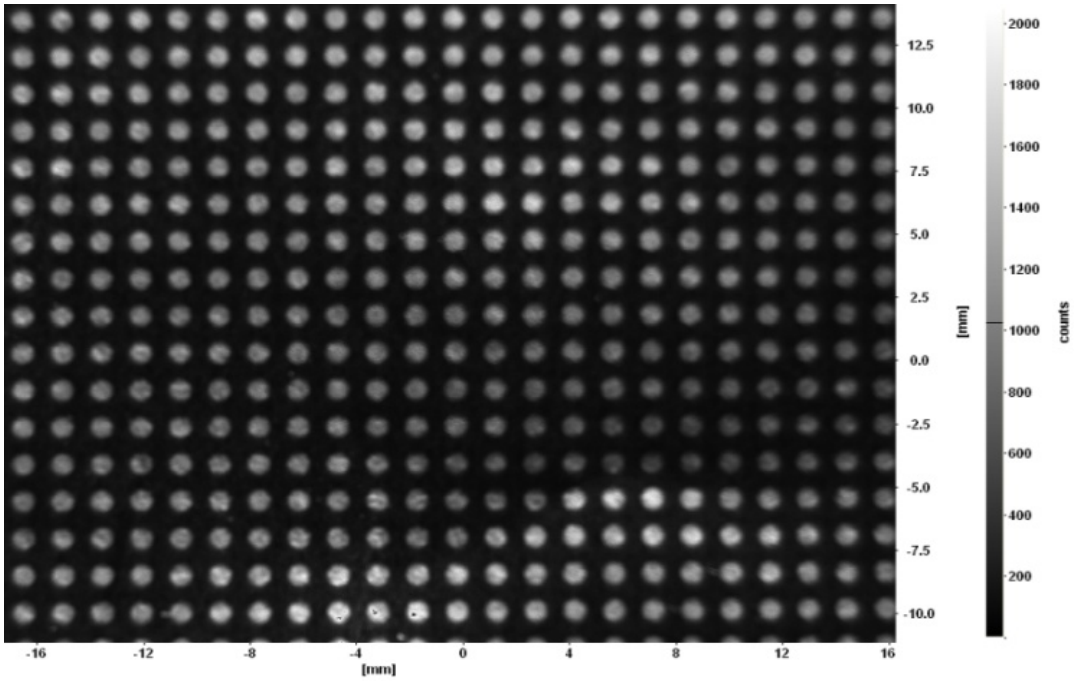

Figure 3 - 1. Picture of the Calibration Target.

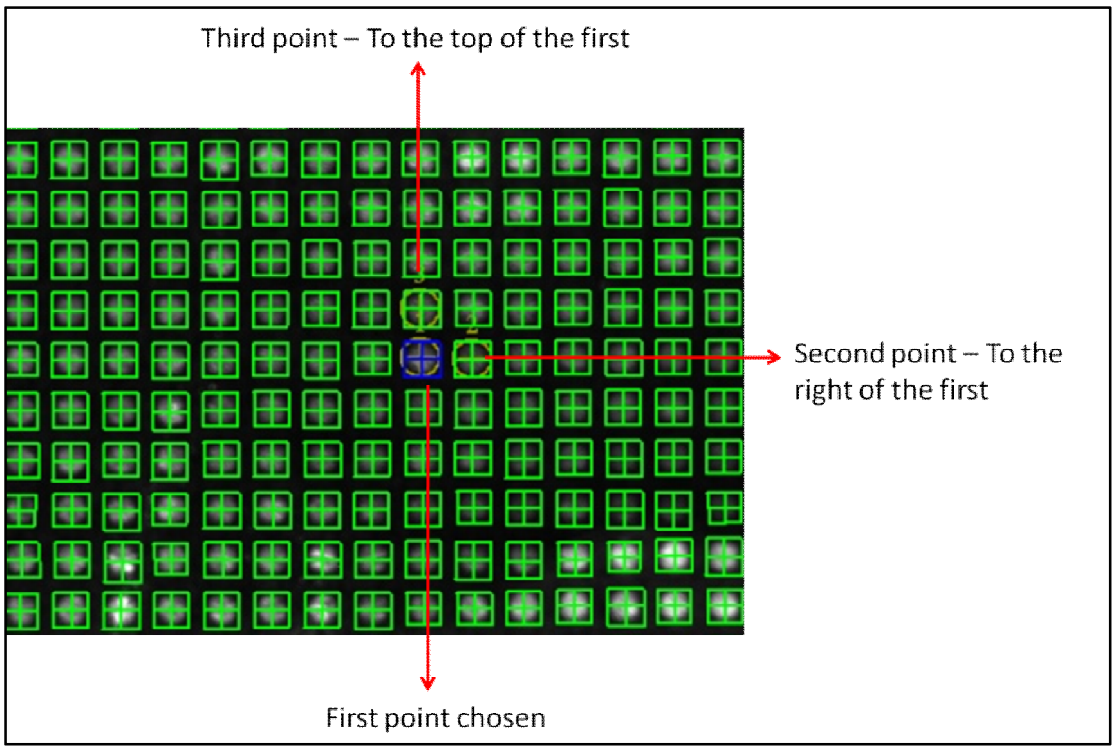

Figure 3 - 2. Initial Dot Definition and Final Dot Detection.

The calibration is performed based on the number and the distance between dots and the dimension of the total FOV is obtained as shown in figure 3-3 [1].

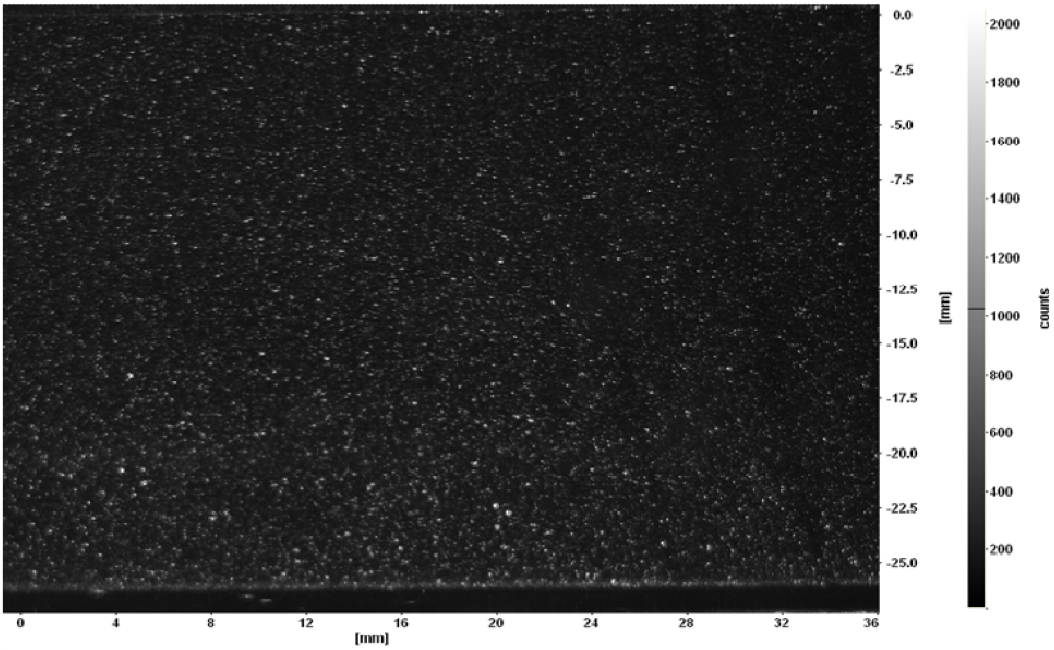

Figure 3 - 3. Final Picture Scaled

3.3 PIV Data Processing

The velocity fields are calculated using Direct Cross Correlation Method. This method is based on the concept of velocity [2]:

$$u = \frac{\Delta x}{\Delta t} \tag{3}$$

$$v = \frac{\Delta y}{\Delta t} \tag{4}$$

The laser produces two illuminations in a very small interval of time (Δt), during this time the displacement in the x direction (Δx) and the y direction (Δy) of the particles are recorded by the CCD camera.

The displacement of the particles is calculated using the FFT (Fast Fourier Transform) based cross correlation of two corresponding interrogation windows. This is included in the software Davis 7.2. As shown in figure 3-4, the image is divided in small interrogation windows; then, the highest peak which represents the main displacement in each particular window is calculated and finally, the velocity field is obtained [3].

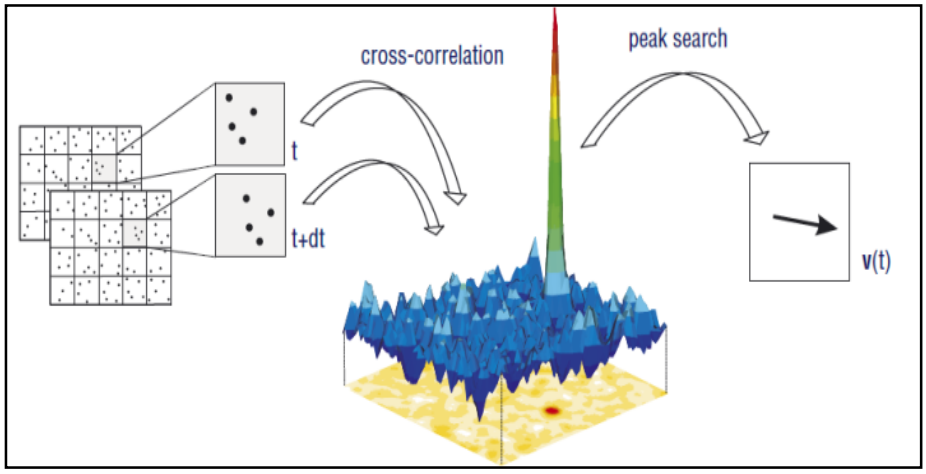

Figure 3 - 4. Scheme of FFT-based cross correlation (Taken from Lavision Catalogue) [3].

In this research, a double pass with a 50% overlap scheme was implemented. The FOV was initially divided into small interrogation windows of 64 x 64 pixels. Then, the cross correlation was performed and the first pass velocity vector field was obtained. After that, the FOV was again divided in even smaller interrogation windows (32 x 32 pixels) and the values obtained in the first pass were used as input values for the second pass. Finally, the cross correlation was performed once more and the final velocity vector field was obtained [1].

A post processing operation allows us to refine the velocity vector field removing erroneous vectors. Thus, groups with less than 5 vectors, which are 2.5 rms different from the average of neighbouring vector values, were removed.

Three hundred pairs of pictures resulting in three hundred velocity vector fields were obtained.

For most turbulence analyses, it is required to obtain the fluctuating velocity fields. PIV only provides local velocity data; therefore, the Reynolds decomposition is used to perform these calculations [4]:

$$u = \bar{u} + u' \quad (5)$$

$$v = \bar{v} + v' \quad (6)$$

Where $\bar{u}$ and $\bar{v}$ are the time average velocities and u' and v' are the fluctuation components.

For example, for the Reynolds stress calculations, once the fluctuation components are calculated, the product $u'v'$ is calculated in every fluctuation field and then is time averaged in the *x* direction using the 300 fluctuation fields. As a result, the product $\rho\overline{u'v'}$ is obtained and used in the subsequent analyses presented in the results section. In this study, 300 pair of pictures which are representative of the turbulent flow were taken and processed.

Figures 3-5 to 3-9 are presented to describe the sequence of the steps taken while processing PIV data. Figure 3-5 is an example of the primary image obtained before processing. After acquiring the images as shown in figure 3-5, Davis 7.2 is used for calculating the velocity fields by Direct Cross-Correlation Method (DCM). 300 velocity fields are obtained as shown in figure 3-6.

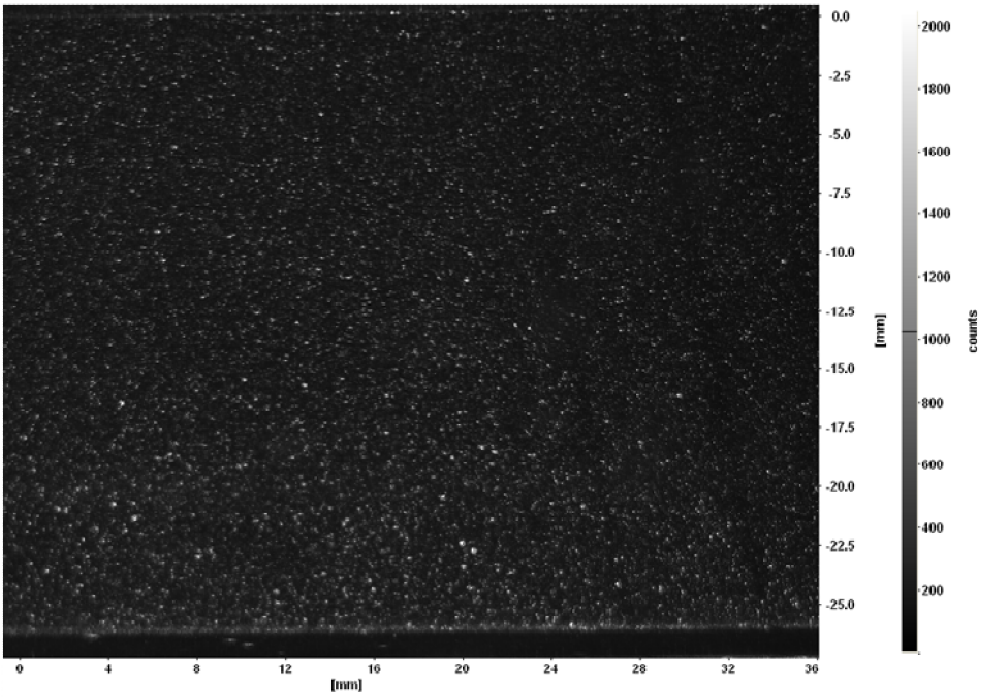

Figure 3 - 5. Field Flow Image Obtained Before Processing.

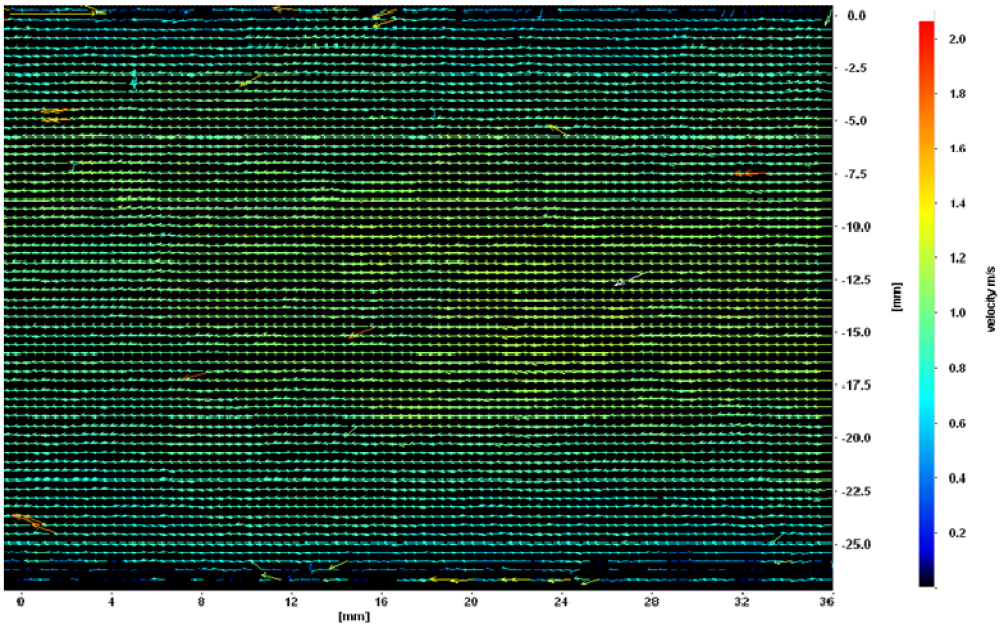

Figure 3 - 6. Velocity Field Obtained After DCM.

In order to remove the erroneous vectors, the post-processing is performed and refined figures like the one shown in figure 3-7 are obtained.

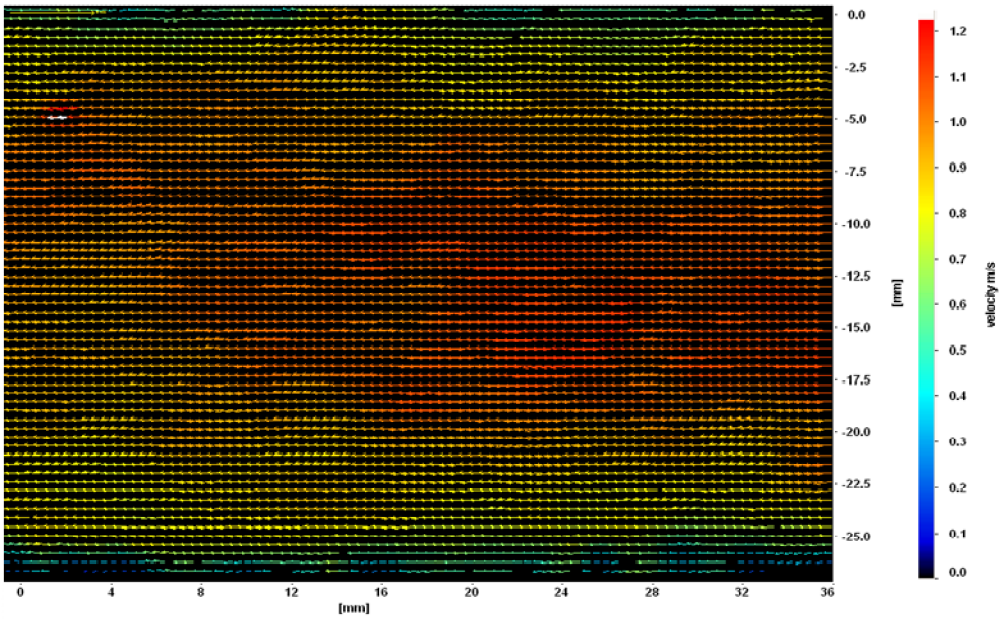

Figure 3 - 7. Velocity Field Obtained After Post-processing.

A time averaged velocity field is required for calculating the fluctuation components of the velocity; therefore, the time average of the 300 velocity fields is calculated and the resulting image is shown in figure 3-8.

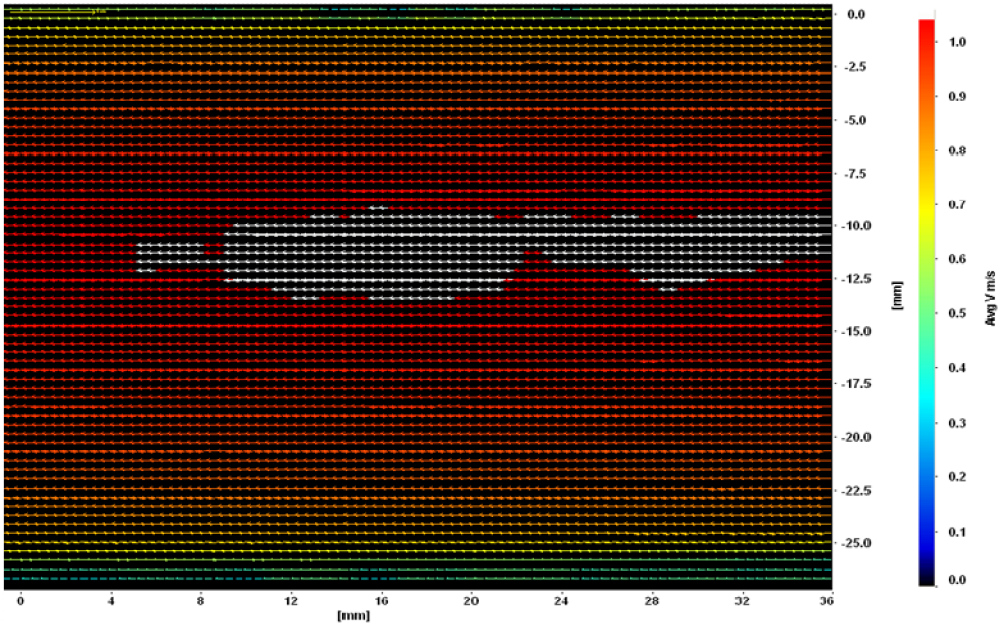

Figure 3 - 8. Time Average of the 300 Velocity Fields

Finally, the Reynolds decomposition is used for calculating the 300 fluctuation velocities fields as shown in figure 3-9.

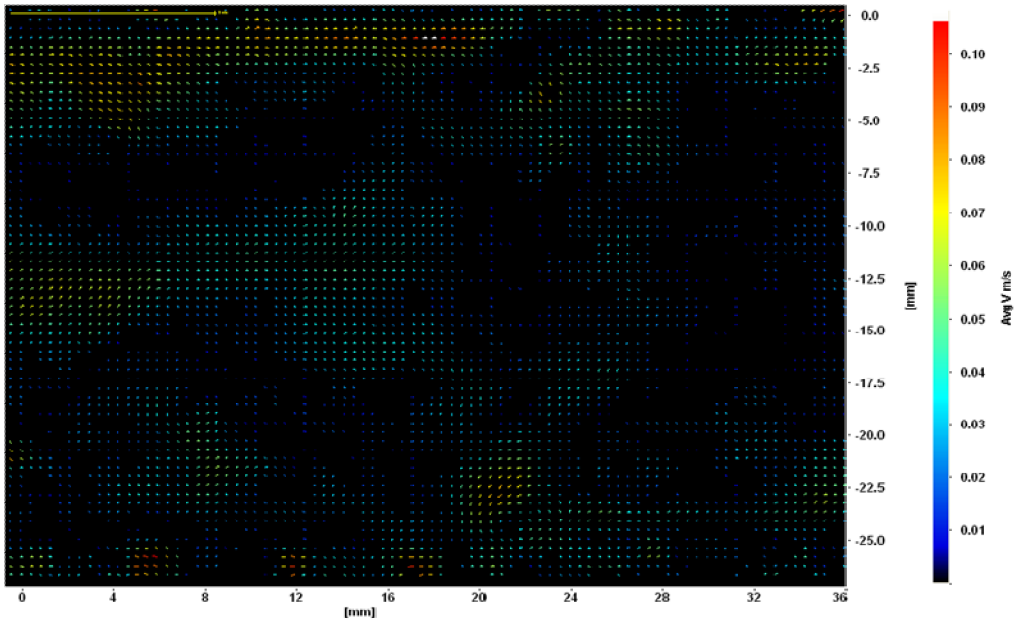

Figure 3 - 9. Fluctuation Velocity Fields

3.4 References

[1] LaVision. “Flow Master Getting Started,” Product manual (2006).

[2] Nezu, I., and Sanjou, M., 2011, “PIV and PTV measurements in hydro-sciences with focus on turbulent open-channel flows,” *Journal of Hydroenvironment Research*, 5, pp. 215-230.

[3] LaVision., “Flow Master,” Product Catalogue, 2006.

[4] Kund, P. and Cohen I., 2008, “Fluid Mechanics, Fourth Edition,” Elsevier.

4 TURBULENT FLOW OF WATER IN HORIZONTAL CONCENTRIC ANNULI[1]

4.1 Introduction

Turbulent flow through concentric annulus is encountered in many different industrial applications. For instance, in oil and gas well drilling engineering flow through the annular geometry is commonly experienced, where good understanding of turbulent flow of drilling fluids is required especially when designing strategies to improve the well bore cleaning. Other industries including the food and chemical industries also involve in processes where the turbulent flow in concentric annulus is encountered such as design of heat exchangers.

In annular turbulent flow, unlike the pipe and channel flow, variation of the total shear stress and velocity across the radial space between two pipes is non linear. This makes the study of turbulence in annular geometry to become more complex than that of the pipe and channel flow [1].

Fully developed turbulent flow in the concentric annulus has been studied by many researchers in the past, however, there is no common agreement among the researchers on the question of whether locations of maximum velocity and zero shear stress coincide at the same point or not.

Brighton and Jones et al. [2] used the double pitot-tube technique to measure the velocity profile and the hot wire anemometry technique to find the zero shear stress location. They

[1] A version of this chapter has already been presented.
Rodriguez-Corredor, F.E., Bizhani, M., Kuru, E., and Ashrafuzzaman, M., 2012, "An experimental investigation of turbulent flow in concentric annulus using particle image velocimetry technique," ASME 2012 International Mechanical Engineering Congress & Exposition (IMECE), Technical paper. Houston, Texas, US.

reported that the locations of maximum velocity and zero shear stress did coincide at the same point.

Recently, Boersma and Breugem et al. [3] also found the radial locations of maximum velocity and zero shear stress to be identical. They had this conclusion based on results obtained from direct numerical simulations (DNS) study. However, they did not validate their results with any experimental data.

Kjellstrom and Hedberg et al. [4] performed theoretical analyses showing that maximum velocity and zero shear stress locations do not necessarily coincide at the same point. They also provided some experimental data showing that shear stress distribution is asymmetric, however, the maximum velocity and zero shear stress locations were coinciding at the same radial point [4].

Lawn and Elliott et al. [5] used hot wire anemometry technique to study the turbulent flow in annulus. They found that maximum velocity and zero shear stress locations did not coincide at the same radial location [5]. This difference was observed to become smaller with the increasing inner to outer pipe radius ratio [5].

Rehme [6] also measured the velocity profile and shear stress profiles in concentric annulus using the hot wire anemometry technique. He found that the maximum velocity and zero shear stress location do not occur at the same radial location [6].

Chung et al. [7] performed direct numerical simulations to study the flow and heat transfer in concentric annuli. They reported a small difference between the locations of zero shear stress and maximum velocity [7].

Ould–Rouiss et al. [8] also conducted direct numerical simulations to analyze turbulent heat and fluid flow in the annulus. The radial locations of maximum velocity and zero shear stress were found to be different [8].

Nouri et al. [9] conducted an experimental study measuring the three components of mean velocity and the corresponding Reynolds shear stresses in fully developed concentric and eccentric annulus flows of Newtonian and non-Newtonian fluids. The velocity profile was found to be following the universal law of the wall ($u^+=y^+$) in the viscous sub layer and following the log law equation ($u^+=2.5\ln y^+ +5.5$) presented by Bernard and Wallace for pipe flow in the logarithmic zone [10]. However, recently Japper-Jaafar et al. [11] show that in the logarithmic zone the velocity profile follows the log wall equation proposed by Clauser et al. ($u^+=2.5\ln y^+ +4.9$) [12].

Although, significant amount of experimental and numerical data exists on the turbulent flow in concentric annulus, there is no common consensus regarding the coincidence of the radial locations of maximum velocity and zero shear stress yet. In terms of measurement technique, previous researchers used double pitot tube, hot wire anemometry and LDA. None of these previous researchers, however, used PIV technique to measure velocity distribution during the turbulent flow in the concentric annulus. Therefore, in this chapter we will provide more experimental data obtained by PIV technique to the discussion regarding the coincidence of the position of zero shear stress and maximum velocity. Data showing the influence of changing the Reynolds number on these radial locations is presented as well. Additionally, the velocity profile in the region close to the pipe walls, second order turbulent statistics and turbulence structures are analyzed for two different Reynolds numbers.

4.2 Experimental Program

Experimental facility and all the associated equipment were described in detail in Chapter 2. Methodology of PIV data acquisition and analyses were presented in Chapter 3.

Turbulent water flow experiments were conducted at six different Reynolds numbers (17700, 27400, 38700, 46700, 56400, and 67700). Pressure drop across the annular flow loop, volumetric flow rate and velocity profile through PIV measurements were taken simultaneously.

4.3 Results and Discussions

4.3.1 Error Analyses and Interval of Confidence

Figures 4-1 to 4-5 present the results for the axial velocity profile, velocity gradient (du/dy) profile, u'v' distribution, and the RMS of fluctuation velocities in axial and in radial directions, respectively. These results were obtained by circulating water at Reynolds number equal to 56400. The error bars plotted in the same graphs represent the 95% interval of confidence calculated by using the results obtained from three experiments performed at the same conditions. The interval of confidence obtained in the velocity profile is really small. However, the error is propagated as further calculations are performed. For example, the –u'v' profile shows an increment in the interval, but it is still kept small.

The interval of confidence in the velocity gradient is maintained really small, but it gets slightly higher in the RMS fluctuation velocities. The degree of confidence in the

experimental measurement is, therefore, high. Although the small error is propagated, the interval is kept relatively small.

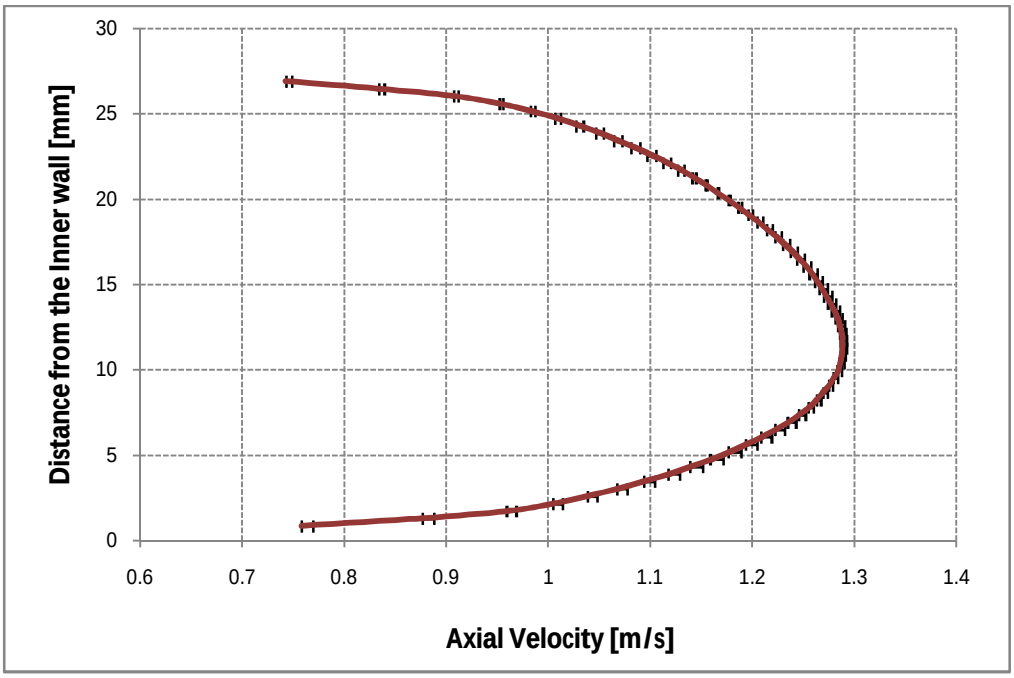

Figure 4 - 1. Velocity Profile and 95% Interval of Confidence.

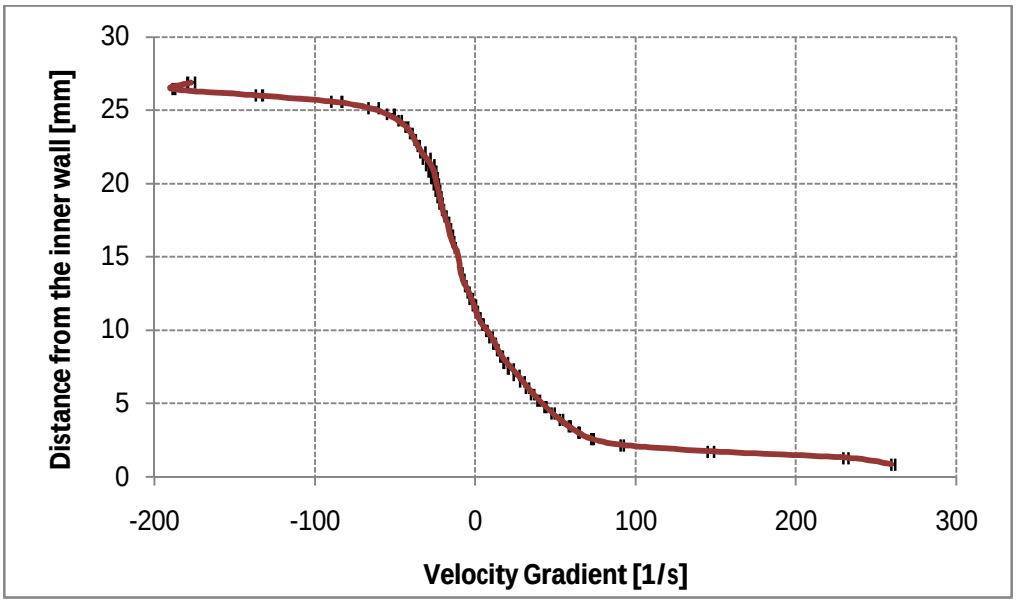

Figure 4 - 2. Velocity Gradient and 95% Interval of Confidence.

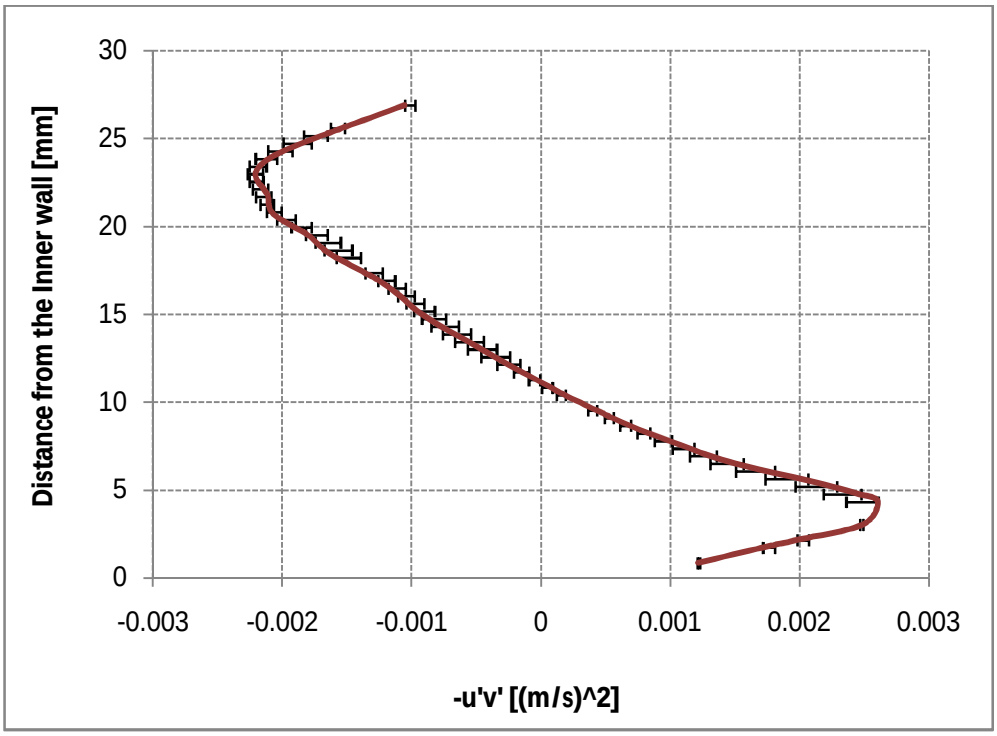

Figure 4 - 3. (–u'v') Profile and 95% Interval of Confidence.

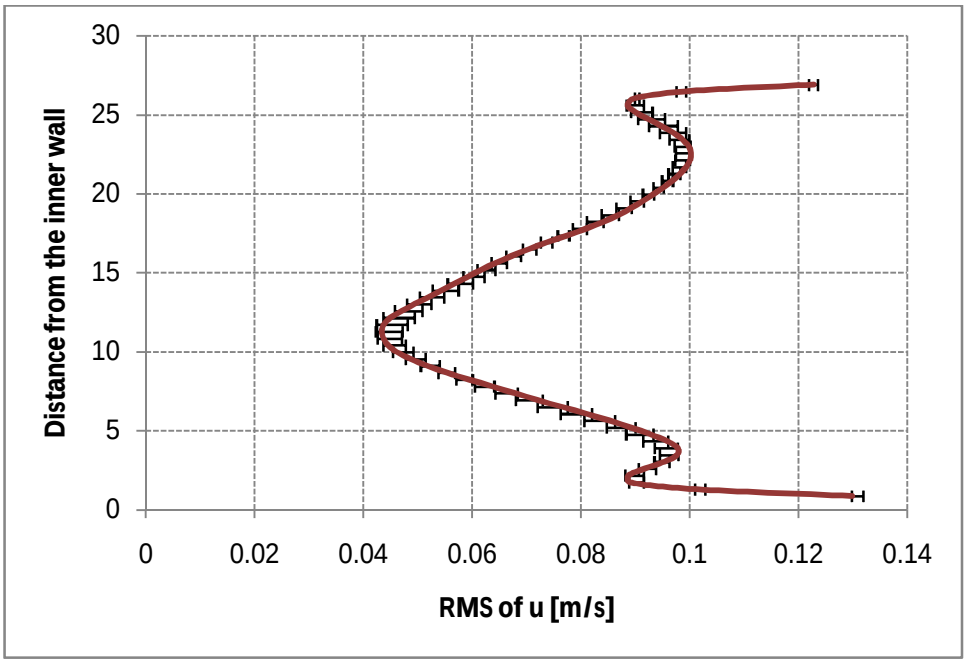

Figure 4 - 4. RMS of Fluctuation Velocity in x (u) Direction Profile and 95% Interval of Confidence.

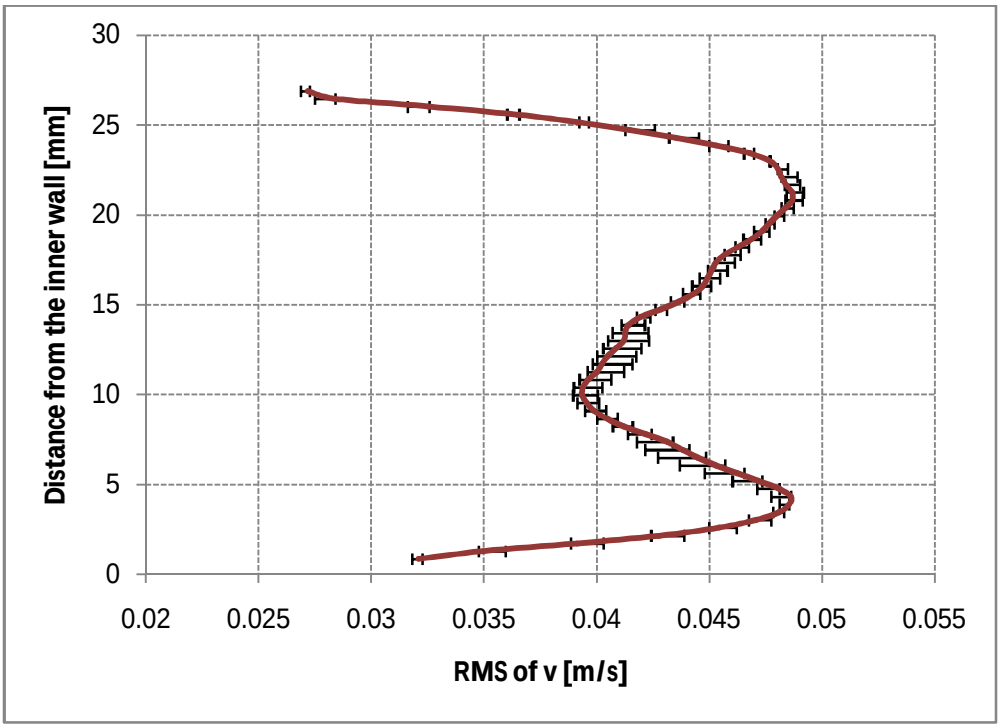

Figure 4 - 5. RMS of Fluctuation Velocity in y (u) Direction Profile and 95% Interval of Confidence.

Figures 4-6 and 4-7 present the effect of PIV interrogation window size on the actual velocity profiles and the -u'v' distribution in the whole annulus, respectively. Three different interrogation window sizes used when performing the cross-correlation were composed of 16x16, 32x32 and 64x64 pixels. All experiments in this case were conducted by water flow at Reynolds Number equal to 56400.

No significant difference on the axial velocity profile was obtained by varying the size of interrogation window. However, due to small differences which propagate through the calculations, there is a noticeable difference in the –u'v' distribution when the largest size of interrogation window (64 x 64 pixels) was used.

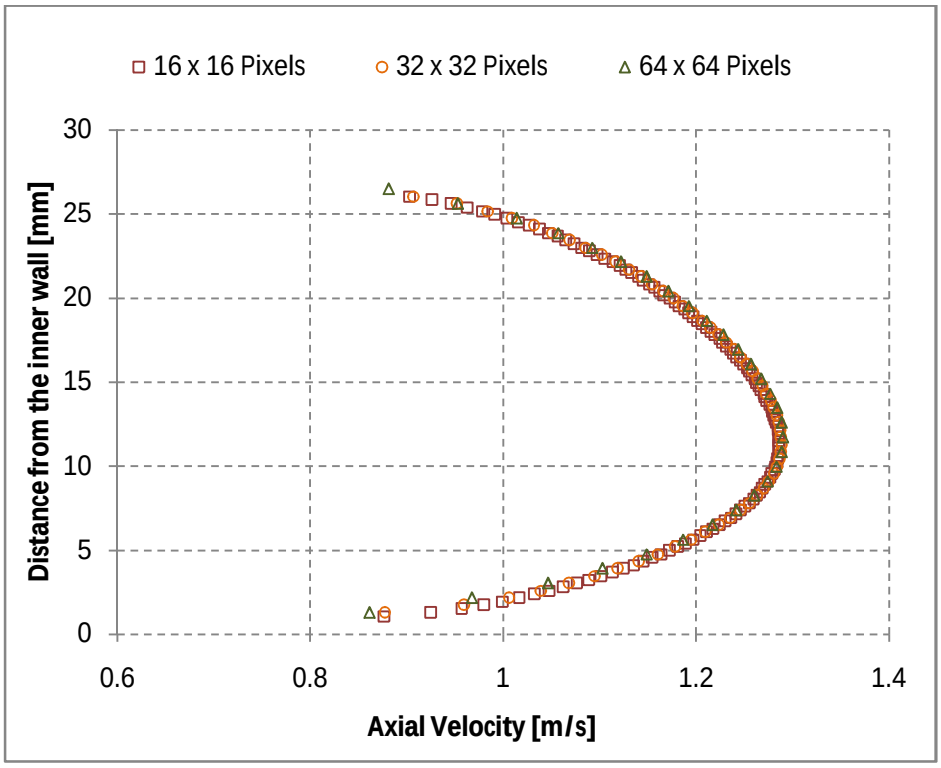

Figure 4 - 6. Effect of PIV Interrogation Window Size on the Velocity Profile.

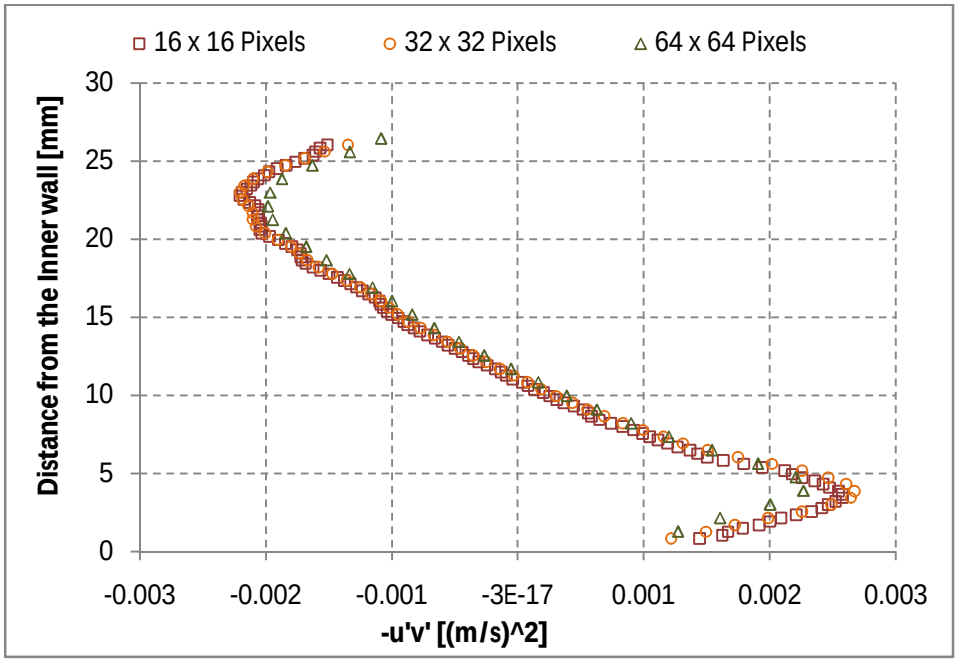

Figure 4 - 7. Effect of PIV Interrogation Window Size on the –u'v' Distribution.

4.1.1 Axial Mean Velocity Profile

Figures 4-8 and 4-9 show the axial mean velocity profile obtained during the turbulent water flow in the region close to the inner and the outer wall, respectively. The data were presented in wall units, which are defined by Eqns. 1-3 [13]:

$$u^+ = \frac{u}{u^*} \tag{1}$$

$$y^+ = \frac{\rho y u^*}{\mu} \tag{2}$$

$$u^* = \sqrt{\frac{\tau_w}{\rho}} \tag{3}$$

Due to the non-linear radial variation of the total shear stress, the wall shear stress is different on the inner and on the outer walls. The wall shear stress calculations are performed by using the equations suggested by Nouri et al. [9]:

$$\tau_{w\ inner\_wall} = -\frac{\Delta P}{L} * \left[\frac{{r_o}^2 - {r_1}^2}{2 * r_1}\right] \tag{4}$$

$$\tau_{w\ outer\_wall} = -\frac{\Delta P}{L} * \left[\frac{{r_2}^2 - {r_0}^2}{2 * r_2}\right] \tag{5}$$

Where r_o is the radial location of the zero shear stress, r_2 is the inner radius of the outer pipe and r_1 is the outer radius of the inner pipe.

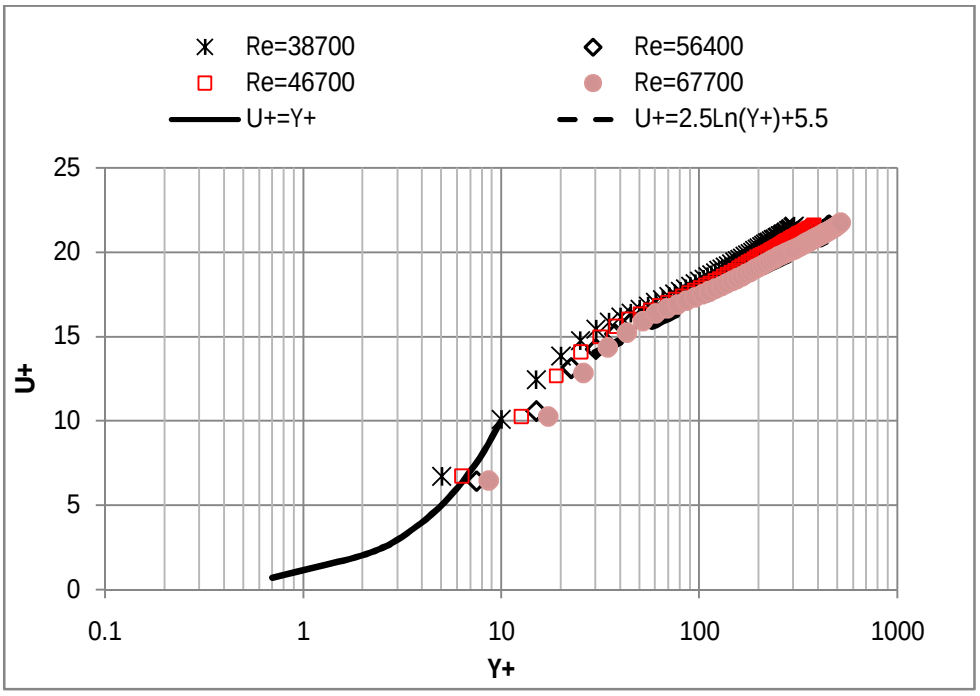

Figure 4 - 8. Axial mean velocity profile in wall coordinates close to the inner wall.

From the data points obtained in the viscous sub-layer ($y^+<10$), it can be observed that the velocity profiles follows the universal wall law ($u^+=y^+$).

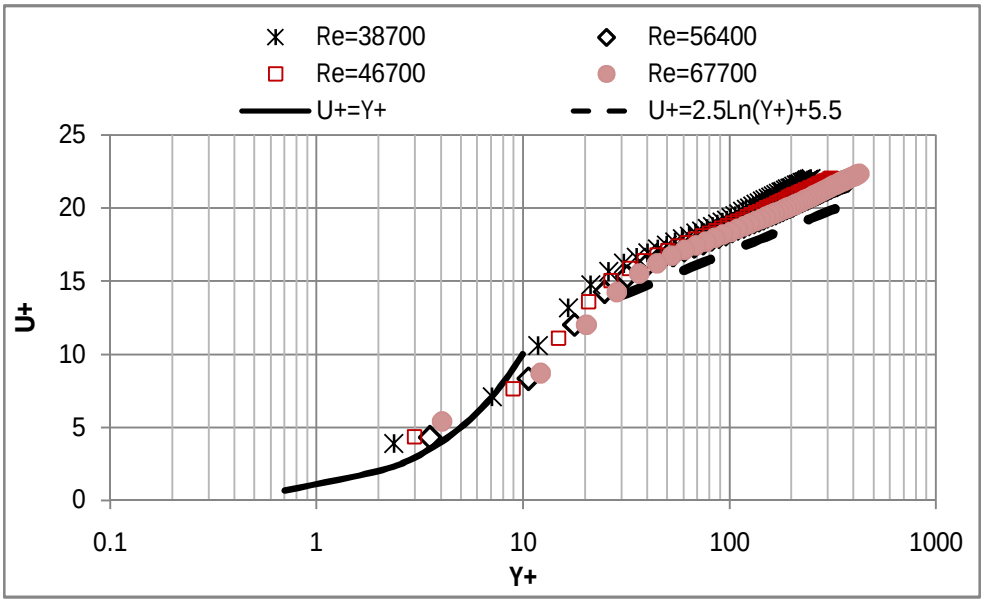

Figure 4 - 9. Axial mean velocity profile in wall coordinates close to the outer wall.

In the logarithmic zone (y^+>30) the experimental data agrees well with the data points obtained by using equation 6 (log law) which was presented by Bernard and Wallace for pipe flow [10]. These results are in agreement with previous experimental results reported by Nouri et al. [9], Churchill et al. [14], Chung et al. [7] and Kaneda et al. [15].

$$u^+ = 2.5 \ln y^+ + 5.5 \tag{6}$$

It is also noticeable that the experimental data agrees better with the log wall law as the Reynolds number is increased. Similar results were also reported by Lawn and Elliott et al. [5].

In the logarithmic zone, the outer wall data is observed to be slightly higher than that of the inner wall data. This is in agreement with numerical simulations, which suggested that this slight difference is due to the curvature effect in the inner pipe where the friction coefficient is higher [7,8]. They also showed that the difference between the inner and outer wall velocity profiles were found to be more significant for smaller inner to outer radius ratio (r_1/r_2=0.1) and almost zero for bigger inner to outer radius ratio (r_1/r_2=0.5) [7].

4.3.2 Total Shear Stress and Axial Velocity Profiles in the Whole Annular Space

The PIV technique only provides velocity data. Therefore, the total shear stress distribution needs to be calculated by using the time averaged momentum balance equation [16].

$$\tau = \rho \overline{u'v'} - \mu \frac{\partial u}{\partial y} \tag{7}$$

Where μ is the fluid viscosity and ρ is the fluid density. The first term on the right hand side of the equation 7 represents the turbulent Reynolds stress. The time averaged product $u'v'$ is calculated using the Reynolds decomposition as explained in chapter 1.

The second term on the right hand side of equation 7, represents the viscous stress. The gradient of velocity along the y direction is calculated using numerical methods [17]:

When the right and left neighbor vector exist, the gradient of velocity is calculated as follows [17]:

$$\left(\frac{\partial u}{\partial y}\right)_{n,m} = \frac{u_{n,m+1} - u_{n,m-1}}{2 * \text{grid size}} \tag{8}$$

When only left neighbor and vector itself exist, the gradient of velocity is calculated as follows [17]:

$$\left(\frac{\partial u}{\partial y}\right)_{n,m} = \frac{u_{n,m} - u_{n,m-1}}{\text{Grid size}} \tag{9}$$

When only left right and vector itself exist, the gradient of velocity is calculated as follows [17]:

$$\left(\frac{\partial u}{\partial y}\right)_{n,m} = \frac{u_{n,m+1} - u_{n,m}}{\text{Grid size}} \tag{10}$$

Figures 4-10 and 4-11 show the velocity profile obtained for six different Reynolds numbers. The results were normalized using the bulk velocity, u_b, ($=u/u_b$) and plotted against the non-dimensional distance from the inner wall ($\xi = \frac{r-r_1}{r_2-r_1}$).

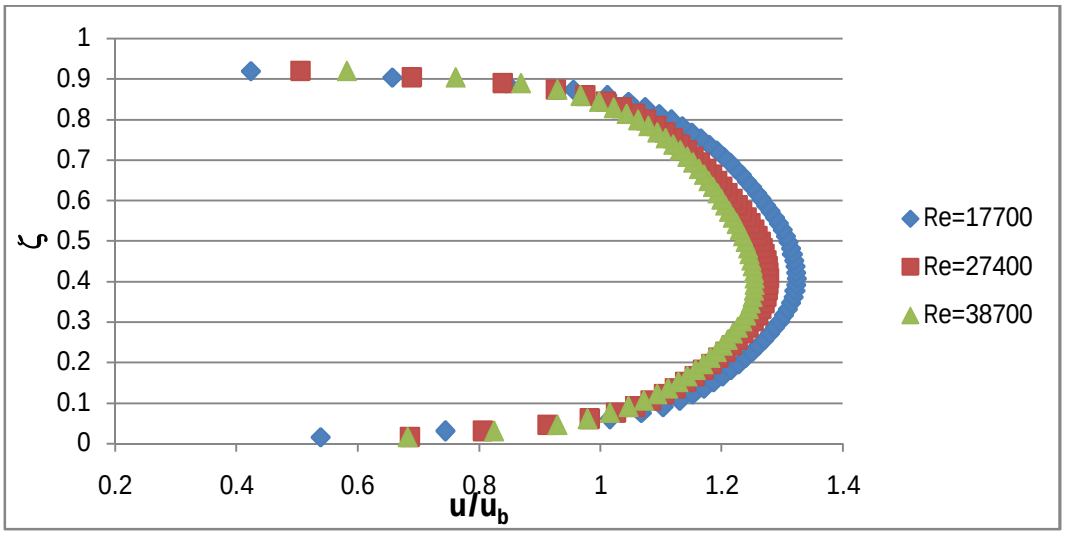

Figure 4 - 10. Axial Mean Velocity Profile in the Whole Annular Section (Re=17700 to 38700).

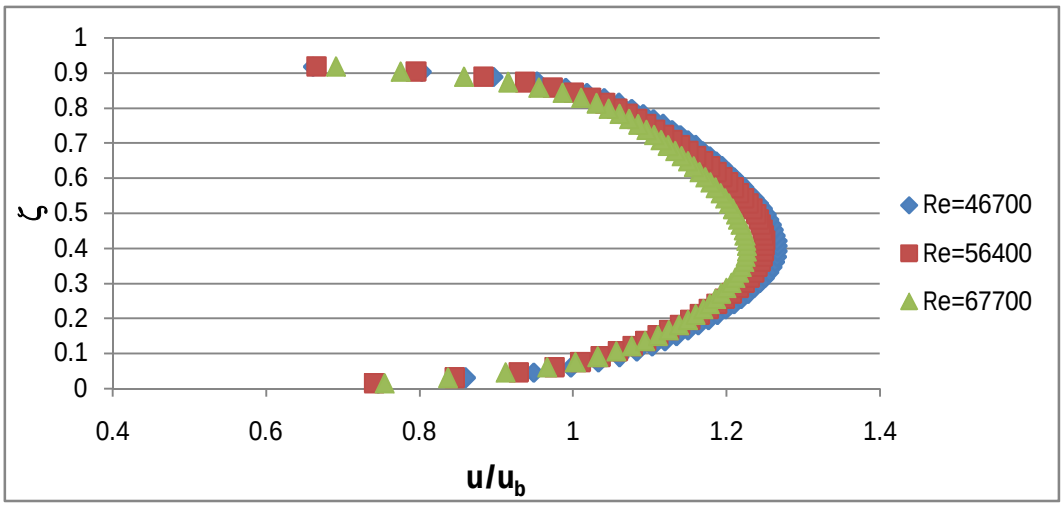

Figure 4 - 11. Axial Mean Velocity Profile in the Whole Annular Section (Re=46700 to 67700).

Unlike pipe flow, the velocity profile has an asymmetric shape. The position of maximum velocity is closer to the inner pipe wall. These results are in accordance with experimental and numerical results presented earlier [7,9]. Moreover, the u_{max}/u_b ratio obtained in the

core flow region was found to be lower for higher Reynolds number. Similar results were also found by Japper-Jaafar et al [11].

Figures 4-12 to 4-13 show the total stress profiles in the whole annular section for six different Reynolds number. The total shear stress was normalized using the bulk velocity ($= \tau/u_b^2$) and plotted against the non-dimensional distance from the inner wall ($\xi = \frac{r-r_1}{r_2-r_1}$).

Similar to the velocity profile, the total shear stress profile also has an asymmetric shape. The location of zero shear stress is also placed closer to the inner pipe wall. It was observed that the zero shear stress location is almost invariable by changing the Reynolds number.

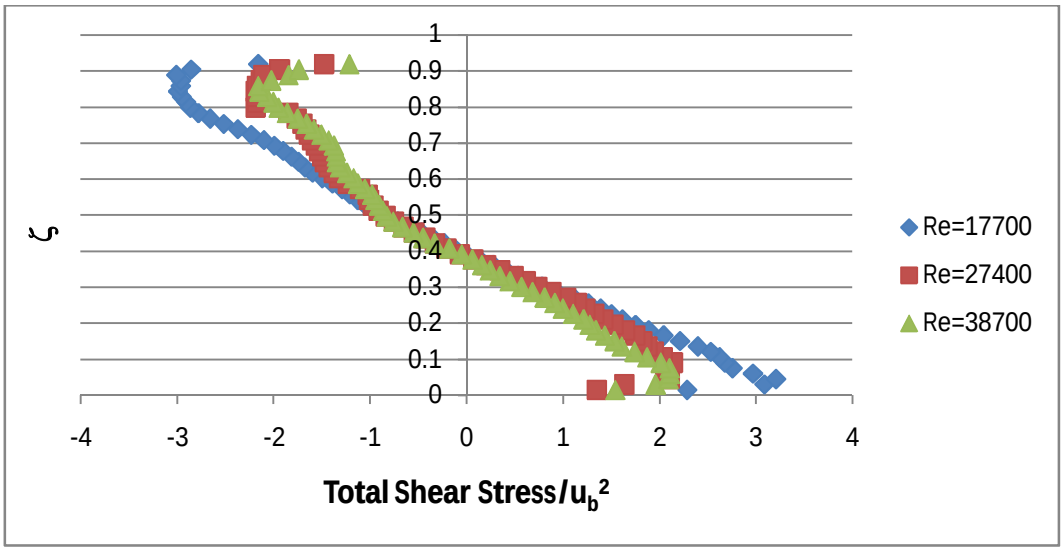

Figure 4 - 12. Total Shear Stress Profile in the Whole Annular Section (Re=17700 to 38700).

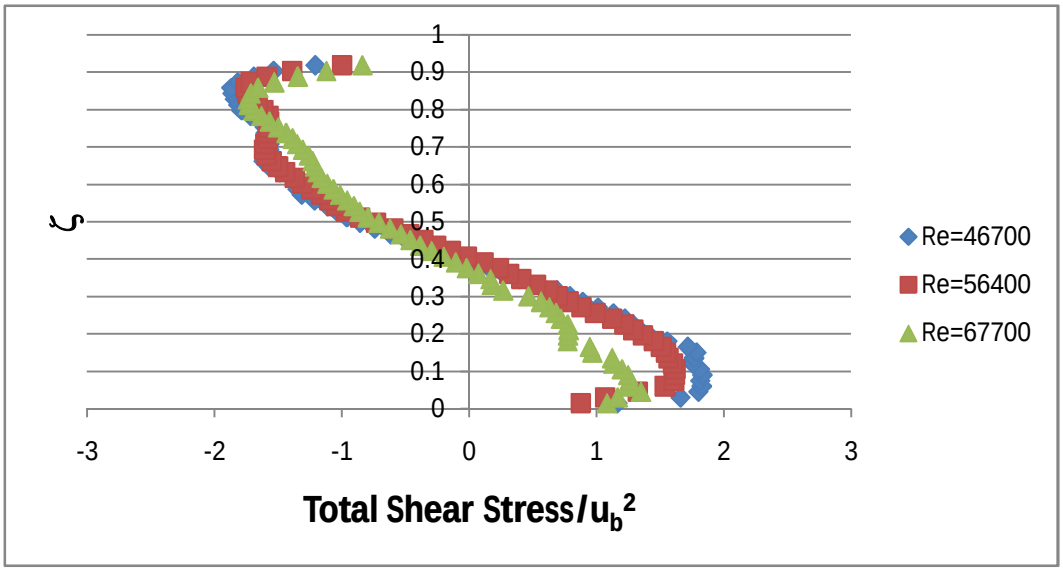

Figure 4 - 13. Total Shear Stress Profile in the Whole Annular Section (Re=46700 to 67700).

4.3.3 Radial Location of Zero Shear Stress and Maximum Velocity

Table 4-1 presents a comparison between the radial locations of maximum velocity and zero shear stress.

Table 4 - 1. Radial Position of Zero Shear Stress and Maximum Velocity

Re	r_m/r_2	r_o/r_2	% Difference
17700	0.657	0.646	1.64
27400	0.657	0.646	1.64
38700	0.657	0.642	2.28
46700	0.657	0.648	1.32
56400	0.665	0.655	1.71
67700	0.657	0.636	3.25

Radial locations of maximum velocity and zero shear stress were found to be different (± 0.5 mm) in all of the cases studied. This difference varied between 1.3 and 3.3%, on on the average it was around 2%. Additionally, comparison between zero shear stress and

maximum velocity locations shows the position of zero shear stress placed even closer to the inner pipe wall. Moreover, no significant numerical changes in these locations were observed by changing the Reynolds number.

Results obtained experimentally by Lawn and Elliott et al. [5] who used the hot wire anemometry technique to measure the velocity profile in a flow loop facility with a inner to outer radius ratio very close to the one used in this experimental study (0.396), show that for Reynolds numbers ranged between 30,000 and 70,000 the radial position of maximum velocity and zero shear stress are around r_m/r_2=0.655 and r_0/r_2=0.655 respectively. Figure 4-14 presents a comparative analysis of the positions of maximum velocity obtained by Lawn and Elliott et al. [5] and by using PIV technique. It can be observed that the locations of maximum velocity obtained by using the PIV technique implemented in this study were in a very good agreement with the locations obtained by using the hot wire anemometry technique implemented by Lawn and Elliott et al [5].

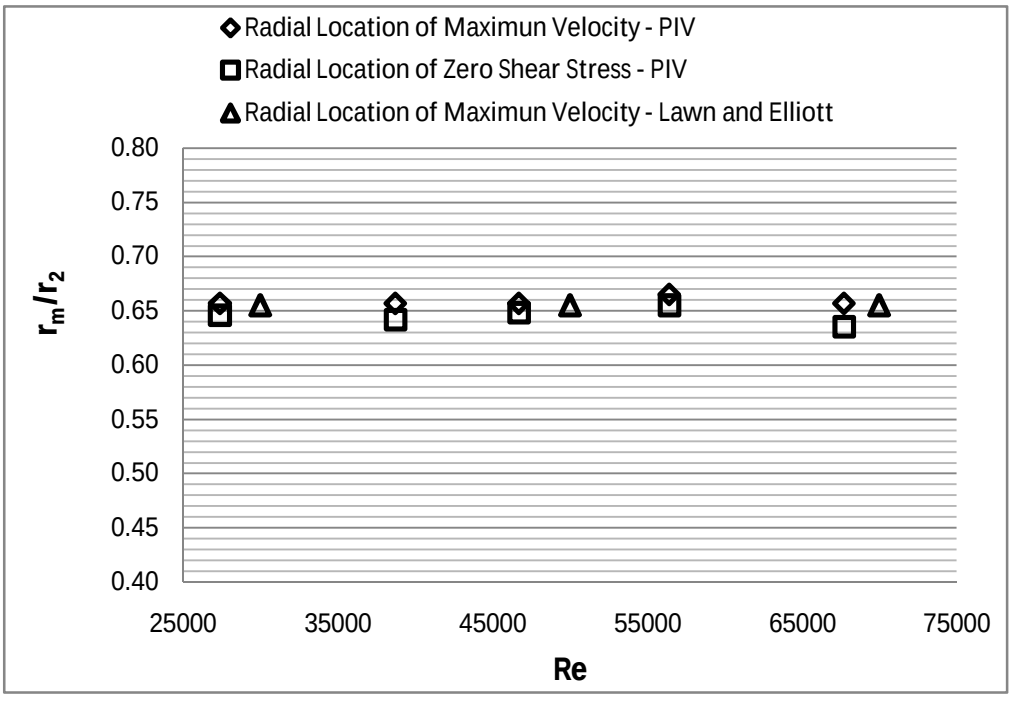

Figure 4 - 14. Comparison of radial locations of maximum velocity and zero shear stress.

Leung et al. [18] suggested an empirical relationship for calculating the radial location of maximum velocity [18]:

$$\frac{r_m - r_1}{r_2 - r_m} = \left(\frac{r_1}{r_2}\right)^{0.343} \quad (11)$$

By using the inner and outer radius values of the flow loop described in chapter 2, the radial location of maximum velocity calculated by equation 11 was found to be r_m/r_2=0.653. This value agrees very well with the value obtained by using PIV, which was r_m/r_2=0.656.

4.3.4 Results of Second-Order Turbulence Statistics and Turbulent Structure Analyses

Velocity distribution obtained from PIV measurements are further used to conduct detailed turbulence statistics and turbulent structure analyses near the wall.

4.3.4.1 Root Mean Square of the Fluctuation Velocities

In turbulent flow, the root mean squares of the fluctuation velocities are associated with the turbulent kinetic energy (TKE) since they are used to perform the TKE calculations. Therefore, the root mean square root mean square of the fluctuation velocities can be considered as a measurement of the turbulent intensity in the flow.

Figure 4-15 and 4-16 present the root mean square (rms) of the axial and radial fluctuation velocities, respectively.

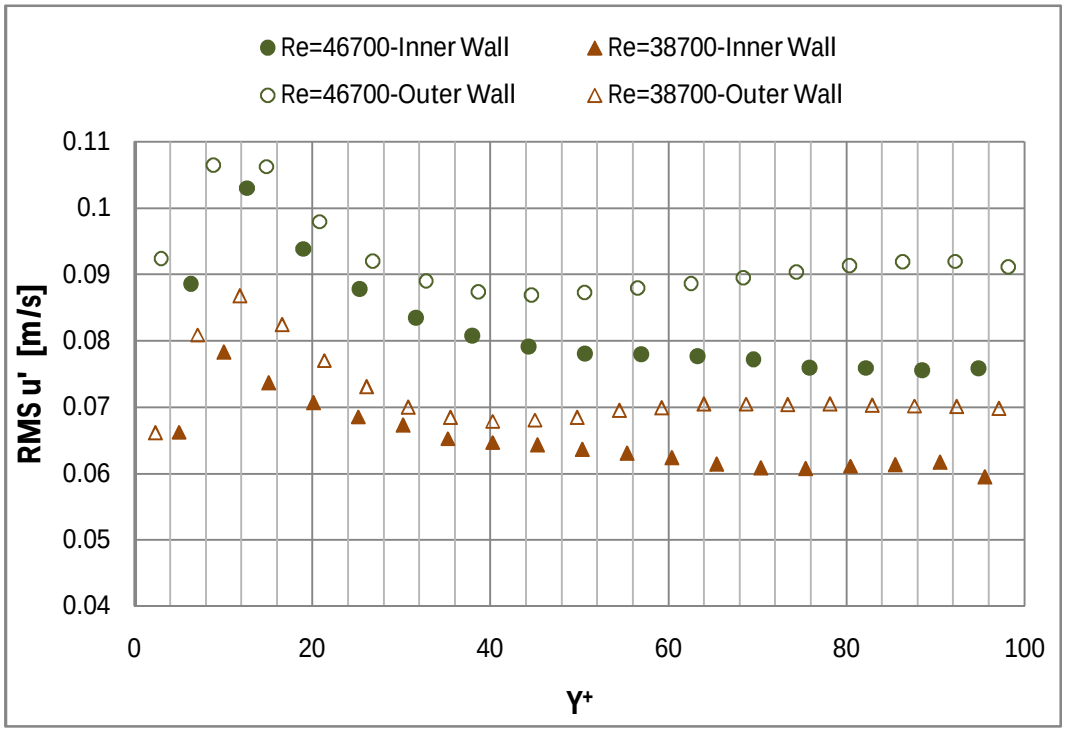

Figure 4 - 15. Root Mean Square of the Axial Fluctuation Velocities.

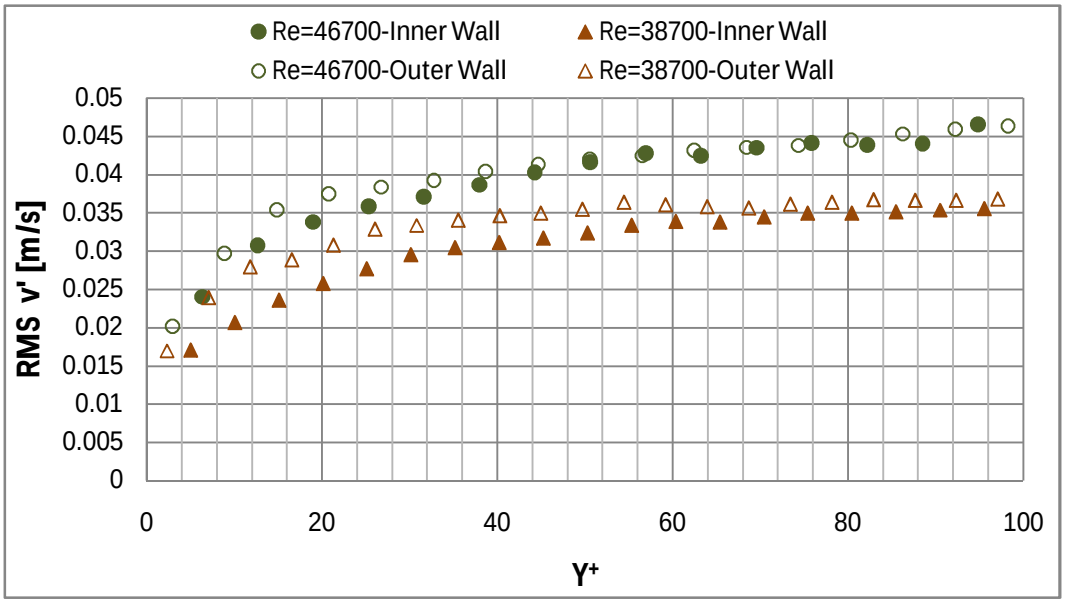

Figure 4 - 16. Root Mean Square of the Radial Fluctuation Velocities.

In general, the rms values are higher at the outer wall than at the inner wall. The difference is more noticeable in the axial rms values. This can be explained by taking into

account the transverse curvature effect. The surface area in the inner wall is smaller than that of the outer wall and therefore, less turbulent kinetic energy is supplied by the inner wall to the same volume of flow [7].

RMS fluctuation velocity values increase with the increasing Reynolds number.

Peak values of axial rms fluctuation velocities are located in the buffer zone between 10 and 14 wall units. These values can be normalized using the shear velocity (u_τ) for comparison purposes. The normalized values obtained are in average 2.1 and 2.5 for the inner and outer wall respectively. Similar results were obtained by numerical simulations and experimentally by means of Laser Doppler Anemometry technique using an inner to outer radius ratio equal to 0.5. In their case, the normalized peak values obtained were 2.2 and 2.6 for the inner and outer wall respectively [7,11].

The radial rms fluctuation velocities are smaller in the region close to the pipe walls. However, as it moves further away from the wall, the radial rms values start increasing progressively until achieving a maximum value. This maximum value can be normalized using the shear velocity as in the previous case. The normalized radial rms values are very similar at both pipe walls being in average 0.96 and 1.01 for the inner and outer wall respectively. Japper-Jaafar et al.[11] reported similar values for an inner to outer radius ratio equal to 0.5. In their case, the maximum radial rms value was slightly higher than 1 at the outer wall and slightly smaller than 1 at the inner wall [11].

4.3.4.2 Reynolds and Total Stresses

Figure 4-17 presents the results of Reynolds stresses (= ρu'v') calculations near the inner and outer walls.

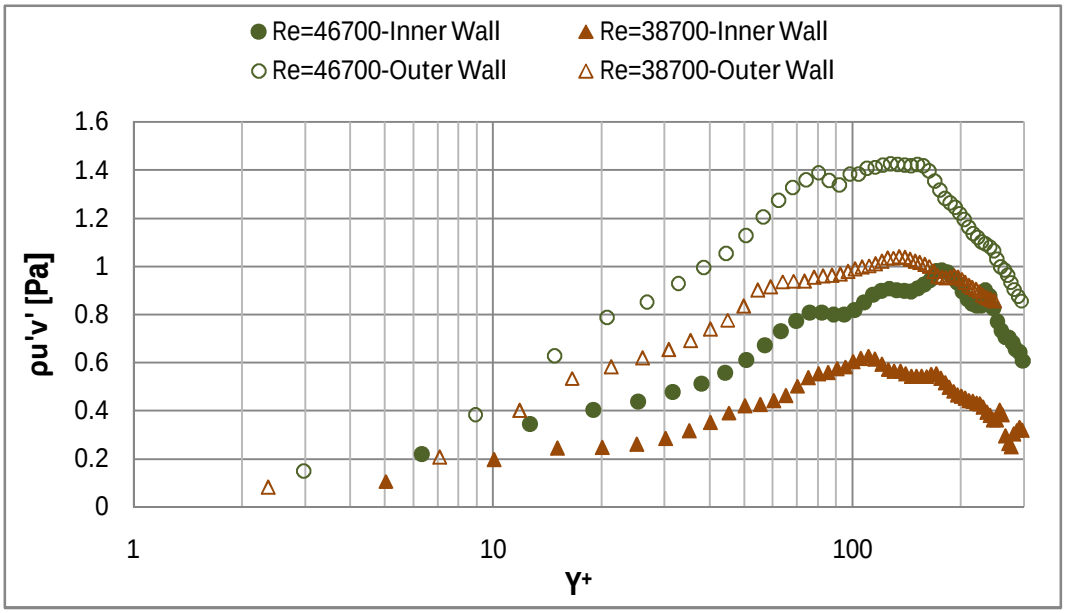

Figure 4 - 17. Reynolds Stress Close to the Inner and Outer Wall.

Reynolds stress values are significantly larger at the outer wall than at the inner wall. The difference between outer and inner wall results was expected since both radial and axial rms fluctuation velocity values were higher at the outer wall. However, in the viscous sub-layer (y^+<10) these values are very similar for both walls.

Finally, the peak values of Reynolds stress were found to occur far away from the wall (after 100 wall units). After achieving the peak value, the Reynolds stress starts decreasing significantly.

The total shear stress (Equation 7) obtained is shown in figure 4-18. In the viscous sub-layer (y^+<10), the total shear stress was found to be very similar for both walls. However, after y^+=10 the total wall shear stress is larger at the outer wall. It can be observed that close to the wall, the total shear stress achieved the maximum values. This is due to the high values of velocity gradients obtained close the wall, which increase the viscous stress component. However, after y^+=10, the total shear stress starts behaving like the

Reynolds stress. This is because after $y^+=10$, the viscous stress values obtained are really low compare to the values of Reynolds stress obtained. Therefore, the Reynolds stress will be predominant after $y^+=10$.

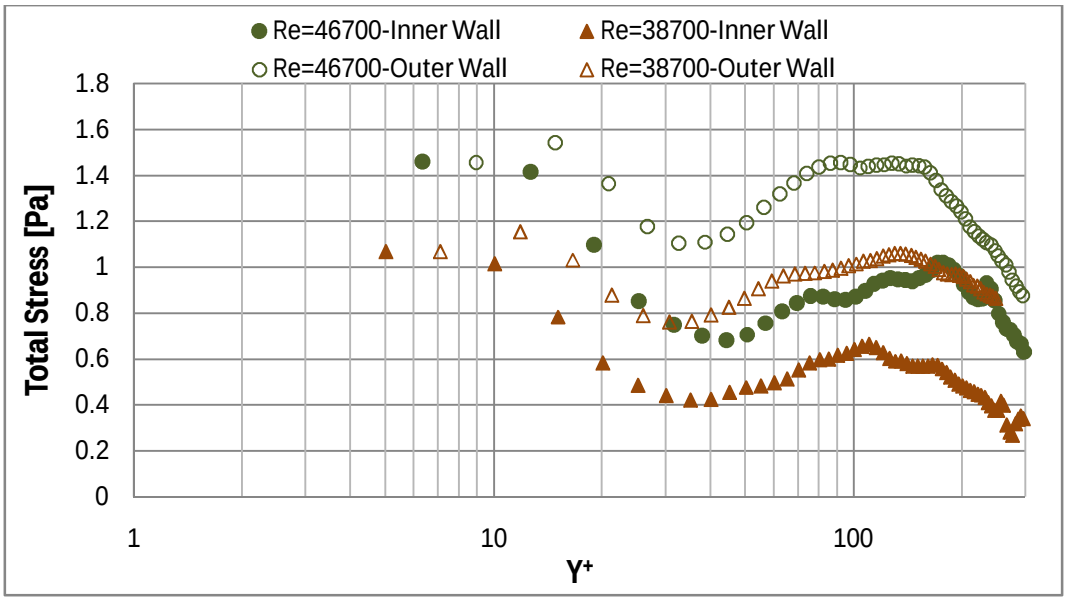

Figure 4 - 18. Total Stress Close to the Inner and Outer Wall.

4.3.4.3 Averaged 2D Vorticity

Vorticity is another important parameter to study in the structure of turbulence as it can be linked to the production of turbulence.

The two dimensional vorticity in the xy plane is calculated using the following relationship [33]:

$$\omega_{xy} = \frac{dv}{dx} - \frac{du}{dy} \tag{12}$$

The vorticity calculation in the xy plane is performed using the central difference scheme with the four closest neighbours as shown in figure 4-19.

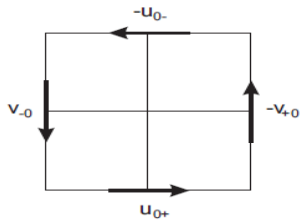

Figure 4 - 19. Central Difference Scheme Implemented in the Vorticity Calculations [17].

Figure 4-20 presents the average vorticity values calculated near the inner and outer wall.

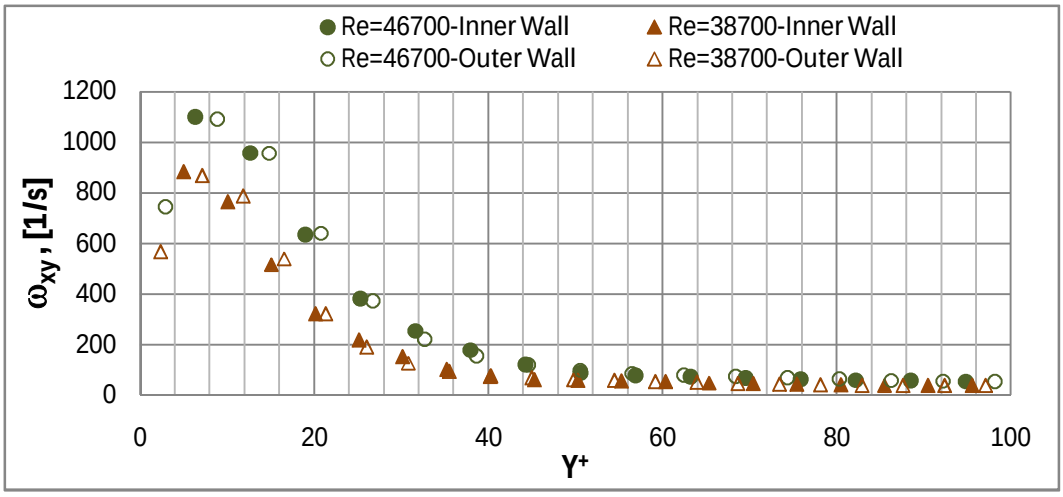

Figure 4 - 20. 2D Vorticity Values Near the Inner and Outer Wall.

Higher values of vorticity were found in the viscous sub-layer where they achieved a maximum vorticity value. The peak values are located between 4 and 6 wall units. After 6 wall units, the vorticity starts decreasing until achieving values very close to zero. Differences between inner and outer wall results are insignificant. It is also observed that higher vorticity values are obtained as the Reynolds number is increased.

4.3.4.4 RMS of Vorticity

Paschkewitz et al [19] suggested that the RMS of vorticity is related to the size and power of the near wall vortex structures. As shown in figure 4-21, the maximum rms vorticity values are obtained in the vicinity close to the pipe walls.

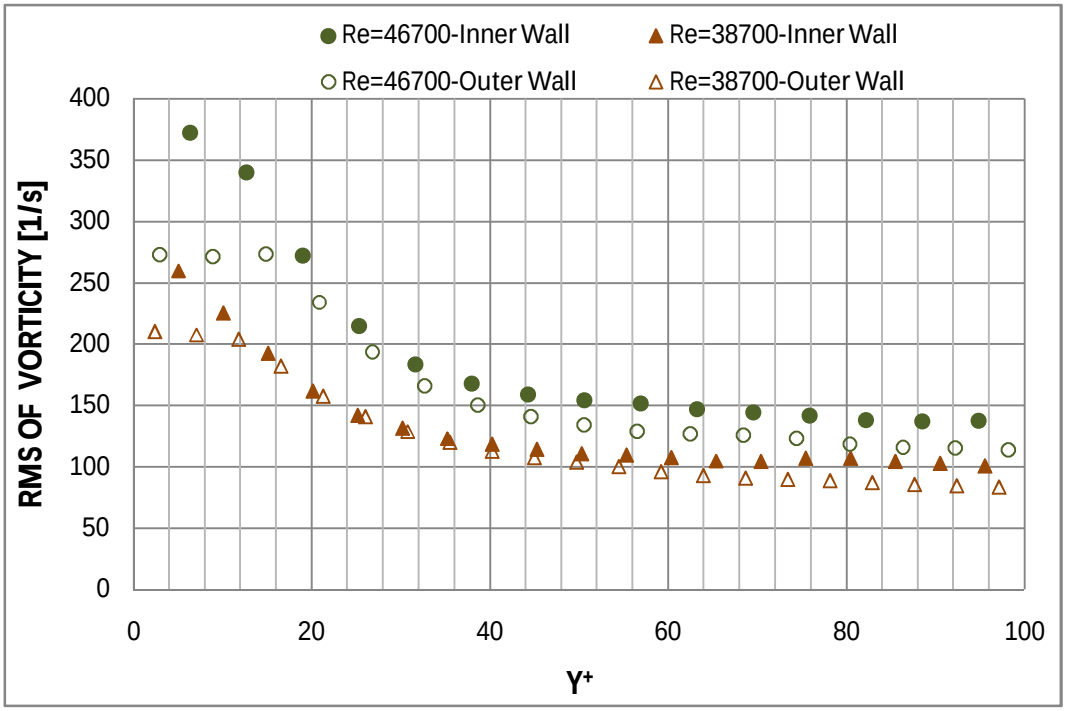

Figure 4 - 21. RMS of Vorticity Close to the Inner and Outer Wall

Maximum values of rms vorticity near the inner wall were higher than that of the outer wall. This suggests that more burst/sweep activities (i.e., turbulent coherent structures) associated with stream-wise vortices are present near the inner wall than near the outer wall. Therefore, greater wall shear stress region is created near the inner wall and, as a result, higher wall shear stress is expected to be encountered near the inner wall. These results can be validated by calculating wall shear stress through the pressure drop calculated using equations 4 and 5. For instance, at Re=46700 the wall shear stress near

the outer wall is calculated as 1.98 Pa whereas the wall shear stress value near the inner wall is calculated as 2.27 Pa.

4.3.4.5 Turbulent Kinetic Energy Budget

The following equation for the turbulent energy in the Newtonian fluid flow is suggested by Kundu and Cohen [16]:

$$\frac{D}{DT}\left(\frac{1}{2}[u']^2\right) = -\frac{\partial}{\partial y}\left(\frac{1}{\rho}\overline{Pv'} + \frac{1}{2}\overline{[u']^2 v'} - 2\vartheta\overline{u' e_{xy}}\right) - \overline{u'v'}\frac{\partial u}{\partial y} - 2\vartheta\overline{e_{xy} e_{xy}} \tag{13}$$

Where e_{xy} is the fluctuating strain rate defined as [35]:

$$e_{xy} = \frac{1}{2}\left[\frac{\partial u'}{\partial y} + \frac{\partial v'}{\partial x}\right] \tag{14}$$

The first and second term on the right hand side of Eqn. 13 represent the transport of turbulent kinetic energy by turbulence itself. The third term represents the viscous transport. The summation of all the three terms is known as total spatial transport of turbulent kinetic energy (T_k).

The fourth term is known as shear production (P_k). Interaction of the mean shear with the Reynolds stress produces turbulent kinetic energy. The rate of generation of turbulent kinetic energy by means of this mechanism is represented by the shear production term (P_k). The last term in Eqn. 20 represents the viscous dissipation of turbulent kinetic energy (V_D).

Figure 4-22 and 4-23 show the results of shear production and viscous dissipation terms of the turbulent kinetic energy budget, respectively.

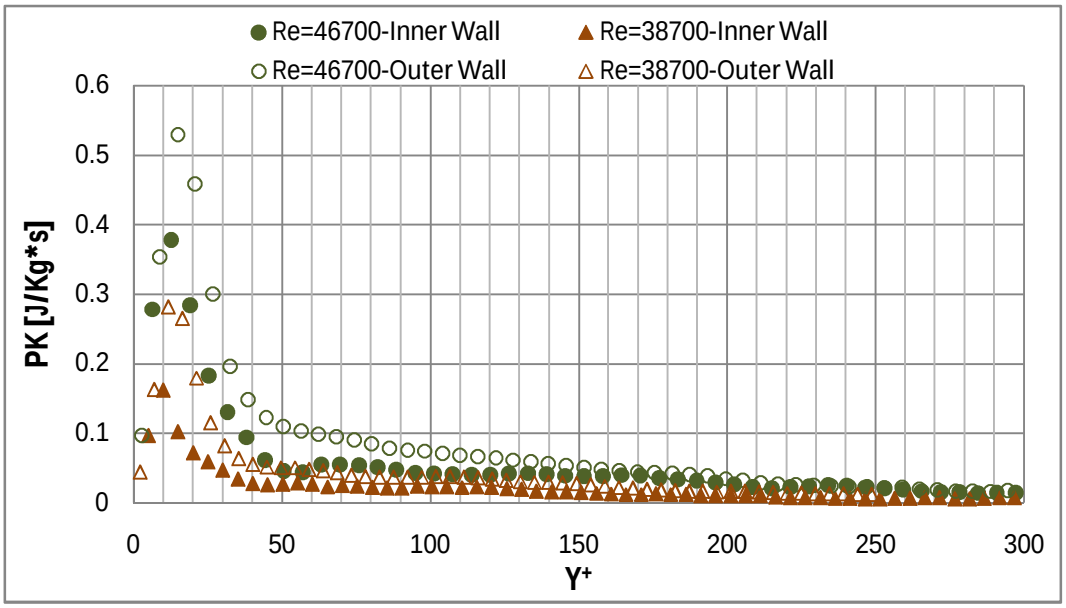

Figure 4 - 22. Shear Production Term (Pk) Near the Inner and the Outer Wall.

As far as the shear production term is concerned, maximum shear production values obtained near the outer wall was higher than that of near the inner wall. Peak production term values are located in the buffer zone between 10 and 14 wall units. These results are agreement with numerical simulation results presented by Chung et al [7]. Moreover, the difference between the inner and outer wall results confirms the rms fluctuation velocity values presented previously.

As shown in figure 4-23, the viscous energy dissipation term was found to achieve a maximum value at the pipe walls. This maximum value was observed to be higher near the outer wall than near the inner wall. This can be explained by taking into account that the surface area in the inner wall is smaller than that of the outer wall and therefore, less turbulent kinetic energy is dissipated at the inner wall.

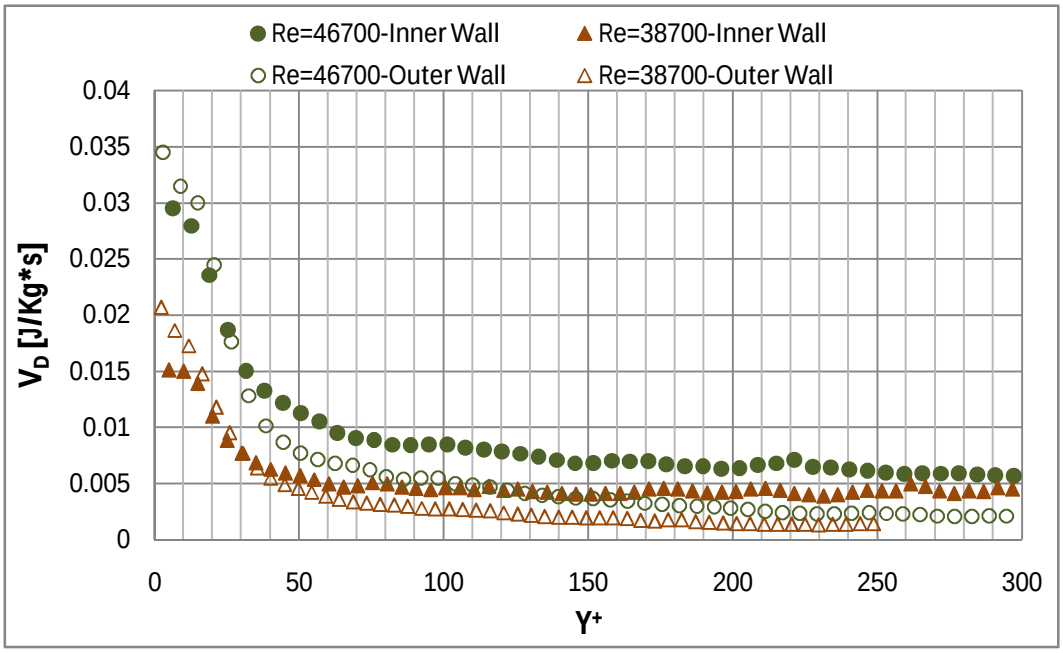

Figure 4 - 23. Viscous Dissipation Term (VD) Near the Inner and the Outer Wall

4.4 Conclusions

New data analysing the position of maximum velocity and zero shear stress in concentric annular turbulent flow is provided to the literature in order to answer if both location coincide or not. This data is highly reliable since it agrees very well with previous experimental data obtained by using different measurement technique (hot wire anemometry).

Additionally, experimental results were provided to analyse the shear production and viscous dissipation term of the turbulent kinetic energy budget as well as the vorticity and rms of vorticity, which have not been extensively studied in the past for the concentric annular flow case.

Axial mean velocity profile for the flow of water in the horizontal concentric annulus was found to be following the universal wall law in the viscous sub-layer ($y^+<10$).

In the logarithmic zone ($y^+>30$), the axial velocity profile is close to the log wall ($u^+=2.5y^++5.5$). However, the best match is obtained for the highest Reynolds number used. Outer wall data was found to be slightly higher than that of the data obtained at the inner wall due to the transverse curvature effect.

Unlike pipe flow, the velocity profile in the whole annular space is asymmetric. The radial position of maximum velocity was found to be placed closer to the inner pipe wall.

The total shear stress profile was found to be curvilinear and asymmetric. Zero shear stress locations were placed closer to the inner wall for all the Reynolds numbers studied.

No significant changes in the zero shear stress and maximum velocity locations were observed by varying the Reynolds number.

Zero shear stress and maximum velocity locations were found to be different (± 0.5 mm). This difference varied from 1.3 to 3.3%. On average the difference was 2%. Additionally, the zero shear stress location was found to be closer to the inner wall than that of the maximum velocity location.

Axial and radial rms fluctuation velocities were found to be higher at the outer wall than at the inner wall. This is attributed to the curvature effect, suggesting that more turbulent kinetic energy is supplied by the outer wall to the same volume of flow.

Peak values of axial rms fluctuation velocity are located in the buffer zone between 10 and 14 wall units.

Reynolds stresses in the vicinity close to the wall are very similar at both inner and outer walls. However, further away from the wall, higher Reynolds stress values are obtained at the outer wall. The total shear stress was found to be very similar in the viscous sub-layer

($y^+<10$) for both walls. After $y^+=10$ the total wall shear stress is larger in the outer wall cases.

The averaged vorticity results show that the vorticity is higher in the vicinity close to the pipe walls. The maximum vorticity is achieved for all the cases in the viscous sub-layer between 4 and 6 wall units. No significant difference in the vorticity values was found between the outer and inner wall results.

Root mean square of vorticity results show that the maximum values of rms vorticity are located in the viscous sub-layer. Higher maximum rms vorticity values were obtained at the inner wall than at the outer wall suggesting that more burst/sweep motions related to stream-wise vortices exist at the inner wall and therefore, higher wall shear stress regions are present at the inner wall. These results were also confirmed with the wall shear stress calculations using the measured frictional pressure drops, in which the wall shear stress obtained at the inner wall was higher than that of the outer wall.

The shear production term of the turbulent kinetic energy budget was found to be higher at the outer wall than at the inner wall, confirming the results obtained from the rms fluctuation velocities. The peak values were located in the buffer zone between 10 and 14 wall units.

Maximum values of viscous turbulent kinetic energy dissipation are observed to occur at the pipe wall. These maximum values were found to be higher at the outer wall than at the inner wall.

4.5 References

[1] Rodriguez-Corredor, F.E., Bizhani, M., Kuru, E., and Ashrafuzzaman, M., 2012, "An experimental investigation of turbulent flow in concentric annulus using particle image velocimetry technique," *Proceedings of ASME 2012 International Mechanical Engineering Congress & Exposition*, Houston, Texas, US.

[2] Brighton, J.A. and Jones, J.B., 1964, "Fully developed turbulent flow in annuli," J. Basic Eng, D86, pp. 835.

[3] Boersma, B.J.,Breugem, W. P, 2011, "Numerical Simulation of Turbulent Flow in Concentric Annuli," Flow Turbulence Combustion, 86, pp. 113-117.

[4] Kjellstrom, B., and Hedberg, S., 1966, " On Shear Stress Distributions for Flow in Smooth or Partially Rough Annuli," Technical Report AE-243, Aktiebolaget Atomenergie, Stockholm, Sweden.

[5] Lawn, C.J., and Elliott, C.J., 1972, "Fully Developed Turbulent Flow Through Concentric Annuli," J. of Mechanical Eng. Science, 14(3), pp. 195-204.

[6] Rehme, K., 1974, "Turbulent flow in smooth concentric annuli with small radius ratios," J. Fluid Mech., 64, pp. 263-287.

[7] Chung, S.Y., Rhee, G.H., Sung, H.J., 2002, "Direct numerical simulation of turbulent concentric annular pipe flow Part 1: Flow field," Int. J. Heat and Fluid Flow, 23, pp. 426-440.

[8] Ould-Rouiss, M., Redjem-saad, L., and Lauriat, G., 2009, "Direct numerical simulation of turbulent heat transfer in annuli: Effect of heat flux ratio," International Journal of Heat and Fluid Flow, 30, pp. 579-589.

[9] Nouri, J.M., Umur, H., Whitelaw, J.H., 1993, "Flow of Newtonian and non-Newtonian Fluids in concentric and eccentric annuli," J. Fluid Mech., 253, pp. 617-641.

[10] Bernard, P.S., Wallace, J.M., 2002, "Turbulent Flow, Analysis, Measurement and Prediction," John Wiley & Sons, New Jersey, U.S, Chap 4.

[11] Japper-Jaafar, A., Escudier, M.P., and Poole, R.J., 2010, "Laminar, transitional and turbulent annular flow of drag-reducing polymer solutions," J. Non-Newtonian Fluid Mech, 165, pp. 1357–1372.

[12] F.H. Clauser, 1956, "The turbulent boundary layer," Advances in Applied Mechanics 4, pp. 1–51.

[13] F.M. White., 2005, "Viscous Fluid Flow," The McGraw-Hill Companies.

[14] Churchill, S.W. and Chan, C., 1995, "Turbulent flow in channels in terms of local turbulent shear and normal stress," AI ChE J. 41, pp. 2513-2521.

[15] Kaneda,M.,Yu, B., Ozoe, H. Churchill,S.W., 2003, "The characteristics of turbulent flow and convection in concentric circular annuli, Part I: flow," Int. J. Heat Mass Transfer, 46, pp. 5045-5057.

[16] Kund, P. and Cohen I., 2008, "Fluid Mechanics," Elsevier, Oxford, UK, 4th ed, pp. 547-549.

[17] LaVision., 2006, "DaVis 7.2 Software," Product-Manual.

[18] Leung, E.Y., Kays, W.M. and Reynolds, W.C., 1962, "Heat transfer with turbulent flow in concentric and eccentric annuli with constant and variable heat flux," Technical report AHT-4, Stanford University, Stanford, CA.

[19] Paschkewitz, J.S., Yves Dubief., Dimitropoulos, C.D., Shaqfeh, E.S.J., and Parviz Moin., 2004, "Numerical simulation of turbulent drag reduction using rigid fibres," *J. Fluid Mech*, Vol. 518, pp. 281–317.

5 AN EXPERIMENTAL STUDY OF DRAG REDUCTION PHENOMENON IN HORIZONTAL CONCENTRIC ANNULI USING PARTICLE IMAGE VELOCIMETRY TECHNIQUE[23]

This chapter presents the results of an experimental study, where the effect of drag reducing additive on the structure of turbulence during the flow through horizontal concentric annuli has been investigated by using particle image velocimetry technique.

5.1 Introduction

Experiments conducted by Toms (1948) discovered that the frictional pressure losses in channel or pipe turbulent flows can be reduced tremendously by the addition of small quantities of drag reducer additives [1]. The reduction in the pressure losses leads to an increase in the pump capacity, decreasing the horsepower requirements. This significant increase in the pump capacity makes this phenomenon applicable in many industries [2]. In the oil and gas industry, drag reduction is used to improve process such as drilling operations, hydraulic fracturing, workover, well completions and wellbore cleanup [3]. For instance, during deep and horizontal drilling operations, due to the high circulating system pressure losses, high pump horse power is necessary to re-circulate the drilling fluid [4]. Thus, the circulating pressure losses can be reduced by adding drag reducers additives to the drilling fluid. Effective polymer drag reducers are substances composed of linear molecules with high molecular weight which are soluble in water and oil based solvents [4].

[2]A version of this chapter has already been presented.
Rodriguez-Corredor, F.E., Bizhani, M., and Kuru, E., 2013, "An experimental investigation of turbulent drag reduction in concentric annulus using particle image velocimetry technique," Proceedings of the 32nd International Conference on Ocean, Offshore and Arctic Engineering, Technical paper. Nantes, France.

[3] Rodriguez-Corredor, F.E., Bizhani, M., and Kuru, E., 2013, "An experimental study of the effect of drag reducing additive on the structure of turbulence in concentric annular pipe flow using particle image velocimetry technique," ASME 2013 International Mechanical Engineering Congress & Exposition (IMECE), Technical paper. San Diego, California, US.

Drag reduction is defined as a reduction in the skin factor in turbulent flow when adding polymer additives to the fluid [5,6]. Even though this effect has been proven to be useful in many industrial applications, the drag reduction is especially beneficial for the fluid transportation by pipes and channels. Therefore, drag reduction is defined in terms of the pressure drop at the same flow rate as follows [6]:

$$\%DR = \frac{\Delta P_s - \Delta P_p}{\Delta P_s} * 100\% \quad (1)$$

Where ΔP_s is the pressure drop encountered when pumping the solvent only and ΔP_p is the pressure drop encountered when pumping the solvent with polymer [6].

There are many factors that influence the drag reduction effectiveness. Kamel et al., [7] conducted drag reduction experiments in straight circular pipes using two anionic polyacrylamides; an analog of partially hydrolyzed polyacrylamide (PHPA) and a sulfonate-containing polyacrylamide. They studied the influence of the Reynolds number and the polymer concentration on the drag reduction. Kamel et al., [7] found that the drag reduction is enhanced by increasing the polymer concentration. However, this behaviour continues until achieving an optimum value where the maximum drag reduction is obtained. Beyond this value of optimum concentration, the drag reduction decreases because the increase in the fluid viscosity superposes the reduction in the turbulence intensities [7,8]. Kamel et al., [7] also found that the drag reduction increased with the increasing solvent Reynolds number. However, as in the case of the concentration, beyond a critical value of Reynolds number, the drag reduction is decreased because after exceeding a certain value of shear stress, the polymer fibres start to degrade [7,8].

Dschagarowa et al., [9] showed that the drag reduction is enhanced by using polymers with higher molecular weight, reaching values up to 2x10^6. In a follow up work, Dschagarowa et al., [10] also suggested that for lower values of molecular weight a high value of concentration is required to obtain a significant drag reduction.

Polyacrylamides derivatives have gained a great interest as drag reducers. Camail et al. [11] experimentally studied the effectiveness of three different drag reducers; poly-ethyleneoxide (PEO), polyacrylamide (PAM) and PAM derivatives. They found that although the PEO and PAM present higher values of drag reduction, their effectiveness is decreased in few hours, reaching a zero value of drag reduction in short time [11]. On the other hand, the PAM derivatives present smaller values of drag reduction compared with the maximum values obtained by using PEO and PAM, but their drag reduction effectiveness has only a small drop until the end of the experiment which was 80 hours [11]. This makes these kinds of polymer more efficient. Thus, in order to explain these two types of behaviors, Camail et al. [11] suggested a mechanism, which involves three principal steps. In the first step, the solvation of the solids takes place and there is no drag reduction. During the second step, the isolated coils are extracted from the aggregates and as a result, energy is dissipated by this way, decreasing the turbulent energy dissipation; therefore, drag reduction is observed. The third step involves the stretching of the macromolecules chains. After the isolated coils are separated from the aggregates, there are two types of isolated coils obtained. The first types are molecules with low intramolecular interactions. In this case, the stretching energy achieved is below the critical energy level and no drag reduction is presented. This is the case of PEO and PAM molecules [11]. However, the second types of molecules have large intramolecular interactions and the stretching energy produced is above the energy critical level, being large enough to generate drag reduction. This is the case of PAM derivatives [11]. Thus,

PAM derivatives, as partially hydrolyzed polyacrylamide (PHPA), have been used as very efficient polymer additives in drag reduction applications.

Since Toms discovered the drag reduction in 1948, many researchers have been proposing different mechanisms in order to explain this phenomenon. For instance, Sher et al., [12] proposed a mechanistic model based on a force balance on a polymer molecule in a turbulent flow field. It was argued that the dominant forces on a polymer fibre in the turbulent field are elastic restoring forces and centrifugal stretching forces [12]. Thus, it was suggested that the total dominant eddies dissipation in a polymer suspension is the sum of the dissipation in the pure solvent and the energy dissipation by the stretching and damping of polymer fibres [12]. Therefore, a new route of energy dissipation (in which a periodical coil elongation and relaxation take place) exists and less energy is dissipated by the route of turbulence [12].

Japper-Jaafar et al., [13] experimentally studied the drag reduction in concentric annulus using the Laser Doppler Anemometry technique. They found that for the drag reducing fluid, the axial mean velocity profile follows the universal wall law ($y^+=u^+$) for $y^+<10$. However, it deviates (with an increasing slope) from the velocity profile obtained for the Newtonian case in the log wall region ($y^+>30$) [13]. They were not able to observe the effect of the drag reducers on the radial location of the maximum velocity. Therefore, more study in the topic is required. Japper-Jaafar et al. [13] also found that there is a significant decrease in the radial turbulent intensities by adding polymer to the flow. The axial turbulent intensities were also affected by the polymer molecules. Higher peak values of axial turbulent intensities were obtained as the drag reduction was increased [13].

Warholic et al., [14] measured fluctuating velocity fields during channel flow of water and drag reducing fluid. The main conclusion was that the polymer molecules make the flow to become more parallel to the wall [14]. Additionally, less chaotic, less extensive and less frequent large scales eruptions were found in the polymer fluid flow case. They concluded that the near wall activities producing turbulence was strongly affected by adding drag reducing additives [14].

Ptasinski et al., [15] studied the effect of polymer addition on the kinetic energy budget of turbulent pipe flow. A significant decrease in the viscous dissipation and production terms was reported.

In this study, the drag reduction phenomenon during turbulent flow of water through concentric annulus was investigated using Particle Image Velocimetry technique and partially hydrolyzed polyacrylamide (PHPA) as drag reducing agent. Data is presented to show the influence of adding drag reducing agent on the mean axial velocity profile, radial position of maximum velocity and radial Reynolds shear stress distribution. Analyses and discussions are also presented including the shear production and viscous dissipation term in the kinetic energy budget as well as the vorticity, which have not been extensively studied in the past for the concentric annular flow case.

5.2 Experimental Program

Detailed description of all the facilities and equipment used for experiments were described in the Chapter 2. Methodology of PIV measurement and data analyses were discussed in the Chapter 3.

5.2.1 Fluid Preparation and Characterization

A high molecular weight partially hydrolyzed polyacrylamide (PHPA) provided by M-I SWACO Canada was used as drag reducer. The main PHPA properties are presented in Table 5-1 [16]:

Table 5 - 1. PHPA Properties (Taken From Poly-Plus Rd Catalogue) [16]

Physical appearance	White granular powder
Odor	Slightly Hydrocarbon
Specific gravity	1.25 – 1.40
pH (1% Solution)	7.7
Bulk Density	641 – 737 kg/m^3
Nature of Charge	Anionic
Activity	>90%

The polymer solution was prepared by using the procedure recommended by Wyatt et al. [17]. Initially, a concentrated solution was prepared by adding polymer slowly to the mixing tank filled up with water at room temperature. The mixer was operated at 30 RPM to avoid degradation of the polymer fibres. The solution was allowed to rest for 24 hours and after that, it was diluted to desired final concentrations (0.07%, 0.10%, 0.12%) and pumped through the flow loop. In order to guarantee that the solution was properly mixed and totally transparent, it was allowed to re-circulate through the loop for 20 minutes. After that, both PIV and pressure drop measurements were taken.

5.3 Results and Discussions

5.3.1 Polymer Fluid Rheology

The polymer solution was characterized using a high resolution controlled stress ARG2 rheometer [18]. All the polymer solutions were found to be exhibiting Power Law behaviour as observed in figures 5-1, 5-3 and 5-5. Viscosity versus shear rate data is presented in figures 5-2, 5-4 and 5-6 for 0.07, 0.1 and 0.12 %V/V PHPA respectively Table 5-2 shows the power law parameters for the three solutions studied.

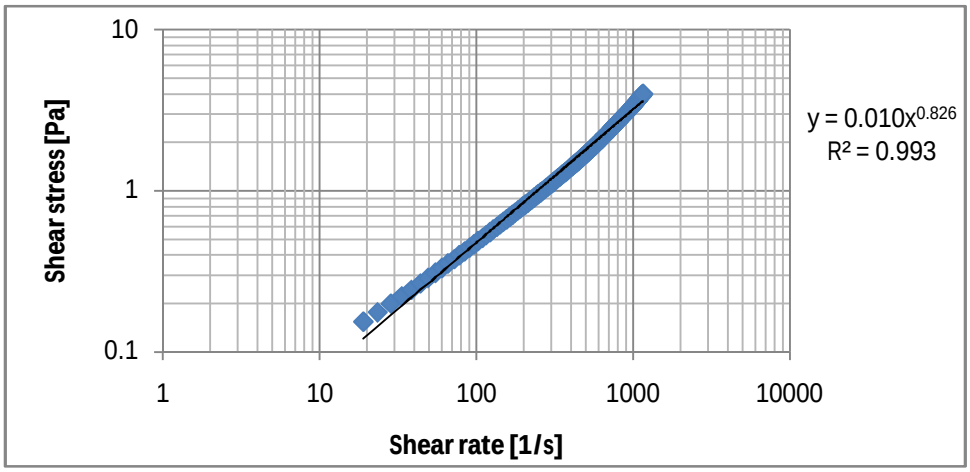

Figure 5 - 1. Shear Stress versus Shear Rate for 0.07% V/V PHPA Solution.

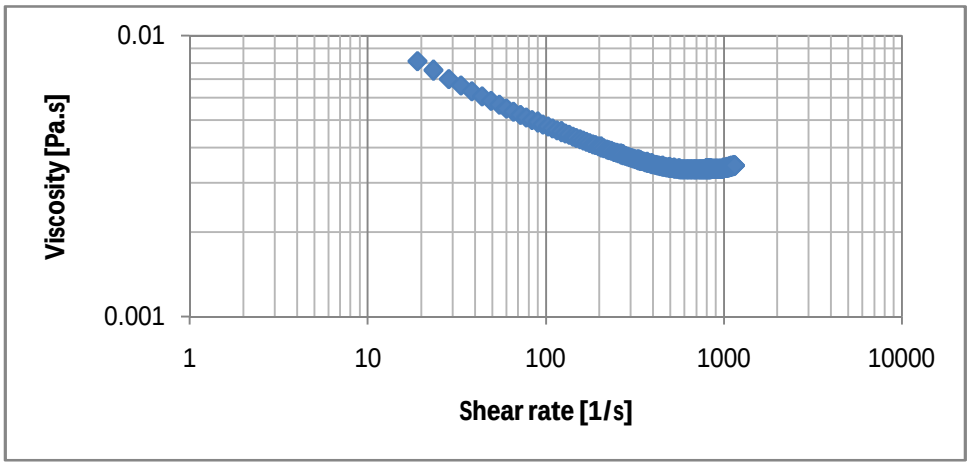

Figure 5 - 2. Viscosity versus Shear Rate for 0.07% V/V PHPA Solution.

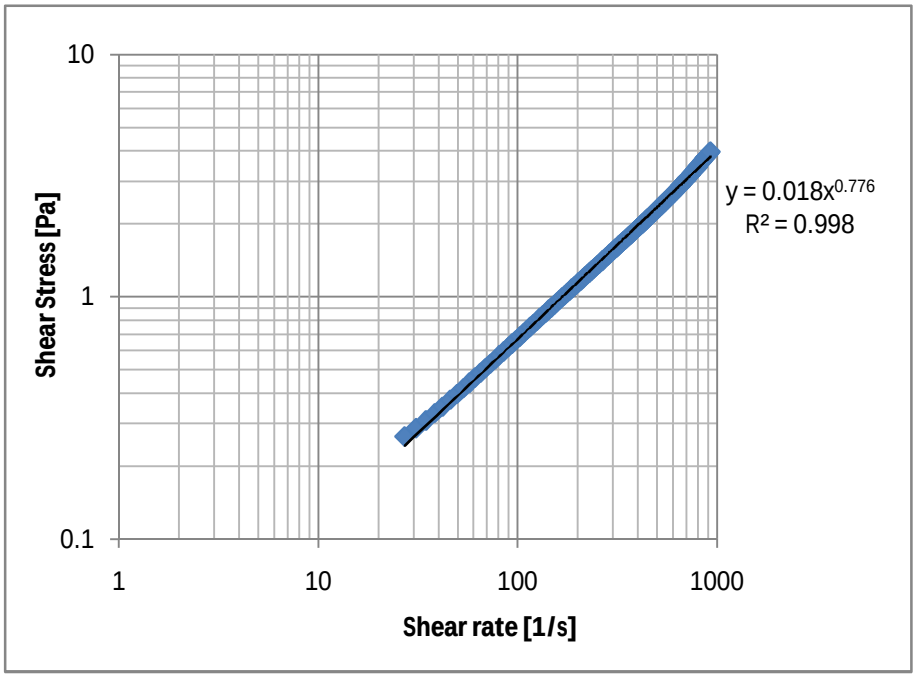

Figure 5 - 3. Shear Stress versus Shear Rate for 0.1% V/V PHPA Solution.

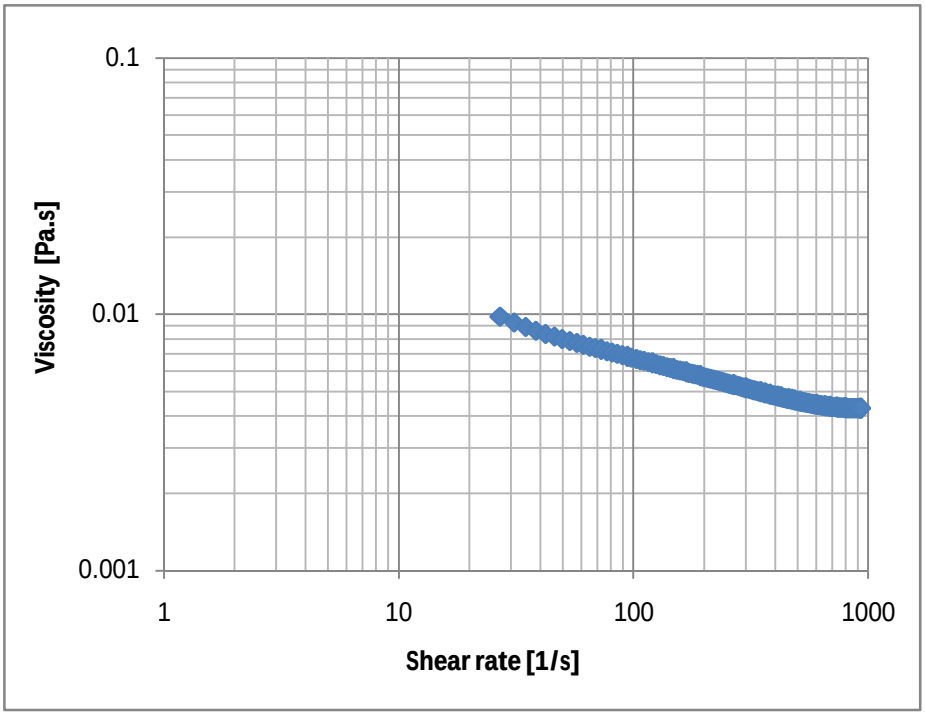

Figure 5 - 4. Viscosity versus Shear Rate for % V/V PHPA Solution.

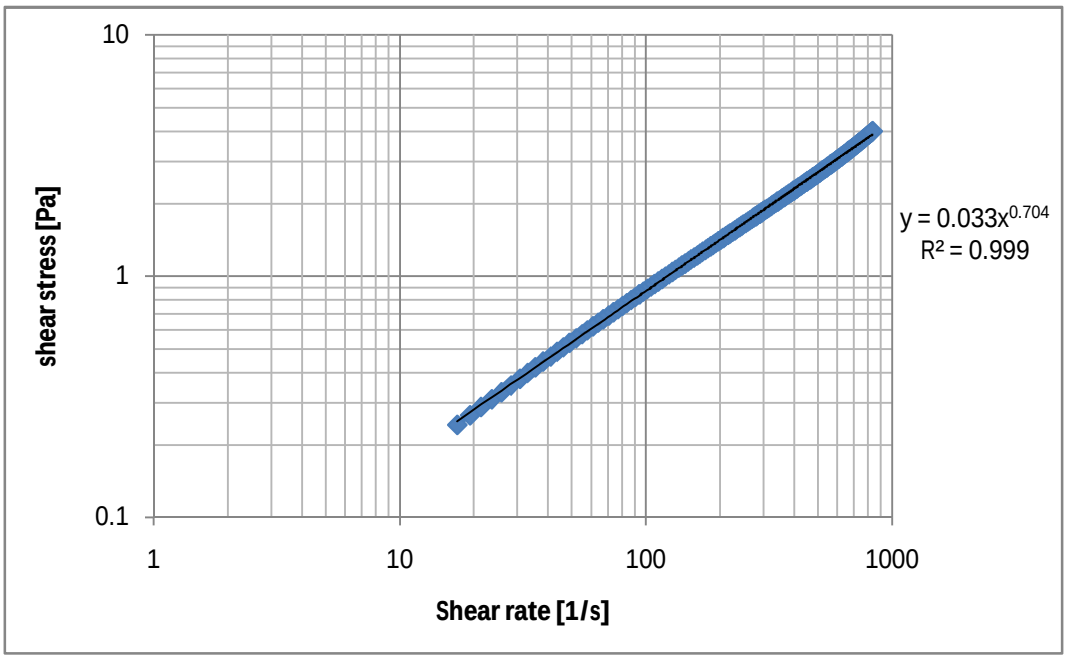

Figure 5 - 5. Shear Stress versus Shear Rate for 0.12% V/V PHPA Solution.

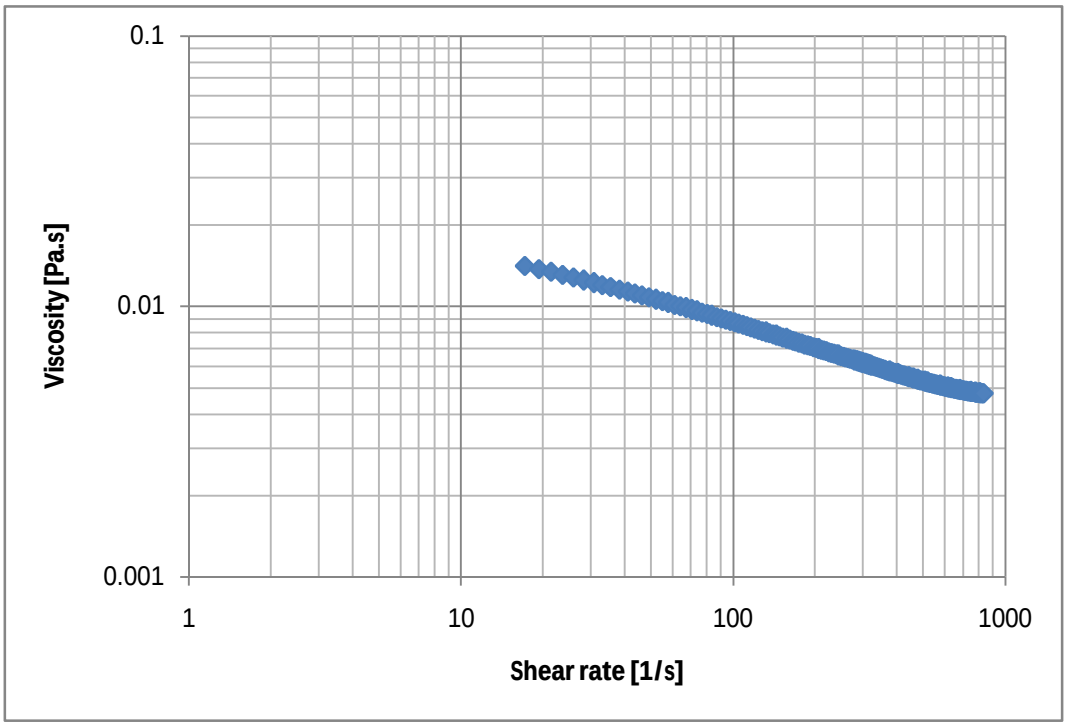

Figure 5 - 6. Viscosity versus Shear Rate for 0.12% V/V PHPA Solution.

Table 5 - 2. Power Law Parameters for the Polymer Solutions Studied.

Concentration [%V/V]	K	n
0.07	0.010	0.826
0.1	0.019	0.776
0.12	0.033	0.704

5.3.2 Drag Reduction Experiments

Preliminary experiments were conducted to determine the effect of polymer concentration on the drag reduction. Three different polymer concentrations were used for conducting this study as 0.07, 0.1 and 0.12%V/V.

Experiments were also conducted at three different solvent Reynolds numbers as 38700, 46700, and 56400. Figure 5-7 shows the results of all drag reduction experiments.

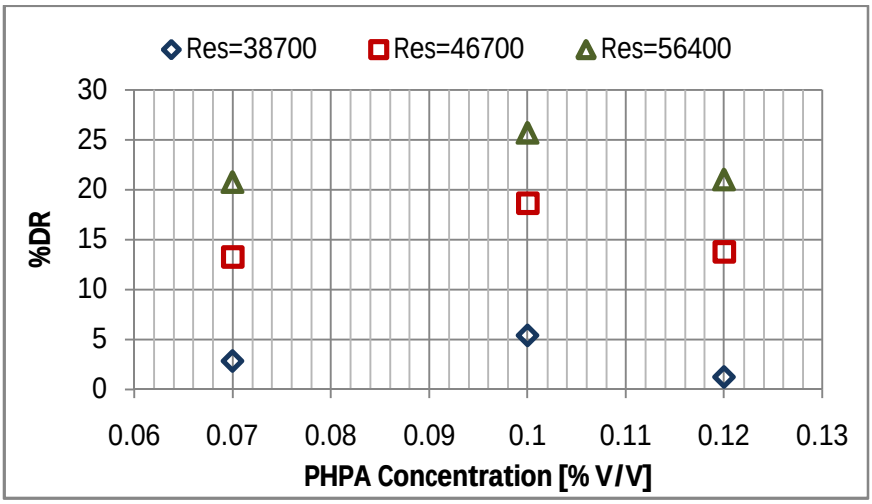

Figure 5 - 7. Drag reduction Versus Polymer Concentration at Different Reynolds Number.

The effect of the concentration is such that increasing the concentration caused more drag reduction until the polymer concentration reached an optimum value of concentration.

The optimum value of polymer concentration was 0.1 %V/V for all the Reynolds numbers studied. Beyond this optimum value, the drag reduction decreased due to the increase in the fluid viscosity, which makes the wall shear stress higher than the wall shear stress observed when using the optimum value of concentration.

The drag reduction is enhanced as the solvent Reynolds number is increased from 38,700 to 56,400. Within the ranges of the Reynolds numbers studied, the highest drag reduction was obtained using a polymer concentration of 0.1%V/V, at a solvent Reynolds number equal to 56400. A maximum drag reduction of 26% was achieved in this case.

5.3.3 Friction Factors

Friction factor was calculated by using Eqn. 2 as suggested by Shah and London [19] and Escudier et al. [20]:

$$f = \frac{2\tau_A}{\rho U^2} \tag{2}$$

Where ρ is the fluid density, U is the bulk velocity and τ_A is the weighted average wall shear stress. The weighted average wall shear stress is calculated by using Eqn. 3 [19-20]:

$$\tau_A = \frac{1}{4}(D_2 - D_1)\frac{dP}{dx} \tag{3}$$

Where D_2 is the inner diameter of the outer pipe and D_1 is the outer diameter of the inner pipe.

Figure 5-8 shows the friction factor obtained for water and for a polymer solution (0.1%V/V concentration) at three different solvent Reynolds numbers; 38700, 46700, and 56400. Theoretical values of friction factors for fully developed laminar and turbulent

flow of water were calculated using the model given by Jones and Leung [21] and provided here for comparison purpose:

Laminar flow (Water) [21]:

$$f = \frac{16}{Re^*} \tag{4}$$

Where Re^* is the modified Reynolds number calculated as follows:

$$Re^* = \frac{\rho U d_l}{\mu} \tag{5}$$

Here d_l is defined as an equivalent diameter which depends on the geometric shape factor ∅:

$$d_l = (D_2 - D_1) * \emptyset \tag{6}$$

$$\emptyset = \frac{1}{(1-a)^2}\left[1 + a^2 - \frac{1-a^2}{\ln\frac{1}{a}}\right] \tag{7}$$

Where a is the inner to outer radius ratio ($=r_1/r_2$).

Turbulent Flow (Water):

In the turbulent water flow, the Colebrook equation written in terms of the modified Reynolds number was used [21, 22]:

$$\frac{1}{\sqrt{f_D}} = 2.0\log_{10}Re^*\sqrt{f_D} - 0.8 \tag{8}$$

Here, f_D is the Darcy friction factor.

Laminar Flow (Polymer fluid):

The friction factor for laminar flow of polymer fluid can be calculated following the approaches given by Shah and London [19] and Escudier et al. [20] for power law fluids:

$$\frac{f}{Re_w} = 23.9\left(\frac{2n+1}{3n}\right) \tag{9}$$

Where Re_w is calculated using the viscosity at the wall (μ_w) and the hydraulic diameter as follows [19, 20]:

$$Re_w = \frac{\rho U(D_2 - D_1)}{\mu_w} \tag{10}$$

Friction factors calculated for all three polymer fluid flow experiments are shown in Figure 5-8.

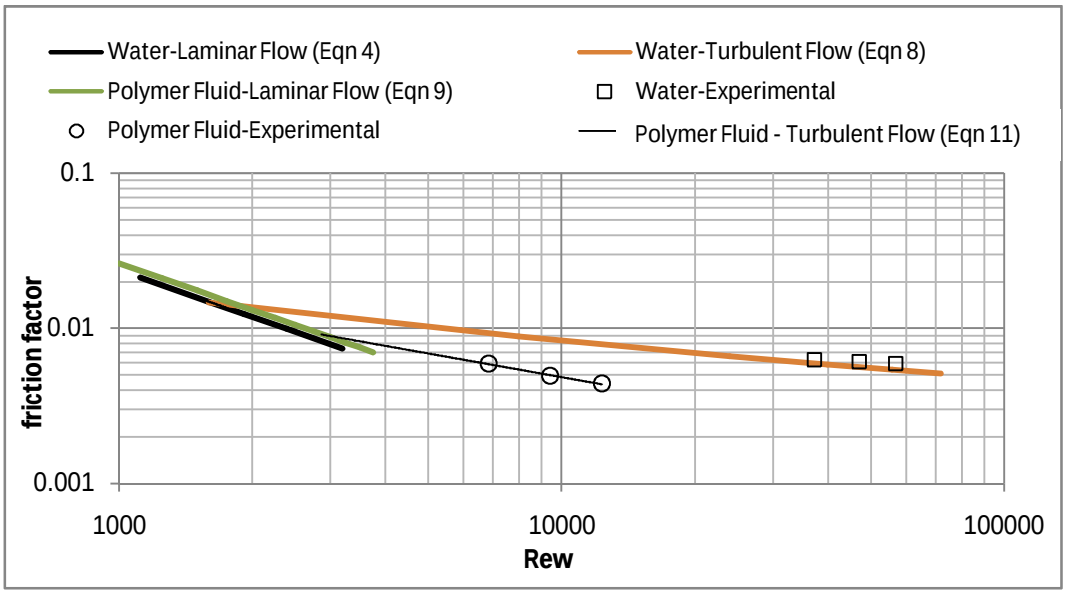

Figure 5 - 8. Friction Factor Obtained for Water and Polymer Solution at Optimum Concentration (0.1%V/V).

The friction factors for polymer flow in the turbulent zone were found to be smaller than that of water flow, showing the drag reduction effect. Additionally, the friction factor was found to be decreasing significantly with the increase in the Reynolds number. For the turbulent water flow, the friction factor values matched the values calculated using Jones and Leung correlation.

The slope of the *f*-Re line passing through the experimental data points is significantly different from the theoretical *f*-Re line given for laminar polymer fluid flow, indicating that the flow conditions for these experiments were fully turbulent.

Based on the theoretical *f*-Re curve given for laminar flow of polymer fluid and the *f*-Re curve based on the experimental data for turbulent polymer flow, the transition from laminar to turbulent flow seems to take place at approximately Re_w=3000.

The slope of the *f*-Re curve for the turbulent polymer fluid flow is also significantly lower than that of the water flow, indicating that the addition of polymer fibres affects the flow by decreasing the wall shear stress and consequently, the frictional pressure drop is reduced.

An empirical correlation for calculating the friction factor as a function of the Reynolds number for the turbulent flow of polymer fluid was obtained as follows:

$$f = 0.519 Re_w^{-0.50} \quad (11)$$

5.3.4 Turbulent Flow Experiments Using 2D-PIV

The effect of the polymer addition on the mean flow velocity, turbulent statistics and the turbulent structure will be discussed in the following section.

5.3.4.1 Axial Mean Velocity Profile

Axial velocity profiles were measured for water and for the three polymer solutions at three different solvent Reynolds numbers: 38700, 46700 and 56400. The velocity profile data in the region close to the wall was plotted in dimensionless wall coordinates (u^+ vs y^+) as explained in chapter 4.

Figures 5-9 shows how the velocity profile changes with the polymer concentration. In this case, the solvent Reynolds number (Res) is 56400 and data obtained near the inner wall is shown. The slope of the velocity profile line in the logarithmic zone increases with increasing polymer concentration. However, the velocity profiles for 0.01 and 0.12%V/V were very similar, being slightly higher for the optimum value of concentration (0.1%V/V).

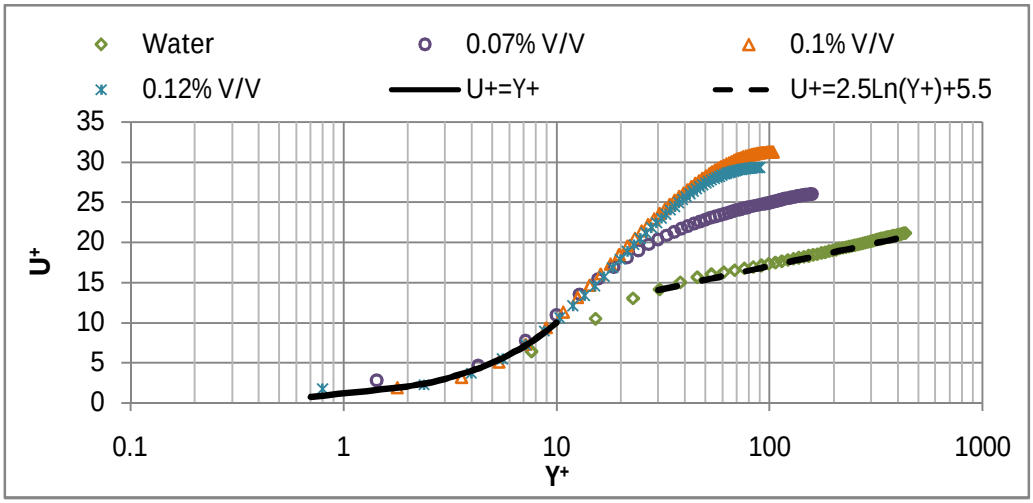

Figure 5 - 9. Effect of the Polymer Concentration on the Axial Mean Velocity Profile – Inner Wall (Res=56400).

Figure 5-10 shows how the velocity profile changes with increasing solvent Reynolds number at constant polymer concentration. The velocity profile line is shifted up in the logarithmic zone as the solvent Reynolds number increases showing that the drag

reduction is enhanced with an associated increase in the velocities in the turbulent core region.

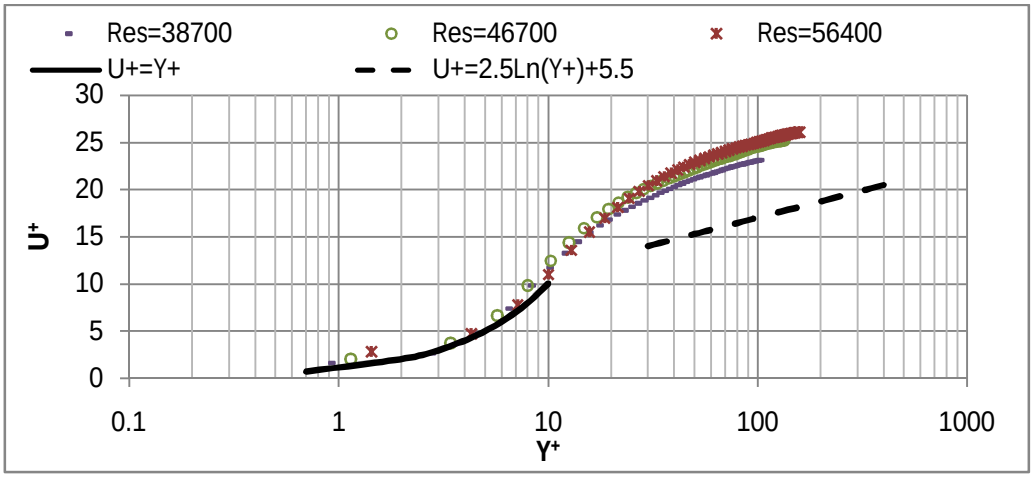

Figure 5 - 10. Effect of Varying the Solvent Reynolds Number on the Velocity Profile (Inner Wall Data - Polymer Concentration; 0.07%V/V).

A comparison of the velocity profile in log-wall region near the inner and the outer pipe walls is presented in figure 5-11. Here, the solvent Reynolds number is 56,400 and the polymer concentration is 0.1% V/V. For comparison purpose, the Virk's maximum drag reduction asymptote [26] is also included in figure 5-11. This asymptote is produced according to Virk et al. [26] for y+>30:

$$u^+ = 11.7\ln(y^+) - 17.0 \qquad (13)$$

The velocity profile near the inner wall was found to be shifted up with an increasing slope and closer to Virk's maximum asymptote compared to the velocity profile near the outer wall, which indicates that more drag reduction exists near the inner wall. Similar results were also reported by Japper-Jaafar et al.,[13].

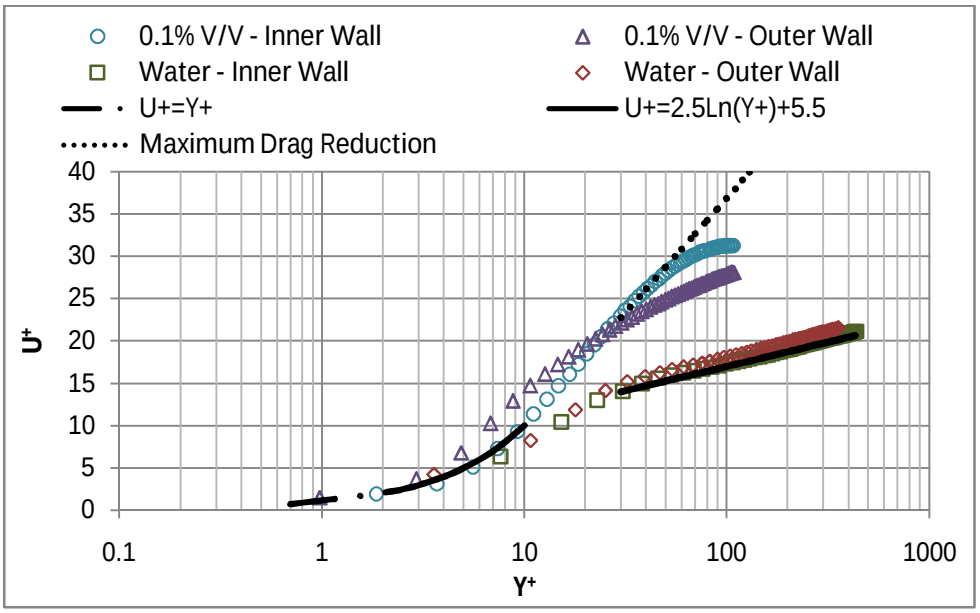

Figure 5 - 11. Comparison of the Velocity Profile Near the Inner and Outer Pipe Walls (Res: 56400).

As observed in figures 5-9 to 5-11, the velocity profile is composed of three different zones. The first zone is the viscous sub-layer ($y^+<10$) where the viscosity of the fluid controls the motion [25]. In this zone, both water and polymer fluid velocity profile follows the universal law of the wall ($u^+=y^+$). The second zone is known as logarithmic zone, where no influence on the motion is attributed to the viscosity because of the fact that the viscous scales are so small and the pipe radius is sufficiently large [26]. The shape of the velocity profile in this region is logarithmic, and for water (Newtonian fluid), it follows the log law ($u^+=2.5\ln(y^+)+5.5$). For the polymer fluid flow case, the shape of the velocity profile also remains logarithmic [25-26]. However, the slope of the velocity profile of polymer fluid flow is higher than that of water, showing that drag reduction is taking place [25-26].

The zone between the viscous sub-layer and the logarithmic zone is referred as the buffer zone. As shown in figure 5-11, the thickness of the buffer zone for polymer fluid flow is

much higher than that of observed in water flow. Lumley et al [25] suggested that the drag reduction occurrence is mostly related to changes in the buffer zone [25]. This will be discussed in detail when analyzing the production term in the turbulent kinetic energy budget.

5.3.4.2 Radial Position of the Maximum Velocity and Reynolds Shear Stress Distribution

Experimental results presented in chapter 4 confirmed that in turbulent water flow the radial variation of the total shear stress in concentric annulus is non-linear. That is; the wall shear stress is different at the inner and outer walls [27]. The position of the zero shear stress was closer to the inner wall [27]. The radial position of the zero shear stress was shown to be different than the position of the maximum velocity, on the average by about 2% [27].

The PIV technique implemented, allows obtaining many points in the core flow region and also acquiring images without a significant scatter; therefore, the radial position of the maximum velocity and the Reynolds stress distribution could be determined with an acceptable accuracy. Once the time average velocity field and Reynolds stress ($-\rho\overline{u'v'}$) are obtained for the three solvent Reynolds number studied, the data is averaged in the x direction and normalized using the bulk fluid velocity (U_b). Finally, the data is plotted against the dimensionless distance from the inner wall (E= [r-r_1] / r_2-r_1]) as shown in figures 5-12 to 5-18.

Figures 5-12, 5-13 and 5-14 show comparison of Reynolds stress distribution for flow of water and fluid with three different polymer concentrations calculated for Reynolds numbers 38700, 46700 and 56400, respectively.

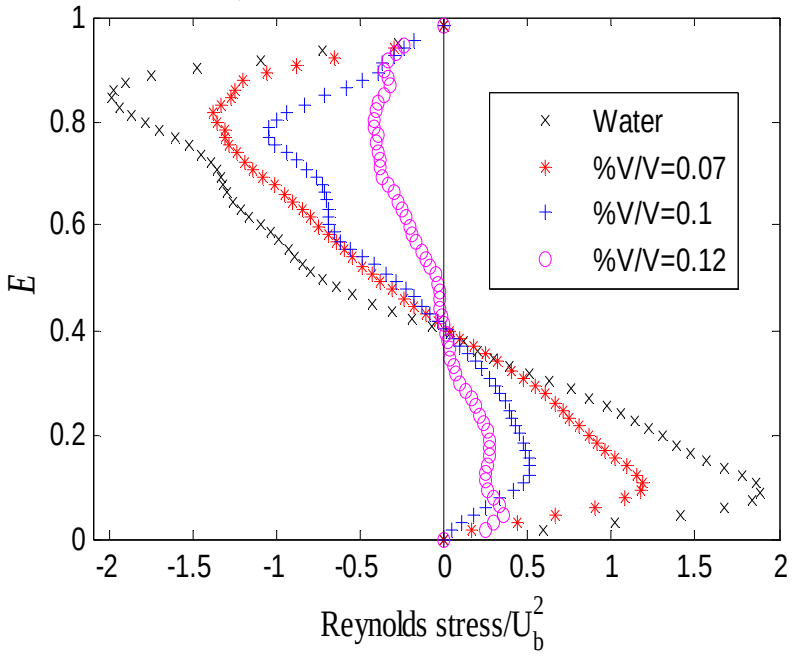

Figure 5 - 12. Reynolds Stress Distribution (Res=38700).

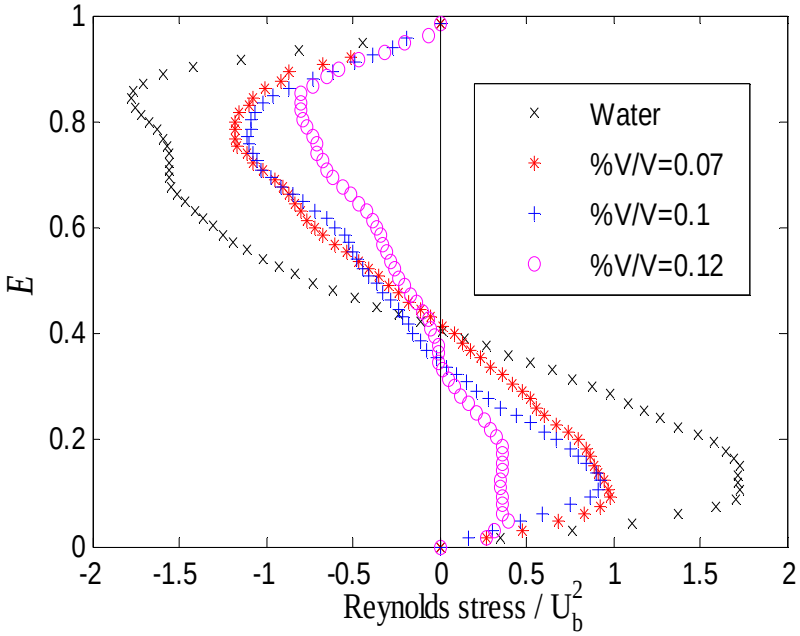

Figure 5 - 13. Reynolds Stress Distribution (Re=46700).

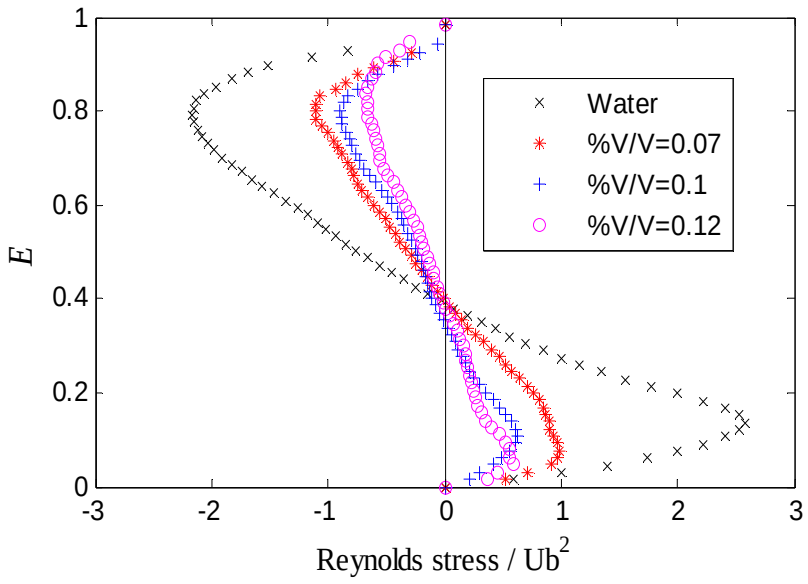

Figure 5 - 14. Reynolds Stress Distribution (Re=56400).

As observed in figures 5-12 to 5-14, for all of the polymer fluid flow cases, the Reynolds stresses are lower than the Reynolds stresses for water flow. The influence of the polymer concentration is such that there is a decrease in the Reynolds stresses distribution in the core flow region with the increasing polymer concentration; however, close to the wall, the optimum polymer concentration (0.1% V/V) results the lowest Reynolds stress which, also explains why the highest drag reduction was observed at this polymer concentration as reported earlier. The optimum polymer concentration in this case, is going to be the concentration that presents the lowest wall shear stress and consequently the lowest pressure drop. Therefore, the Reynolds stress distribution in the region close to the wall should be analyzed in detail.

Figure 5-15 shows the Reynolds stress distribution in the region close to the wall ($y^+<10$).

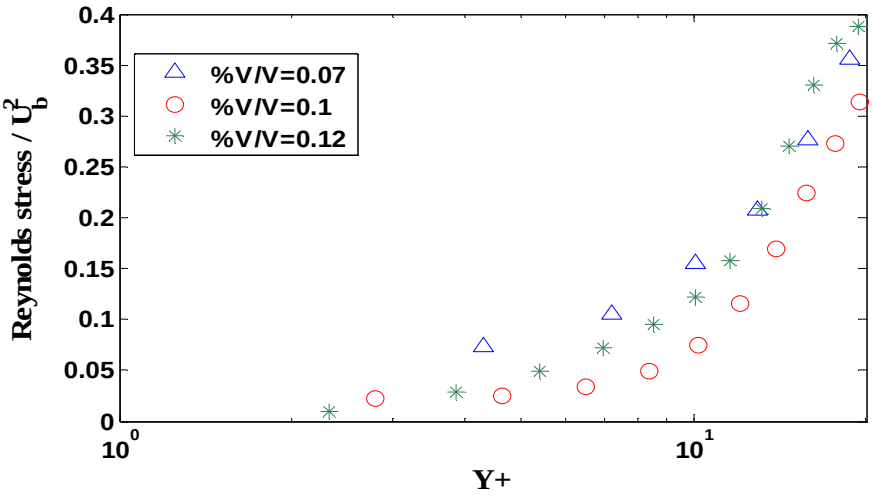

Figure 5 - 15. Effect of Polymer Concentration on the Reynolds Stress Distribution Near the Inner Pipe Wall.

The Reynolds stress is reduced as the polymer concentration is increased from 0.07% V/V to 0.10% V/V. However, increasing polymer solution concentration above the optimum value (0.1% V/V), does not create much reduction in the Reynolds stress. In fact, the Reynolds stresses for $5<y^+<10$ were found to be the lowest for 0.1%V/V, but it was almost the same in the near wall region ($y^+<5$) for polymer concentrations of 0.1%V/V and 0.12%V/V. The wall shear stress, however, will be greater for the 0.12%V/V than for 0.1%V/V case. This is because of the increased viscosity in the 0.12%V/V solution. Therefore, the total wall shear stress will be lower for 0.1% V/V, which also explains why 0.1%V/V is the optimum concentration giving the highest drag reduction.

The effect of polymer concentration on the axial velocity profile in the whole annular gap is also shown in figures 5-16, 5-17 and 5-18 for Reynolds number 38700, 46700 and 56400, respectively. In the core flow region, the velocity is higher for all of the polymer fluid flow cases as compared to the water flow. In addition, the maximum velocity achieved in the core flow region is increased with the increasing polymer concentration.

Figures 5-16, 5-17 and 5-18 also show that close to the wall, the polymer solutions presented lower velocities than the water case. Moreover, the flow of fluid with optimum polymer concentration (% 0.1 V/V) resulted the lowest velocity values close to the wall.

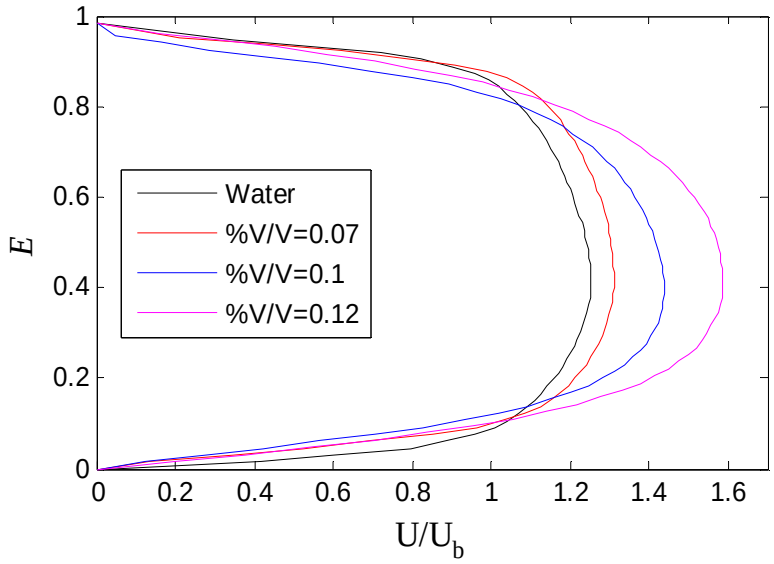

Figure 5 - 16. Axial mean Velocity Profile (Res=38700).

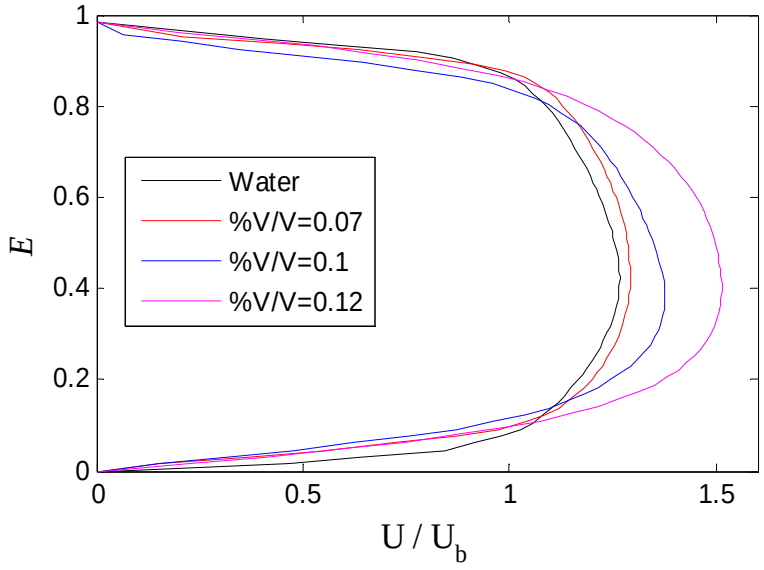

Figure 5 - 17. Axial mean Velocity Profile (Res=46700).

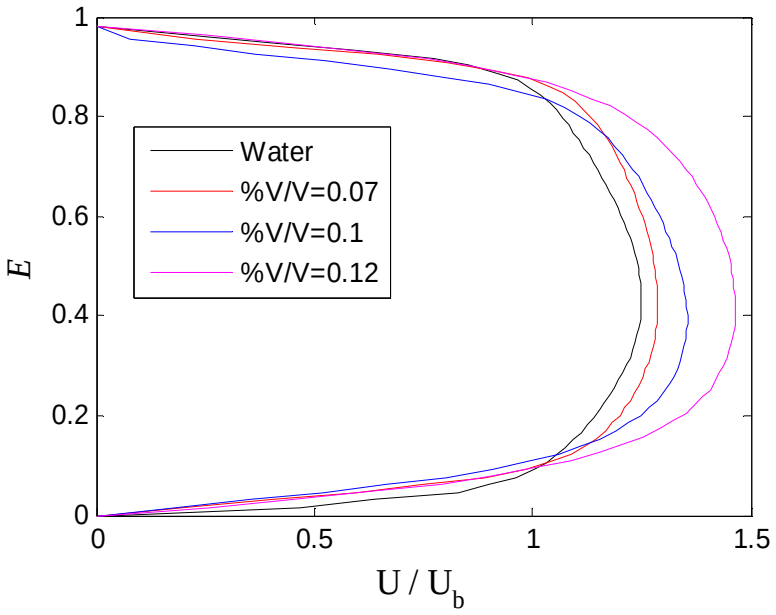

Figure 5 - 18. Axial mean Velocity Profile (Res=56400).

The radial locations of maximum velocity for all the Reynolds numbers and concentrations studied are summarized in Figure 5-19 and numerical values are listed in Table 5-3.

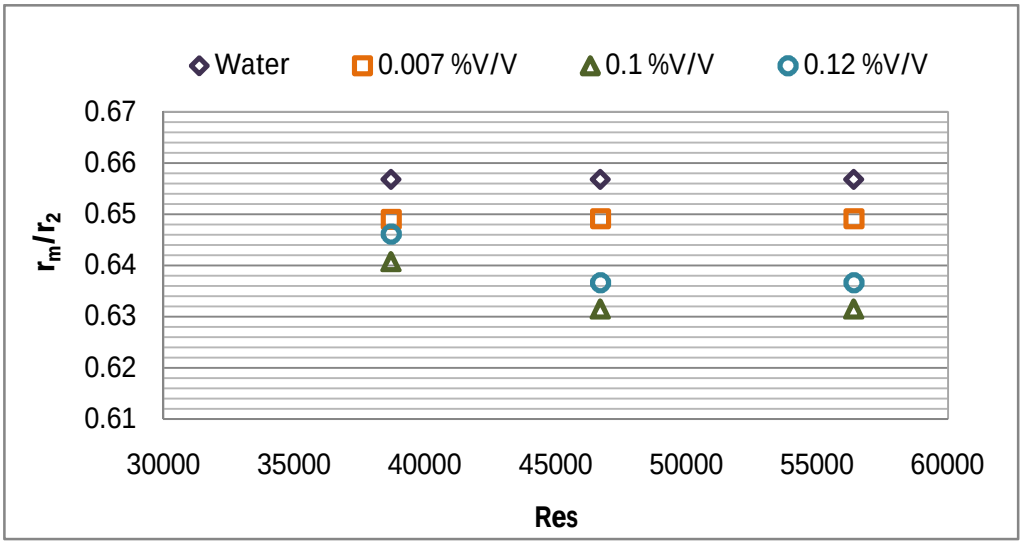

Figure 5 - 19. Comparison of the Radial Positions of the Maximum Velocity at Different Reynolds Number and Polymer Concentrations.

Table 5 - 3. Numerical Values of the Radial Positions of Maximum Velocity.

	Res=38701	**Res=46701**	**Res=56401**
Concentration %V/V	r_m/r_2	r_m/r_2	r_m/r_2
Water	0.66	0.66	0.66
0.07	0.65	0.65	0.65
0.1	0.64	0.63	0.63
0.12	0.65	0.64	0.64

It was found that with the addition of drag reducing agent, the position of the maximum velocity gets closer to the inner wall. However, the differences between the position of maximum velocity obtained for water and polymer fluid flow are more noticeable at higher values of drag reduction. For instance, at maximum drag reduction, (DR=26%, 0.1%V/V and Res=56400), there is a difference of around 0.3 r_m/r_2 (1.2 mm) between the locations of maximum velocity obtained for water and polymer fluid flow case.

5.3.4.3 Analyses of Second-order Turbulence Statistics and Turbulent Structure in Concentric Annulus

The following section is dedicated to analyze the second-order turbulence statistics and turbulent structure in concentric annulus using the results obtained by using a polymer solution with the optimum concentration (0.1% V/V). The optimum concentration was determined as the concentration yielding the highest drag reduction for the type of polymer used in this study. All the experiments were conducted at the same bulk velocity (U_b= 1 m/s), which gives a solvent Reynolds number equal to 56400. At these conditions, the drag reduction obtained was equal to approximately 26%. The velocity data to be used in the subsequent analyses were obtained using the PIV technique.

5.3.4.3.1 Turbulent Intensities

Figure 5-20 shows the root mean square (rms) of the axial velocity fluctuations. These values were non-dimensionalized using the shear velocity u_τ. In the region close to the wall (y^+<10), the rms values for the polymer fluid flow are similar to the rms values for water flow. Higher rms values were obtained for the polymer fluid flow between 10 and 60 wall units. The peak rms values obtained for the polymer fluid flow in the outer and inner wall were located at approximately 16 and 21 wall units, respectively. These results are in agreement with the results from the numerical simulation study performed by Sureshkumar et al., [28] and Dimitropoulos et al., [29] who found that in pipe flow, the maximum extension of the polymer takes place at 20 wall units.

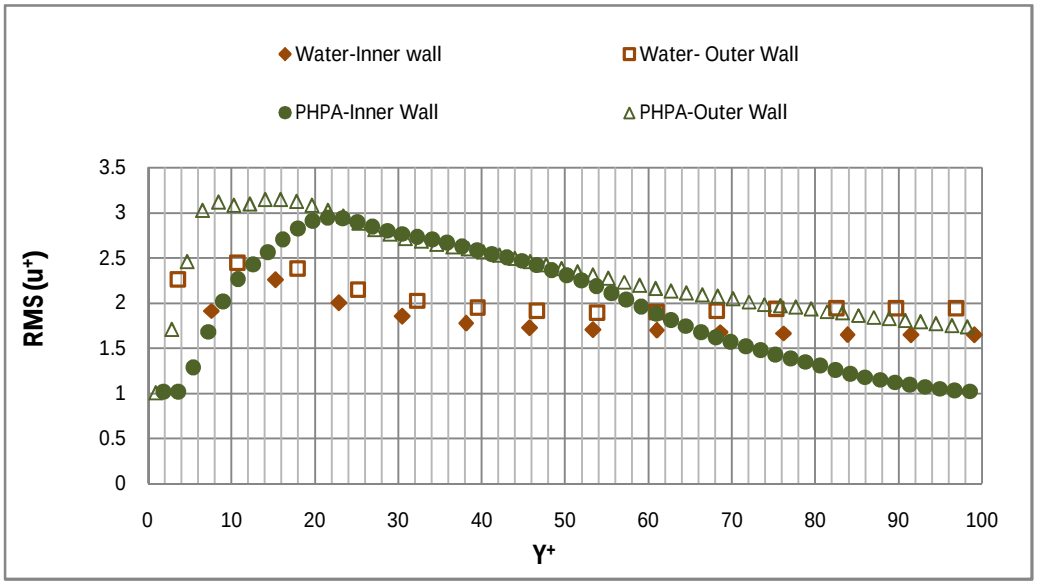

Figure 5 - 20. Axial Turbulent Intensities in Wall Coordinates (RMS[u+]=RMS [u']/u_t)

Figure 5-21 shows the root mean square of the radial velocity fluctuation in wall units. Generally, the radial turbulent intensities are reduced significantly in the polymer fluid flow except in the region close to the wall (y^+<10). However, close to the wall, a small decrease was obtained at the inner wall. This suggests that the velocity fluctuations

become more rectilinear after adding polymer to the flow especially in the zones further away from the wall. Similar results were also reported by Japper-Jaafar et al. [13], Ptasinski et al. [15], and Warholic et al. [14].

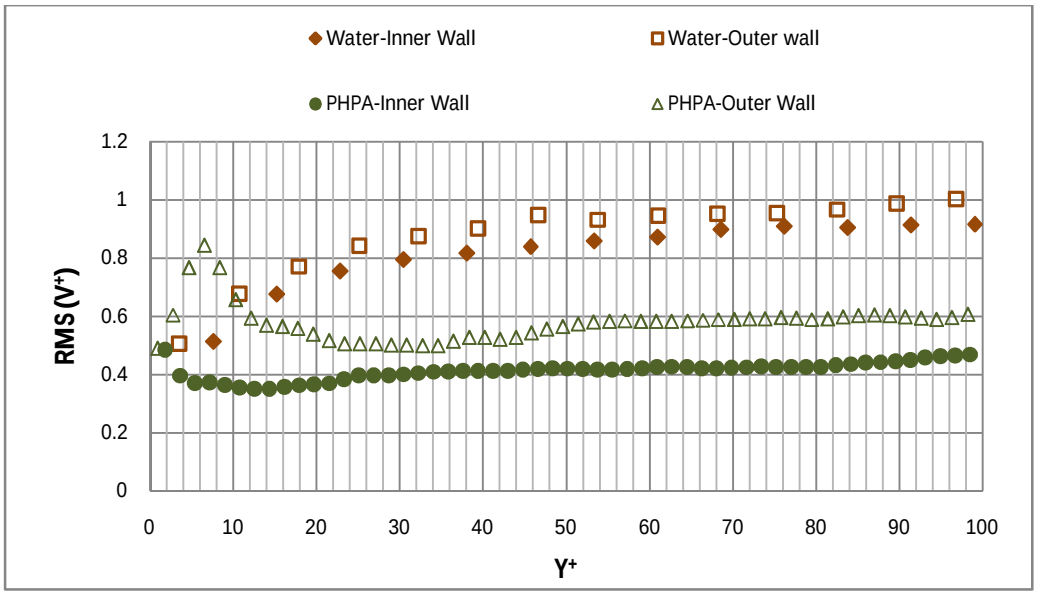

Figure 5 - 21. Radial Turbulent Intensities in Wall Coordinates (RMS[v+]=RMS [v']/u_t)

In general, axial and radial turbulent intensities at the outer pipe wall are higher than that of the inner wall. It is also noticeable that more reduction in the turbulent radial intensities takes place at the inner wall, suggesting that a higher contribution to the drag reduction comes from the inner wall. Similar results were also found by Japper-Jaafar et al. [15].

Results on turbulent intensities can be explained using the shear sheltering layer mechanism suggested by Hunt and Durbing et al., [30] and more recently by Ptansinski et al., [31]. They suggested that a shear sheltering layer exists in the buffer zone, where the large-scale eddies coming from the core flow are damped and blocked, so they can not easily approach the near wall region. When adding polymer to the flow, this shear sheltering layer mechanism is strengthened and the blocking of large-scale eddies

increases due the high polymer stretching rate [31]. Therefore, radial (normal to wall) velocity fluctuations are damped and reduced as shown in figure 5-21. Additionally, the breakdown of this shear layer is delayed since the natural Kelvin-Helmholtz instability is suppressed by the action of the polymer, as explained by Ptansinski et al [31]. This suppression of Kelvin-Helmholtz instabilities together with the strengthened blocking of eddies approaching the near wall region, result in amplification of the axial velocity fluctuations at the top of the buffer layer as shown in figure 5-20 [31].

5.3.4.3.2 Fluctuating Velocity Fields

Figures 5-22 and 5-23 are the examples of the local fluctuating velocity fields obtained for water and polymer fluid flow, respectively. The fluctuating velocity field profiles show that velocity values are more rectilinear for the polymer fluid than that of the case for water flow. This characteristic of the fluctuation velocity field is also supported by the reduced turbulent radial intensities observed in the polymer fluid flow.

In addition, more small scale motions are seen in the fluctuation velocity field of water. Comparing the fluctuating velocity fields obtained for water and polymer fluid flow, it can be seen that the dampening of the small scale motions and radial fluctuations produces an important effect on the near wall activities producing turbulence. Therefore, the sweeps and bursts that can be seen for the polymer fluid flow are less chaotic, less frequent and with less extension than that of the water flow. These reductions will have an impact on the Reynolds stress which is decreased significantly.

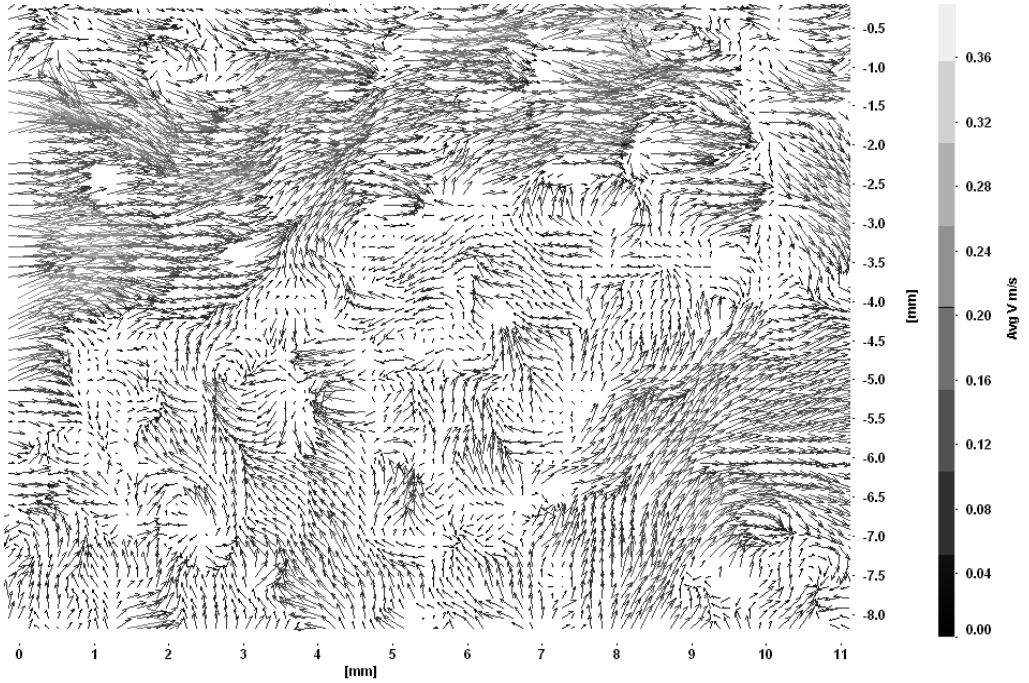

Figure 5 - 22. Example of the Local Fluctuating Velocity Field Obtained for Water Flow

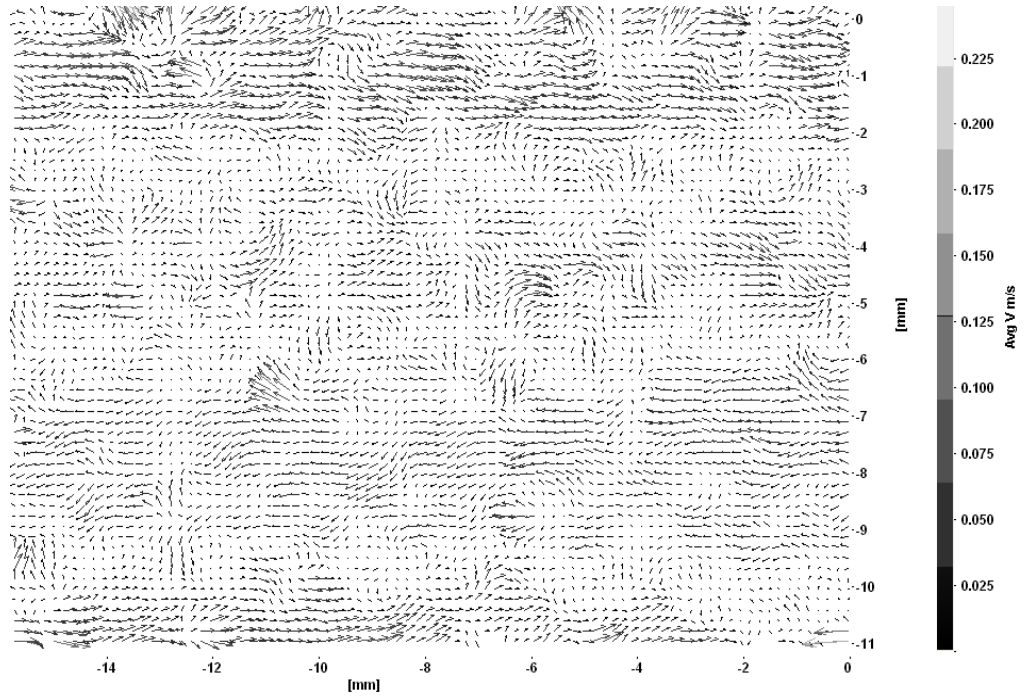

Figure 5 - 23. Example of the Local Fluctuating Velocity Field Obtained for Polymer Fluid Flow

5.3.4.3.3 Reynolds stresses

Reynolds stresses close to the inner and outer walls are shown in figure 5-24. A strong decrease in the Reynolds stress is obtained after adding polymer to the flow. In the region close to the wall, it is reduced to a value very close to zero. Similar results were also shown previously by Warholic et al., in channel flow [14]. Another important effect is that for the polymer fluid flow, the location of the peak value is closer to the wall than that of water flow. The height of the peak is smaller for polymer fluid flow case. Moreover, the magnitude of the Reynolds stress is generally higher at the outer wall.

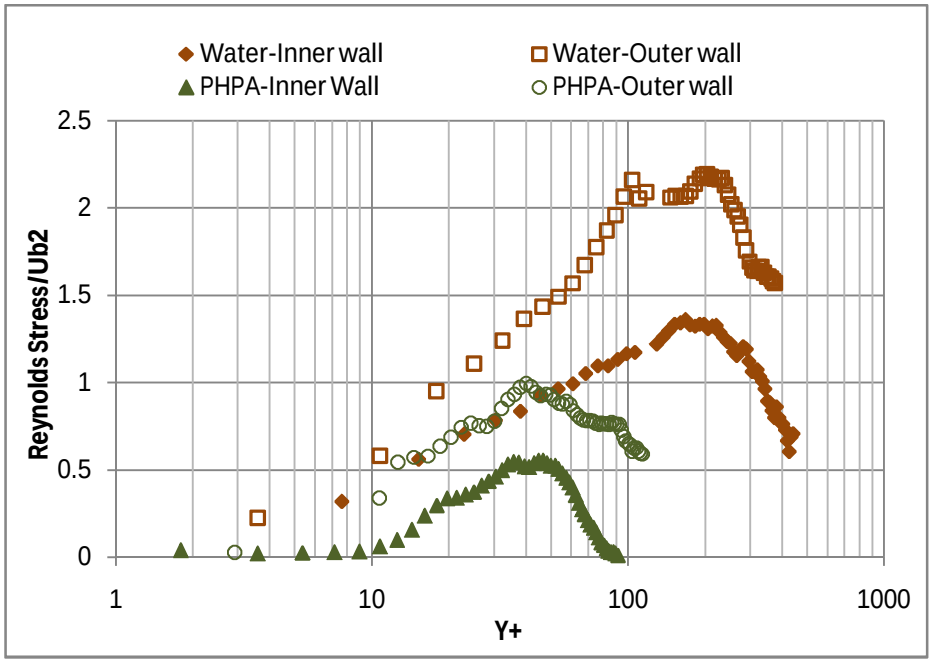

Figure 5 - 24. Reynolds Stress Results for Water and Polymer Solution.

The significant reduction in the Reynolds stress (Figure 5-24) during drag reduction applications is known as “Reynolds stress deficit” [31-32]. Reynolds stress reductions are mainly due to the decrease in the fluctuating velocity components, which leads to a decrease in the -u’v’ values. The biggest contribution to the Reynolds stress reductions is

provided by the radial component of the fluctuating velocity. As shown by the radial turbulent intensities results (Figure 5-21) and by the fluctuating velocity fields (Figures 5-22 and 5-23), the radial component is decreased significantly when adding polymer to the flow.

5.3.4.3.4 Averaged Vorticity

Vorticity is another important parameter to study in the structure of turbulence. This can be linked to the production of turbulence. The vorticity calculation in the xy plane is performed using the central difference scheme with the four closest neighbours as described in chapter 4

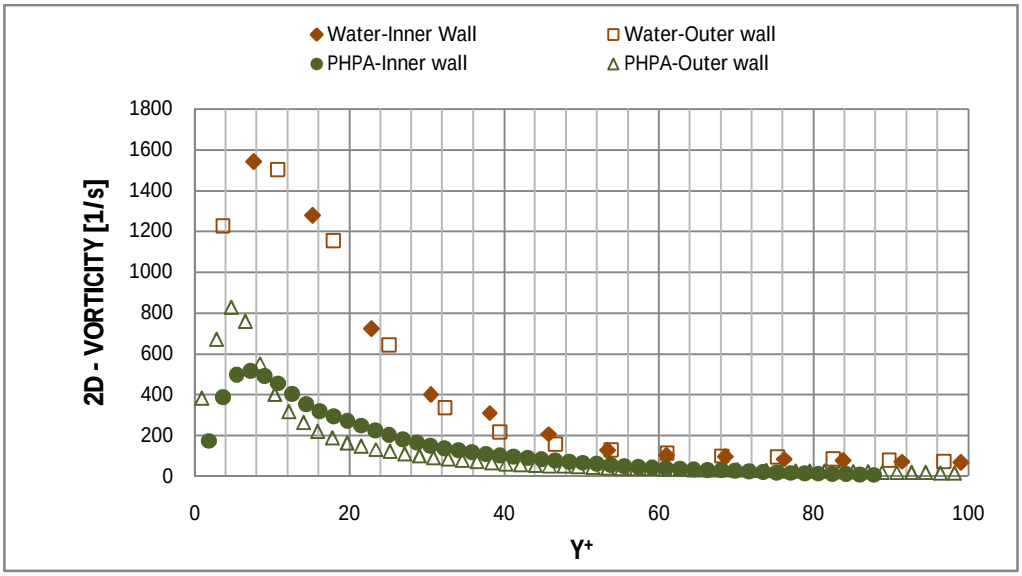

Figure 5 - 25. Results of the 2D Vorticity for Water and Polymer Solution.

Figure 5-25 shows the impact of polymer addition on the vorticity. Higher peak values are obtained for water flow. The vorticity decreased significantly as the polymer is added to the flow. The location of the peaks in all cases lies in the viscous sub-layer. As we move further away from the wall, the vorticity is decreased until achieving a value close to zero in both water and polymer fluid flow. For water, it was found that the vorticiy is

almost the same at both walls. However, by adding polymer, more reduction in the vorticity takes place at the inner wall.

Reductions in the vorticity values can be linked to the fluctuating velocity fields. As discussed previously, the decrease in radial fluctuating component of the velocity makes the flow to become more parallel to the pipe walls as shown in figure 5-23, reducing the radial velocity gradients along the x direction. As a result, the first term on the right hand side of the equation 12 presented in chapter 4 becomes smaller and consequently a decrease in the vorticity is obtained.

5.3.4.3.5 RMS of Vorticity

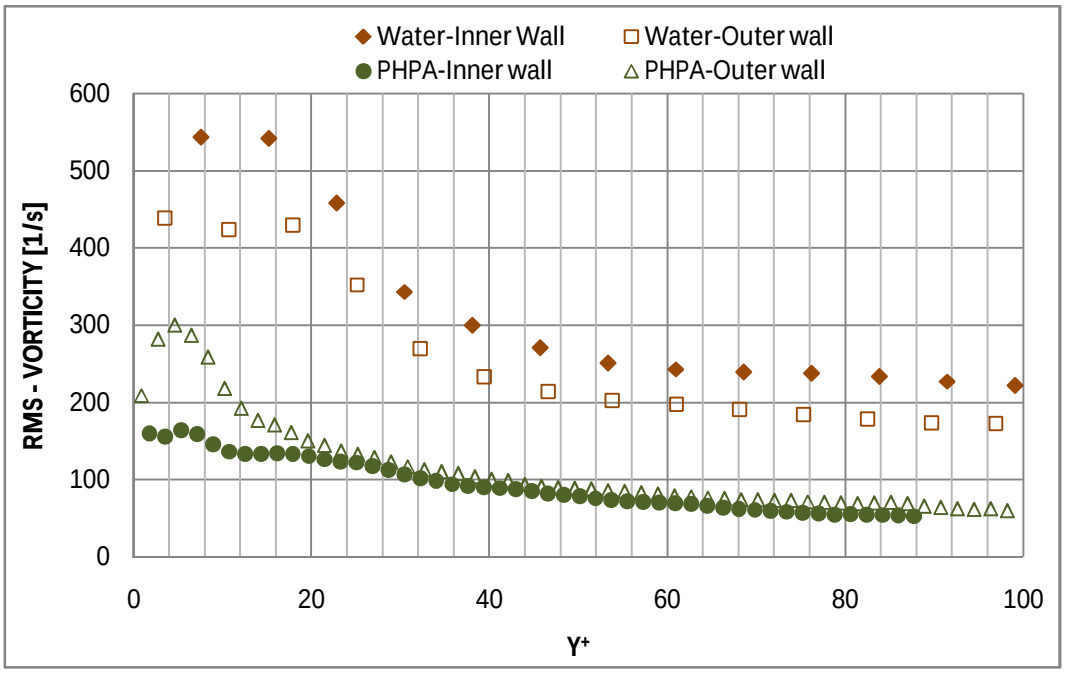

Figure 5 - 26. Results of the RMS of Vorticity for Water and Polymer Solution.

As explained by Paschkewitz et al [34], RMS of vorticity is related to the size and power of the near wall vortex structures. Thus, when the RMS of vorticity values are reduced, the sweep motions related to streamwise vortices decreases its effectiveness in creating

greater wall shear regions and therefore, drag reduction is obtained [34]. This supports the results obtained in figure 5-26, where much lower rms vorticity is obtained for the drag reduction fluid flow case.

Figure 5-26 also shows an interesting phenomenon. For the water flow case, it can be observed that the rms vorticity values are higher at the inner wall than at the outer wall. Therefore, higher wall shear stress is expected at the inner wall. However, after adding polymer to the flow, the RMS of vorticity is lower at the inner wall and consequently, lower wall shear stress is expected at the inner wall. These results can be validated by means of the wall shear stress calculated using the pressure drop. In the water flow case, the wall shear stresses obtained were 3.24 and 2.82 Pa at the inner and outer wall respectively. On the other hand, in the polymer fluid flow case, the wall shear stresses obtained were 2.04 and 2.6 Pa at the inner and outer wall respectively. This also supports the claim that more contribution to the overall drag reduction is provided by the inner wall.

5.3.4.3.6 Kinetic Energy Budget of Turbulent Flow

As suggested by Warholic et al. [14] and Ptasinsk et al. [15], when drag reducing additives are added to the flow, the turbulent flow should not be analyzed using the classical Newtonian fluid theory. The polymer molecules introduce a stress equal to the summation of the average polymer stress $\overline{\tau_p}$ and the fluctuating polymer stress τ'^{p}_{ij} [14]. It was also argued that the total shear stress is equal to the solvent stress plus the polymer stress [15]:

$$\tau_{xy} = \tau^{s}_{xy} + \tau^{p}_{xy} \qquad (14)$$

A scalar quantity $\varepsilon^p = \tau'^p_{xy}\gamma_{xy}$ was also defined by Warholic et al. [14] where γ_{xy} represents the fluctuation velocity gradient tensor. Thus, the turbulent energy equation (equation 13 – Chapter 4) for the polymer fluid flow becomes:

$$\frac{D}{DT}\left(\frac{1}{2}[u']^2\right) = -\frac{\partial}{\partial y}\left(\frac{1}{\rho}\overline{Pv'} + \frac{1}{2}\overline{[u']^2 v'} - 2\vartheta\overline{u' e_{xy}} - \frac{1}{\rho}\overline{u'\tau'^p_{xy}}\right) \qquad (15)$$

$$- \overline{u'v'}\frac{\partial u}{\partial y} - 2\vartheta\overline{e_{xy} e_{xy}} - \tau'^p_{xy}\gamma_{xy}$$

Two new terms were incorporated into the turbulent kinetic energy budget. The fourth term $(\frac{1}{\rho}\overline{u'\tau'^p_{xy}})$ on the right hand side of Eqn. 15 represents the transport by the polymer fibres and the seventh term $(\tau'^p_{xy}\gamma_{xy})$ represents the dissipation of energy by means of the polymer fibres.

The scope of this study is to analyze the impact of adding polymer to the flow on the shear production and the viscous dissipation of turbulent kinetic energy. Therefore, next we will analyze if there is a reduction or an increase in the energy produced and dissipated by the route of turbulence.

Figures 5-27 and 5-28 show the shear production (P_K) and viscous dissipation (V_D) terms, respectively. The results were normalized using the shear velocity and the kinematic viscosity.

The addition of polymer resulted in a strong decrease on both terms of the budget. However, the reduction in the shear production term is more noticeable. The significant reduction in the production term is mainly due to the strong decrease in the Reynolds stresses. Additionally, the heights of the peaks obtained for water are much higher than that of the polymer fluid flow. All the production peaks are located between 10 and 20 wall units. The peak heights for both polymer fluid and water flow are higher at the outer

wall than at the inner wall. These results are in agreement with numerical simulations results presented earlier [31, 35]. This suggests that, the zone where there is a major contribution from the polymers to the changes in turbulence is the buffer zone [31].

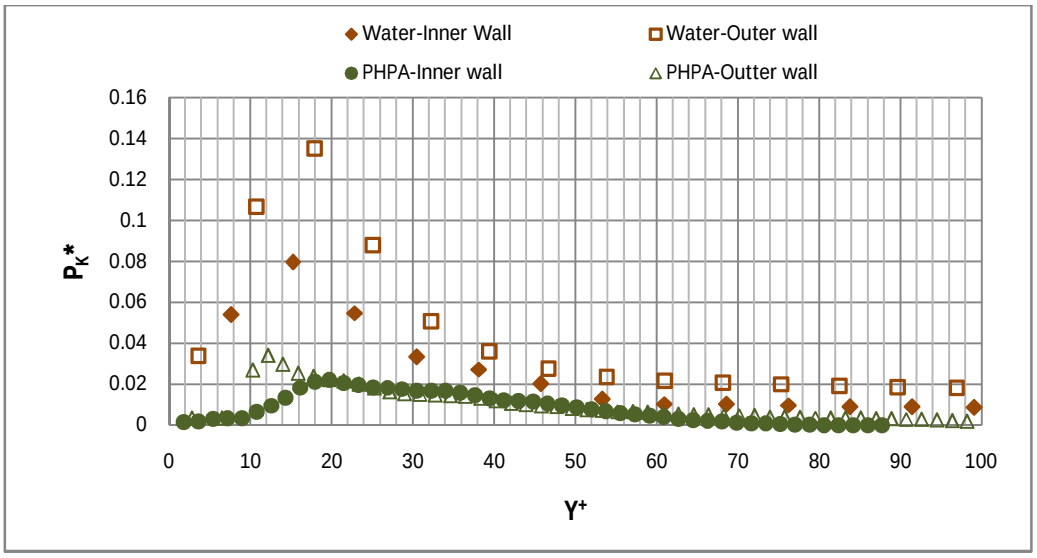

Figure 5 - 27. Normalized Shear Production of Turbulent Kinetic Energy for Flow of Water and Polymer Solution ($P_k^* = P_k * \vartheta / u_t^4$)

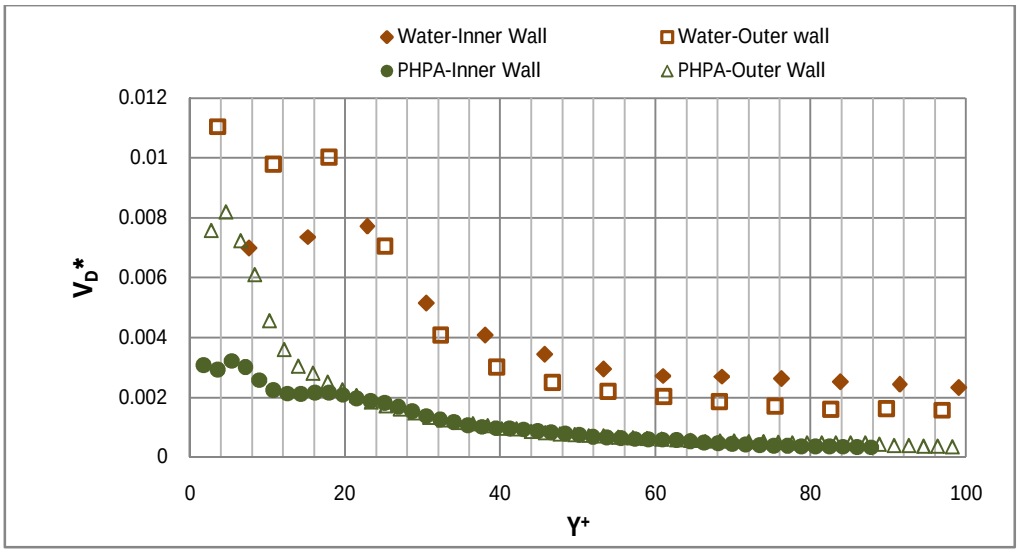

Figure 5 - 28. Normalized Viscous Dissipation of Turbulent Kinetic Energy for Flow of Water and Polymer Solution ($V_D^* = V_D * \vartheta / u_t^4$)

With reference to the viscous dissipation term (V_D), the main conclusion is that less energy is dissipated by the route of turbulence when adding polymer to the flow as shown in figure 5-28. Results obtained from numerical simulations, shows that the polymer stress work has a negative contribution to the turbulent kinetic energy budget and consequently, it acts as a dissipative term [31]. Therefore, a new route of energy dissipation in which a periodical coil polymer elongation and relaxation takes place exists as postulated by Sher et al., [12].

5.4 CONCLUSIONS

Turbulent drag reduction due to flow of polymer (PHPA) fluid flow in horizontal concentric annulus was investigated using the particle image velocimetry technique.

PHPA concentration was varied from 0.07% V/V to 0.12%V. Based on the pressure drop measurements and Reynolds stress analyses, the optimum polymer concentration was found to be 0.1%V/V.

The axial mean velocity profile was found to be following the universal law of the wall ($u^+=y^+$) in the viscous sub-layer ($y^+<10$) for both water and polymer fluid flow.

In the logarithmic zone, the velocity profile was found to be following the log wall ($u^+=2.5\ln(y^+)+5.5$) for the water flow. However, in the polymer flow case, although the velocity profile remained logarithmic, it has higher slope than that of velocity profile of water, showing the drag reduction effect due to polymer addition.

Comparison of the dimensionless velocity profile in the log-wall region near the inner and outer pipe walls shows that the velocity profile near the inner pipe wall has higher

slope than that of the one near the outer pipe wall. This suggests that more drag reduction is taking place close to the inner wall than the outer wall.

The thickness of the buffer zone for polymer fluid flow was much higher than that of observed in water flow.

The drag reduction is enhanced by the increasing Reynolds number. The maximum drag reduction (26%) was obtained at the highest solvent Reynolds number studied (Res=56400).

The effect of Reynolds number on the drag reduction was also proven by analyzing the velocity profile at different Reynolds numbers. The velocity profile in the logarithmic zone was shifted up (i.e., increasing slope) as the solvent Reynolds number was increased, indicating that the drag reduction was enhanced.

Reynolds stresses were found to be reduced in the core flow region by the increasing polymer concentration. However, in the region close to the wall ($y^+<10$), no more reduction in the Reynolds stress was observed when the polymer concentration exceeds the optimum value of concentration (0.1% V/V). This also explains, why above the optimum value of polymer concentration, more wall shear stress was present (since more viscosity is obtained at higher concentrations), and therefore no additional drag reduction was observed.

In the viscous sub-layer, the Reynolds stresses were reduced to a value close to zero. The peak values obtained for water flow are significantly higher than that of the polymer fluid flow. Comparing the peak locations, it can be seen that the peak locations are closer to the wall in the polymer fluid flow. Moreover, higher Reynolds stresses are encountered at the outer wall in both water and polymer fluid flow.

A significant decrease in the radial turbulent intensities was observed as a result of adding drag reducer to the flow, which makes the flow more rectilinear. A greater decrease in the turbulent radial intensities was obtained at the inner wall than at the outer wall.

The turbulent axial intensities were found to be almost the same in the region very close to the wall ($y^+<10$) for both water and polymer fluid flow. However, the axial rms velocity values obtained were higher for the polymer fluid flow between 10 and 60 wall units. Additionally, higher peaks values of axial intensities were obtained for the polymer fluid flow.

The fluctuating velocity fields demonstrate that the addition of polymer to the flow results in dampening of the small scale motions and radial fluctuations, which produces an important effect on the near wall activities producing turbulence. The sweeps and bursts seen for the polymer fluid flow were less chaotic and less frequent than that of the water flow. These reductions affect the Reynolds stress, which is decreased significantly.

Vorticity analyses show that the vorticity in water flow is very similar at both inner and outer walls. As polymer is added to the flow, the vorticity is reduced considerably. However, the vorticity reduction is higher at the inner wall. The vorticity is reduced almost to zero in both water and polymer fluid flow away from the wall.

Rms of vorticity values show that lower rms vorticity is obtained in the drag reduction fluid flow case than that of the water flow case showing the drag reduction effect. In the water flow case, the rms vorticity values are lower at the outer wall than at the inner wall. Therefore, lower wall shear stress is expected at the outer wall. However, after adding polymer to the flow, the RMS of vorticity is smaller at the inner wall and consequently, lower wall shear stress is expected at the inner wall. This also proved that more contribution to the overall drag reduction is supplied by the inner wall.

The viscous dissipation and the shear production terms of the kinetic energy budget show a significant decrease after adding polymer to the flow. However, the higher decrease was obtained in the production term due to the great reduction in the Reynolds stress.

The peak locations of the production term were found to be in the buffer zone, showing that the major changes in turbulence take place in the buffer zone. Moreover, both terms presented higher peak values at the outer wall, which demonstrates that more energy is produced and dissipated at the outer wall.

Finally, it can be concluded that less energy is dissipated by the route of turbulence when drag reduction additives are supplied to the flow.

5.5 References

[1] B. Toms., 1948, "Some observations on the flow of linear polymer solutions through straight tubes at large Reynolds numbers," *Proceedings of the First International Congress on Rheology* , 135–141.

[2] Hyoung, J.C., and Jhon, M.S.,1996, "Polymer-Induced Turbulent Drag Reduction," *Ind. Eng. Chem. Res*, 35, 2993-2998.

[3] Shah, S.N., Tareen, M., and Clark, D., 2000, "Effects of Solids Loading on Drag Reduction in Polymeric Drilling Fluids Through Straight and Coiled Tubings," *Petroleum Society's Canadian International Petroleum Conference 2000*, Calgary, Alberta, Canada.

[4] Ercan, C., and Ozbayoglu M.E., 2009, ""PHPA" as a Frictional Pressure Reducer and its Pressure Loss Estimation," *SPE/IADC middle east drilling theology conference & exhibition*, Manama, Bahrain.

[5] Lumley, J.L., 1969, "Drag reduction by additives," *Ann. Rev. Fluid Mech*, Vol. 1, 367-384.

[6] McCOMB, W.D., and CHAN, K.T.J., 1985, "Laser-Doppler anemometer measurements of turbulent structure in drag-reducing fibre suspensions," *J . Fluid Mech*, Vol .1 52, pp. 455-478.

[7] Kamel, A., and Shah, S.N., 2009, "Effects of salinity and temperature on drag reduction characteristics of polymers in straight circular pipes," *Journal of Petroleum Science and Engineering*, 67, 23–33.

[8] Shah, S.N., Kamel, A., and Zhou., 2006, "Drag reduction characteristics in straight and coiled tubing — An experimental study," *Journal of Petroleum Science and Engineering*, 53, 179–188.

[9] Dschagarowa, E., and Mennig ,G., 1976, *Fortschr.-Ber. VDI-Z*. Reihe 7/41.

[10] Dschagarowa, E., and Mennig ,G., 1977, "Influence of molecular weight and molecular conformation of polymers on turbulent drag reduction," *Rheol*, Acta 16, 309-316.

[11] Camail, M., Margaillan, A., Maesano, J.C., Thuret, S., and Vernet, J.L., 1998, "Synthesis and structural study of new copolymers, based on acrylamide and N-acryloyl acids, with persistent drag reduction activity," *Polymer , Vol. 39, No. 14, pp. 3187-3192.*

[12] Sher, I., and Hetsroni, G., 2008, "A mechanistic model of turbulent drag reduction by additives," *Chemical Engineering Science*, 63, 1771 – 1778.

[13] Japper-Jaafar, A., Escudier, M.P., and Poole, R.J., 2010, "Laminar, transitional and turbulent annular flow of drag-reducing polymer solutions," *J. Non-Newtonian Fluid Mech*, 165, pp. 1357–1372.

[14] Warholic, M.D., Heist, D.K., Katcher, M., and Hanratty, T.J., 2001, "A study with particle-image velocimetry of the influence of drag-reducing polymers on the structure of turbulence," *Experiments in Fluids*, 31, pp. 474-483.

[15] Ptasinski, P.K., Nieuwstadt, F.T.M., Van den brule, B.H.A.A., and Hulsen, M.A., 2001, “Experiments in Turbulent Pipe Flow with Polymer Additives at Maximum Drag Reduction,” J. *Flow, Turbulence and Combustion*, 66, pp. 159–182.

[16] M-I SWACO., 2007, “Poly-Plus Rd Polymer,” Product Bulletin.

[17] Wyatt, N.B., Gunther, C.M., and Liberatore, M.W., 2011,“Drag reduction effectiveness of dilute and entangled xanthan in turbulent pipe flow,” *J. Non-Newtonian Fluid Mech*, pp. 166, 25–31.

[18] Costello, B., 2005, “The AR-G2 Magnetic Bearing Rheometer,” TA Instruments Ltd.

[19] Shah , R.K., and London, A.I., 1978, “Laminar flow first convection in ducts,” Academic Press, New York.

[20] Escudier, M. P., Gouldson, I. W., and Jones D. M., 1995, “Flow of shear-thinning fluids in a concentric annulus,” Experiments in Fluids, 18, pp. 225–238.

[21] Jones, O. C., and Leung, J. C. M., 1981, “An Improvement in the Calculation of Turbulent Friction in Smooth Concentric Annuli,” J. Fluids Engineering, 103/615.

[22] Colebrook, C. R., 1939, "Turbulent flow in pipes with particular reference to the transition region between the smooth and rough pipe laws," J. Inst. Civ. Eng. (London), Vol. 11, pp. 133-156.

[23] F.M. White., 2005, “Viscous Fluid Flow,” The McGraw-Hill Companies.

[24] Nouri, J.M., Umur, H., Whitelaw, J.H., 1993, “Flow of Newtonian and non-Newtonian Fluids in concentric and eccentric annuli,” *J. Fluid Mech*., Vol.253., pp. 617-641.

[25] Lumley, J.L., 1973, “Drag Reduction in Turbulent Flow by Polymer Additives,” *J. Polymer Sci*., Macromolecular Reviews, Vol. 7, pp. 263-290.

[26] Virk, P.S., 1975, “Drag reduction fundamentals,” AIChE J. 21, 625–656.

[27] Rodriguez-Corredor, F.E., Bizhani, M., Kuru, E., and Ashrafuzzaman, M., 2012, "An experimental investigation of turbulent flow in concentric annulus using particle image velocimetry technique," *Proceedings of ASME 2012 International Mechanical Engineering Congress & Exposition*, Houston, Texas, US.

[28] Sureshkumar, R., Beris, A.N. and Handler, R.A., 1997, "Direct numerical simulation of the turbulent channel flow of a polymer solution," Phys. Fluids 9, pp. 743–755.

[29] Dimitropoulos, C.D., Sureshkumar, R. and Beris, A.N., 1998, "Direct numerical simulation of viscoelastic turbulent channel flow exhibiting drag reduction: Effect of variation of rheological parameters," J. Non-Newtonian Fluid Mech, 79, pp. 433–468.

[30] Hunt, J.C.R. and Durbin, P.A., 1999, "Perturbed vortical layers and shear sheltering," Fluid Dynam. Res. 24, pp. 375–404.

[31] Ptasinski, P.K., Boersma, B.J., Nieuwstadt, F.T.M., Hulsen, M.A., Van Den Brule, B.H.A.A., and Hunt, J.C.R., 2003, "Turbulent channel flow near maximum drag reduction: simulations, experiments and mechanisms," *J. Fluid Mech*, Vol. 490, pp. 251–291.

[32] Jaap M.J. den Toonder., 1996, "Drag Reduction by Polymer Additives in a Turbulent Pipe Flow: Laboratory and Numerical Experiments," *PhD Thesis*, Delft University of Technology.

[33] LaVision., 2006, "DaVis 7.2 Software," Product-Manual.

[34] Paschkewitz, J.S., Yves Dubief., Dimitropoulos, C.D., Shaqfeh, E.S.J., and Parviz Moin., 2004, "Numerical simulation of turbulent drag reduction using rigid fibres," *J. Fluid Mech*, Vol. 518, pp. 281–317.

[35] Chung, S.Y., Rhee, G.H., Sung, H.J., 2002, “Direct numerical simulation of turbulent concentric annular pipe flow Part 1: Flow field,” Int. J. Heat and Fluid Flow, 23, pp. 426-440.

6 A COMPARATIVE STUDY OF SOLIDS TRANSPORT PERFORMANCE - WATER VERSUS DRAG REDUCING FLUIDS.

6.1 Introduction

Choosing the most efficient fluid to be used during drilling operations is an important part of the drilling program. The fluid should not only yield the lowest pressure drops, but also be able to transport the solids effectively generated while drilling.

Insufficient cuttings transport can produce stuck pipe problems, early bit wear, slow drilling rate, high drag and torque, and fracture of the formation due to excessive annular pressure losses among other problems [1]. In vertical and near vertical wells cutting transport is usually not a problem [2]. However, these problems become more critical in horizontal and directional drilling [2,3]. Therefore, the understanding of solids transport is essential for the successful drilling of horizontal and extended reach wells.

Various flow patterns can be encountered during solids transportation depending on the fluid flow rate, geometry, fluid viscosity, and particle size and density [4-7]. Figure 6-1 shows the main flow patterns encountered in sand transport.

The first flow pattern is known as bed load. In this case, the flow velocity reach the critical velocity to initiate particle movement and the particles are moving in a thin layer along the bed of particles (rolling motion) [4]. Below the critical velocity, the particles are deposited at the bottom of the pipe forming a stationary bed [7].

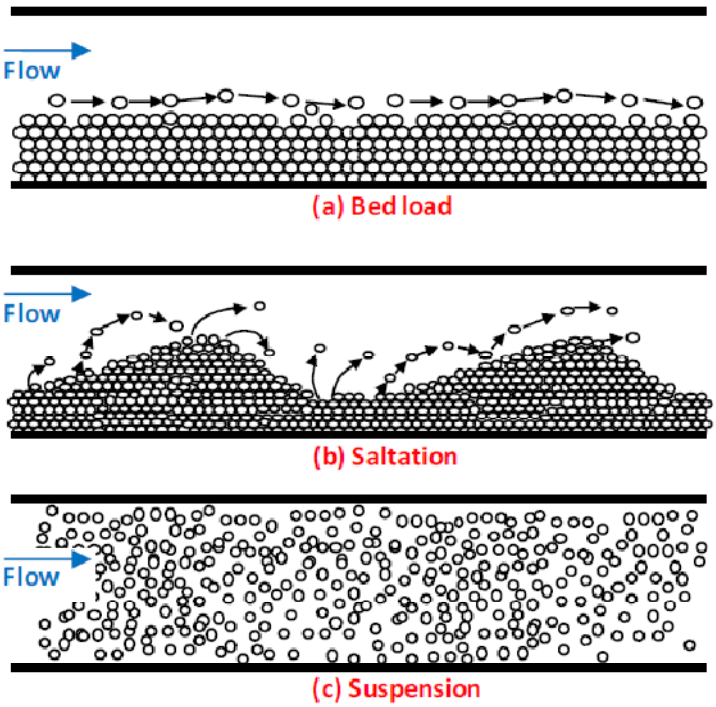

Figure 6 - 1. Different Flow Patterns Presented in Solids Transportation – Taken from Goharzadeh et al. [7].

The second flow pattern is known as saltation. At this conditions, the fluid flow velocity is higher than the critical velocity to initiate movement, but not sufficient to entrain the particles into suspension. However, the particles are transported by means of dunes where the particles are moving from downstream to upstream of the dunes [4]. The dunes velocity depends on the flow rates [8,9]. Pressure drop fluctuations are presented due to the dune movement and dune shape [8,9]. The significant pressure fluctuations are encountered at higher flow velocities, where the dune shape is more triangular [7,8].

Takahashi et al., [8-9] studied the pressure drop fluctuations while transporting particles in the saltation pattern. Figure 6-2 presents the schematic of the dunes formed. Equation 1 presents an expression, based on the Bernoulli's theorem, to calculate the maximum amplitude of the pressure fluctuation.

$$dP = \rho_w(v_1^2 - v_2^2) \quad (1)$$

Where V_1 and V_2 are the fluid velocity at the moving cross section 1 and 2 [8].

As seen from figure 6-2 and equation 1, when the dunes are more triangular, the difference between V_1 and V_2 become more significant and higher pressure fluctuations are expected [8].

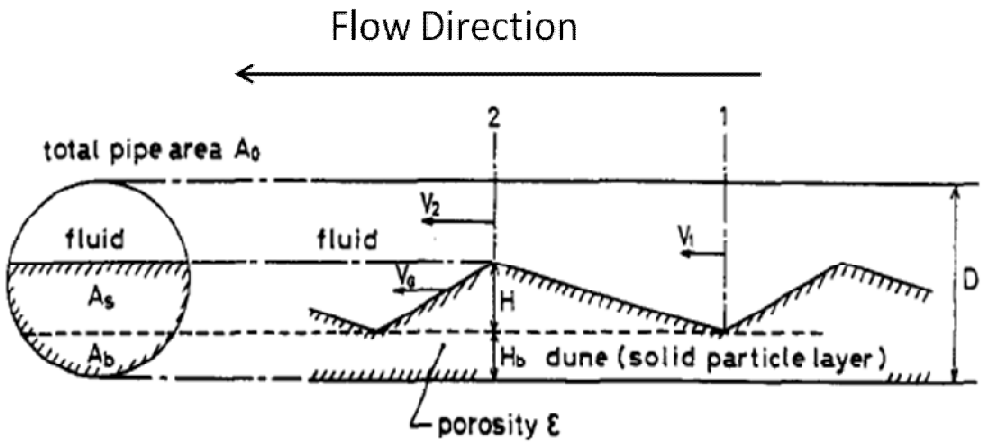

Figure 6 - 2. Dune Shape Formed During Sand Transportation - Taken from Takahashi et al. [8].

The third flow pattern is known as suspension. In this case, the fluid flow velocity is capable of entrain all the particles into suspension and a fully developed slurry mixture is obtained [7].

Different forces, depending on the particle diameter, are involved during the particle removal from the bed [10]. Summary of all the forces involved in solids transport are presented in Table 6-1. According to Phillips et al. [10] for the larger particle diameters (>200 microns) the net weight force and hydrodynamic drag force are more dominant (equation 2 and 3, respectively). In the smaller particle range (<30 microns) adhesion-cohesion force and updraft under a burst force are dominant (Equations 4 and 5,

respectively). Finally, updraft under a burst force and net weight force are the dominant forces in the intermediate particle diameter domain (equations 1 and 5, respectively) [10].

Table 6 - 1. Forces involved in the particle removal

Force	Formula	
Net Weight Force	$\frac{\pi}{6}\Delta\rho d_p^3$	(2)
Hydrodynamic Drag Force	$\frac{1}{8}C_D\rho_f v_f^2 \pi d_p^2$	(3)
Adhesion-Cohesion Force	$C_1 d_p$	(4)
Updraft Under A Burst Force	$C_2\rho_f v_f^2 \pi r_+^3$	(5)

C_1 is the adhesion coefficient, d_p the particle diameter, v_f is the fluid velocity, C_1 is the updraft under a burst parameter, C_D is the drag coefficient and r^+ the particle Reynolds number defines as [10]:

$$r^+ = \frac{u_\tau * d_p}{\vartheta} \quad (6)$$

Where u_τ is the friction velocity and ϑ is the kinematic viscosity.

Zeinali et al., [11] experimentally showed that the selective removal of particles from sand beds deposited in pipelines takes place depending on the particle diameter range. Using water as a fluid, it was observed that for a range of particles smaller than 60 microns, the larger particles were removed easily. However, the smaller particles were retained in the bed since the adhesion and cohesion forces are significantly high at this

particle diameter range as suggested by Phillips [10]. On the other hand, when the particle diameter was larger than 100 microns, the smaller particles were removed [11].

The drag reducing additives are commonly used in horizontal and extended reach drilling to minimize the frictional pressure losses and thereby increase the length of horizontal reach of the wells. Effect of drag reducing additives on the efficiency of the cutting transport process is of significant interest as one might not want to hamper cuttings transport ability of the fluid while reducing frictional pressure losses.

This chapter will present experimental results showing the effect of adding drag reducing additives on the solid transport performance of well fluids in concentric annuli. Particles with mean diameter ranges of 350 microns and 1.2 mm were used in solids transport experiments. The critical velocities to initiate particle movement in different modes were measured by using water and drag reducing fluid as carrier fluids. The flow patterns of solids with each fluid type and flow velocity conditions were observed. Pressure drop and dune velocities at different flow rates were also measured and analyzed.

6.2 Experimental Program

All the flow facilities, equipment associated and the film photography system used to measure the particle movement, were described in chapter 2.

6.2.1 Particle Properties

Natural sands having two different particles size ranges and the same physical properties were used. Table 6-2 shows the main physical properties of the particles used.

Table 6 - 2. Main Physical Properties of the Particles Used [12].

Mineral	**Quartz**
Specific gravity	2.65
pH	7.2-7.4
Bulk Density	92-95 Lbs/Ft^3
Shape	Sub-Angular

In order to guarantee that the particles used were uniform, particle size distributions analyses were performed. Table 6-3 and 6-4 show the results obtained after performing sieving analysis to the finer and coarser particles respectively.

Table 6 - 3. Particle Size Distribution of the Fine Particles.

Mesh Number	**Dp [microns] Associated to the Mesh Number**	**Weight [g] Retained on the Mesh**	**Normalized weight [g] Retained on the Mesh**
20	850	0	0
30	600	0	0
35	500	0	0
40	425	8.863	9.104356
45	355	43.515	44.7
50	300	31.14	31.988
60	250	8.168	8.39043
80	180	5.078	5.216284
100	150	0.275	0.282489
120	125	0.31	0.318442
Total		97.349	100

Table 6 - 4. Particle Size Distribution of the Coarse Particles

Mesh Number	Dp [microns] Associated to the Mesh Number	Weight [g] Retained on the Mesh	Normalized weight [g] Retained on the Mesh
10	2000	0	0
12	1700	0	0
16	1180	58.8	59.2324
20	850	36.47	36.73819
25	710	2.6	2.61912
30	600	1.4	1.410295
		99.27	100

Figures 6-3 and 6-4 show the particle size distribution analyses in terms of the percent of particles smaller than a determined particle diameter d_p ($\%P_f$) for the finer and coarser particles respectively.

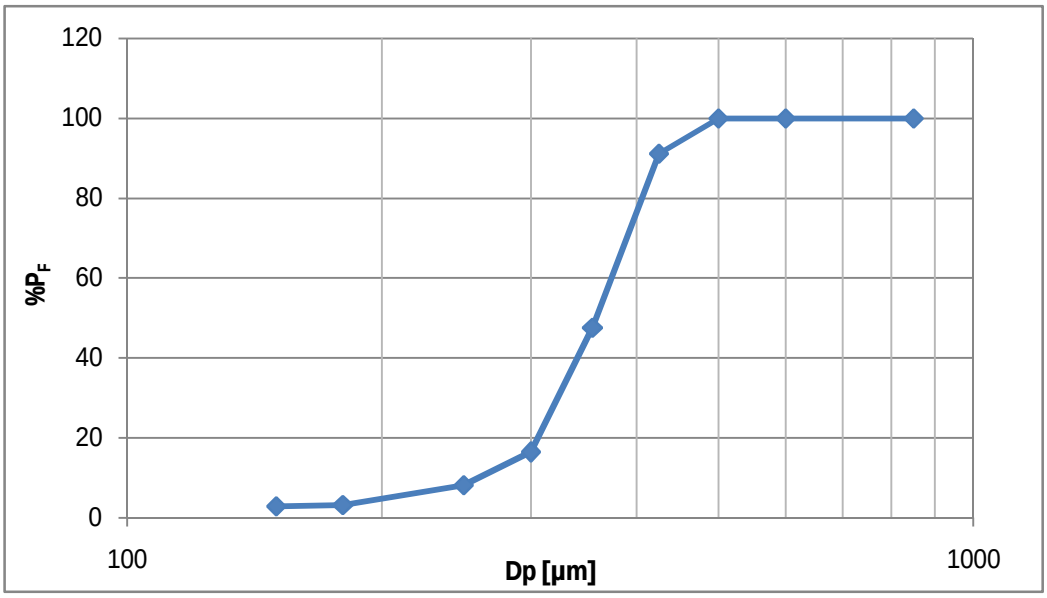

Figure 6 - 3. Particle Size Distribution for the Finer Particles Used.

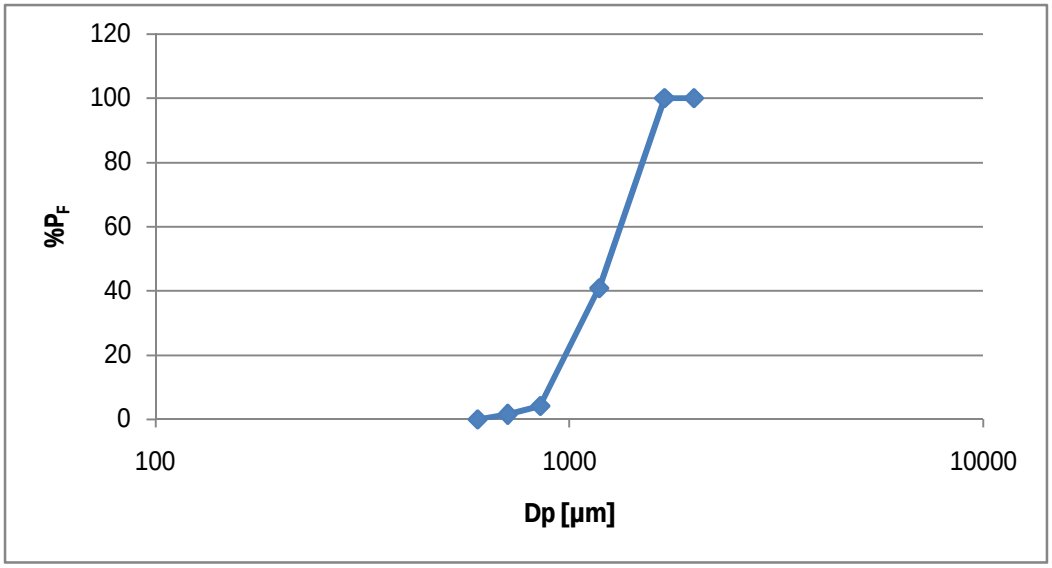

Figure 6 - 4. Particle Size Distribution for the Coarser Particles Used.

In order to determine numerically if the particles used are uniform, the standard deviation and geometric standard deviation should be calculated using the following relationships [13]:

$$\Phi = -log_2(d_p) = -\frac{\ln(d_p)}{\ln(2)} \tag{6}$$

$$\Phi_m = \int \Phi\, P(\Phi) d\Phi \tag{7}$$

$$\delta^2 = \int (\Phi - \Phi_m)^2\, P(\Phi)\, d\Phi \tag{8}$$

$$\delta_g = 2^{\delta} \tag{9}$$

Where Φ_m is the mean particle diameter, δ is the standard deviation and δ_g is the geometric standard deviation.

Table 6-5 shows the results obtained for the two different particles size ranges. The particle distribution is considered uniform when the geometric standard deviation is less

than 1.3 [12]. It can be seen that in both cases the geometric standard deviation is less than 1.3. Therefore, the particle size distribution of the two types of particles used in this study can be considered as uniform and the mean particle diameter will have the same value of d_{50} (median particle diameter).

Table 6 - 5. Results of Statistics Analyses of Fine and Coarse Particles

Property	**Finer Particles**	**Coarser particles**
Mean Diameter [µm]	350	1214.
Standard Deviation	0.27	0.28
Geometric Standard Deviation	1.21	1.21

6.2.2 Establishment of the Bed of Particles

Figure 6-5 shows the schematic of the horizontal flow facility used for cuttings transport experiments. The mixing tank was filled up with water at room temperature. Then, the water was re-circulated through the loop and the flow velocity was gradually increased until achieving around 1.5 m/s. After that, the particles were slowly added to the tank until the particles concentration reached up to 3%. In order to guarantee a homogenous solution, the mixer was operated at the highest rpm while adding the particles to the tank. After adding the desired amount of particles, the mix was allowed to re-circulate through the loop for about 20 minutes. Finally, the pump was stopped and the horizontal annular section was isolated by closing the valves 5 and 6 shown in figure 6-3. The mix was allowed to rest for 24 for hours. Consequently, the particles were deposited at the bottom of the pipe forming a stationary bed.

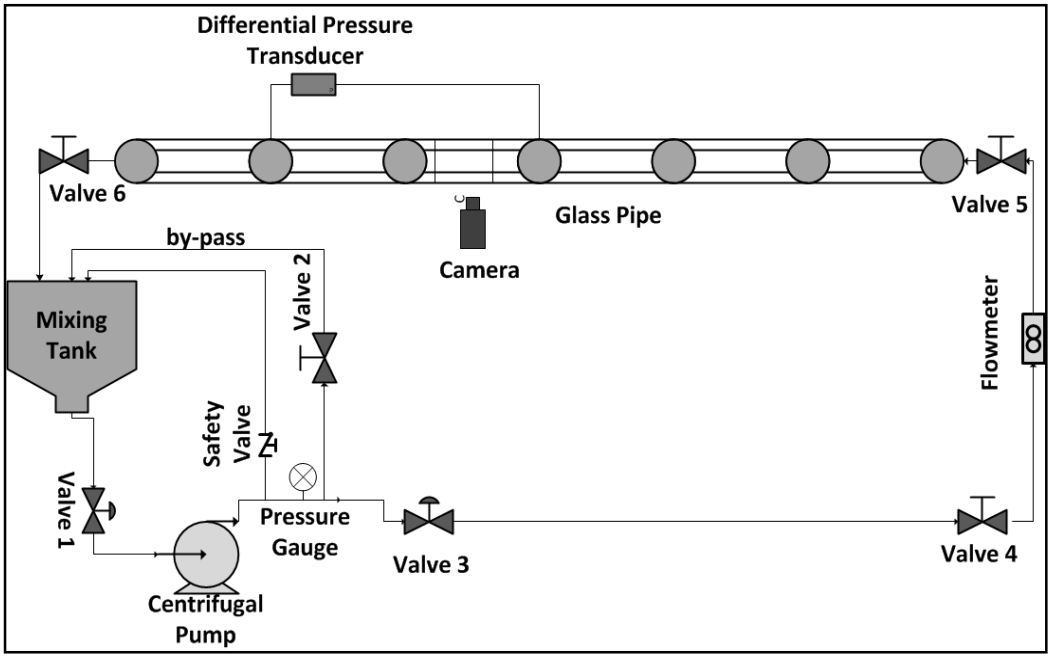

Figure 6 - 5. Schematic of the Experimental Setup

6.2.3 Polymer Fluid Preparation

A high molecular weight partially hydrolyzed polyacrylamide (PHPA) provided by M-I SWACO Canada was used as drag reducer agent. The main PHPA properties are presented in the Table 5-1 in chapter 5.

The polymer solution was prepared by using the procedure recommended by Wyatt et al. [14]. Initially, a concentrated solution was prepared by adding polymer slowly to the mixing tank filled up with water at room temperature. The mixer was operated at 30 RPM to avoid degradation of the polymer fibres. The solution was allowed to rest for 24 hours and after that, it was diluted to desired final concentration. In order to guarantee that the solution was properly mixed, it was allowed to re-circulate for 10 minutes through the by-pass installed between the discharge of the pump and the tank (see figure 6-5). It should be mentioned that by that time, the valve #3 was closed.

6.2.4 Polymer Fluid Characterization

The rheological measurements were performed using a high resolution modular rheometer Bohlin C-VOR 150. The rheometer is equipped with a dynamic spectrometer system which has a triple-mode motor control [15]. This configuration allows performing shear stress or shear rate controlled measurements [15]. For this research, rheological measurements were conducted at controlled shear stress mode.

6.2.5 Experimental Procedure

Once the bed of particles was established, the horizontal annular section was opened (valves 5 and 6 were opened). Immediately, the fluid stored in the mixing tank (either water or polymer fluid) was sent through the loop at a very low velocity (i.e., velocity below the critical velocity to initiate any particle movement). After the water that was used initially to establish the solid bed in the horizontal annular section was removed, the flow rate of the carrier fluid was gradually increased and the particle movement at each velocity was recorded by using the film photography system described in chapter 2. Two filters were installed at the outlet of the loop to impede removed particles getting back into the annular section. All the flow variables such as pressure drop and flow rate were recorded.

6.3 Results and Discussion

6.3.1 Polymer Fluid Rheology

Figures 6-6 and 6-7 show the shear stress vs. shear rate curve for the fluids with polymer concentrations of 0.07%V/V and 0.1%V/V, respectively. Three sets of rheology results are reported for each polymer concentration; polymer (PHPA) only, polymer fluid used

for small particle (d_{50}=350 micron) transport and polymer fluid used for large particle (d_{50}=1.12 mm) transport. Polymer fluid samples were collected from test section (i.e. annular section) using special sample collector while the polymer fluid was being circulated through the loop with and without the presence of solids. Fluid rheology follows the power law model in all cases. The power law parameters obtained at each case, are shown in table 6-6. Although the polymer concentration (0.07%) and mixing procedure are the same for all the samples, the rheology results (i.e.; k and n values) presented in Figure 6-6 show a slight difference. Similar variations in k and n values are also observed for the samples whose shear stress vs. shear rate behaviours are shown in Figure 6-7 (polymer concentration 0.1%)

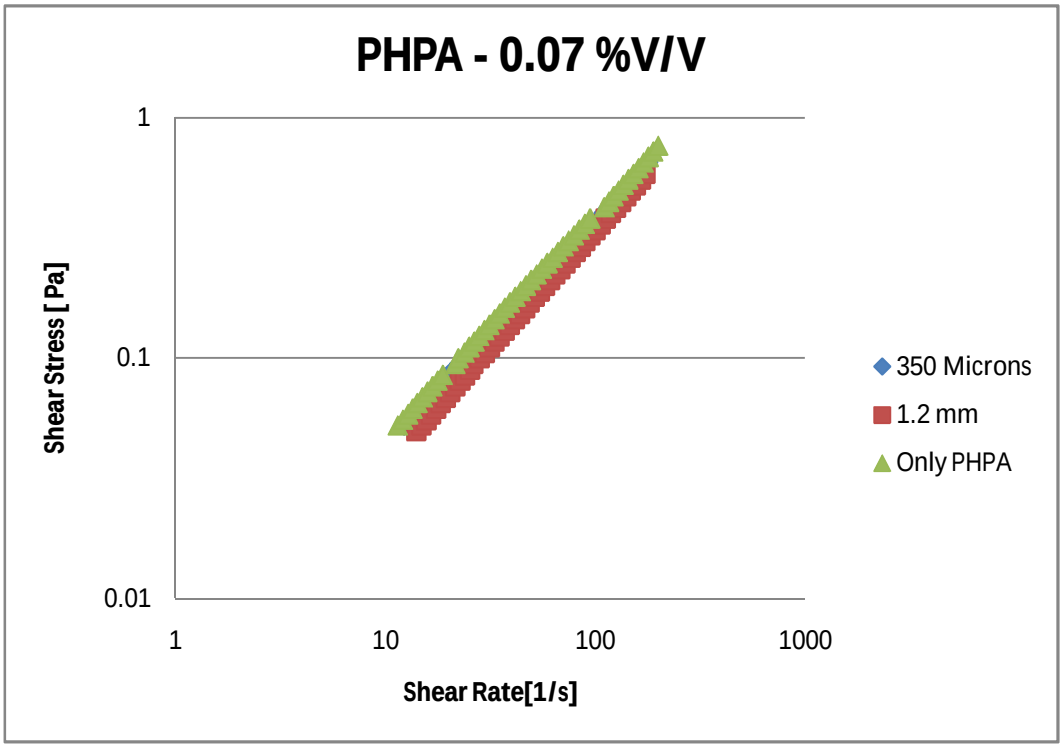

Figure 6 - 6. Shear Stress Versus Shear Rate for 0.07 %V/V Polymer Solutions.

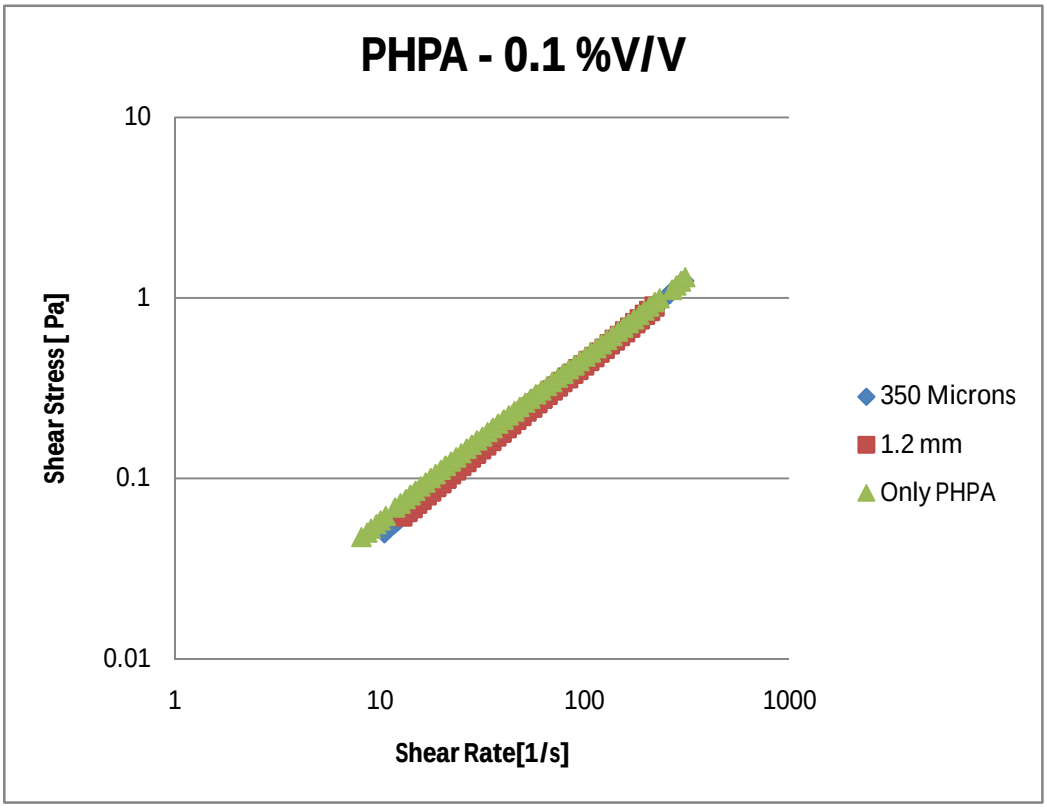

Figure 6 - 7. Shear Stress Versus Shear Rate for 0.1 %V/V Polymer Solutions.

Table 6 - 6. Power Law Parameters of Polymer Fluids

PHPA Concentration [%V/V]	Particle Diameter [mm]	k	n
0.07	0.35	0.005	0.927
0.07	1.2	0.003	0.973
0.07	Only PHPA	0.005	0.926
0.1	0.35	0.005	0.94
0.1	1.2	0.005	0.936
0.1	Only PHPA	0.007	0.897

Figure 6-8 and 6-9 present the viscosity versus shear rate curve for both polymer fluids.

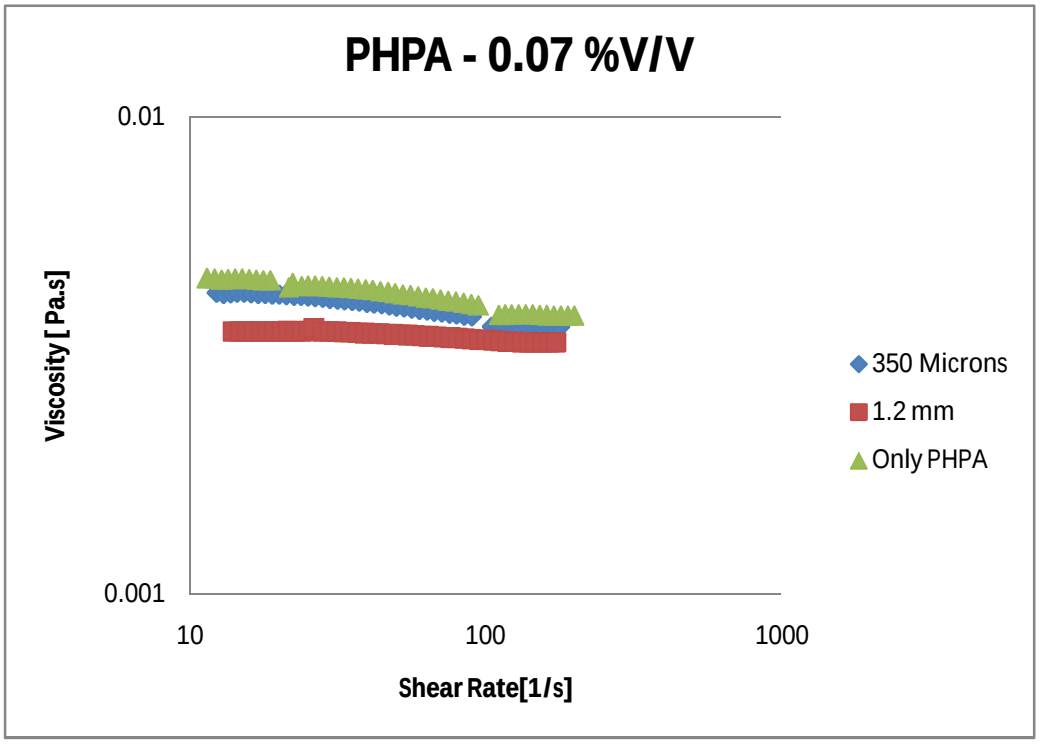

Figure 6 - 8. Viscosity Versus Shear Rate for 0.07 %V/V Polymer Solutions.

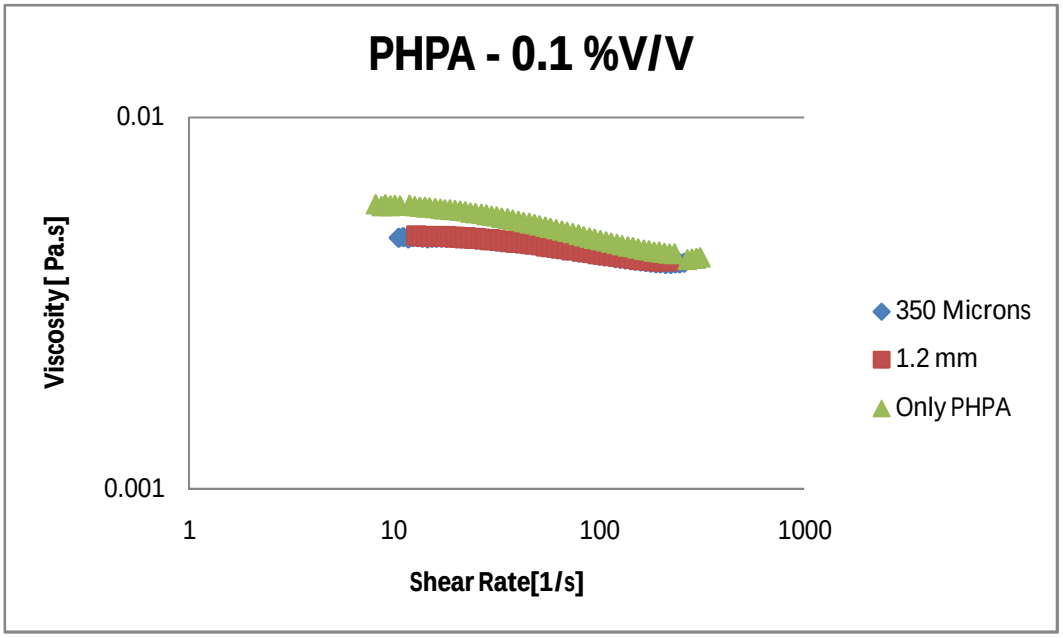

Figure 6 - 9. Viscosity Versus Shear Rate for 0.1 %V/V Polymer Solutions.

For both particle size ranges, the viscosity was found to be lower when the polymer fluid sample was collected from test section while the fluid was being circulated over the bed of particles as compared to the case when the polymer fluid sample was collected while the polymer fluid was being circulated through the loop without the presence of solids. For the 0.1%V/V polymer concentration, no significant changes in fluid viscosity were observed from the samples collected while circulating over the bed of both particle size ranges. However, for the 0.07%V/V polymer concentration, the lowest viscosity was obtained from the fluid sample collected while circulating over the coarser particle size range. The viscosity of the fluid sample (0.07%V/V polymer concentration) collected while circulating over the finer particles was close to the viscosity of the fluid circulated without the presence of bed of particles.

6.3.2 Critical Velocity to Initiate Movement of Small Size Range Particles in Various Flow Patterns with Water

Table 6-7 shows the different flow patterns obtained in the solid transport experiments using water and particles with mean diameter of 350 microns. A picture of the continuous bed formed initially is shown in figure 6-10. It was observed that the particles started rolling at a velocity of 0.24 m/s. At a velocity equal to 0.26 m/s, dunes with saltation pattern were observed. Figures 6-11 to 6-14 show how the dunes developed as the bulk fluid velocity changed from 0.26 m/s to 0.33 m/s. An increase in the bulk fluid velocity caused the dunes length to decrease and dunes get more separated from each other as shown in figures 6-15 and 6-16. When the bulk fluid velocity was close to critical value for particle suspension, the dunes started breaking down and a continuous moving bed is obtained as shown in figures 6-17 and 18. The suspension of the particles started taking place at a velocity of 0.54 m/s.

Table 6 - 7. Flow Patterns Versus Bulk Fluid Velocity: Water – d_{50}: 350 Microns.

Water - 350 microns	
Velocity[m/s]	Bed Type
0.10	Stationary Bed
0.19	Stationary Bed
0.24	Critical Velocity - Rolling
0.26	Dunes/Saltation
0.28	Dunes/Saltation
0.33	Dunes/Saltation
0.37	Dunes/Saltation
0.41	Dunes/Saltation
0.45	Dunes/Saltation
0.50	Dunes/Saltation
0.54	Critical Velocity/ Suspension
0.58	Suspension

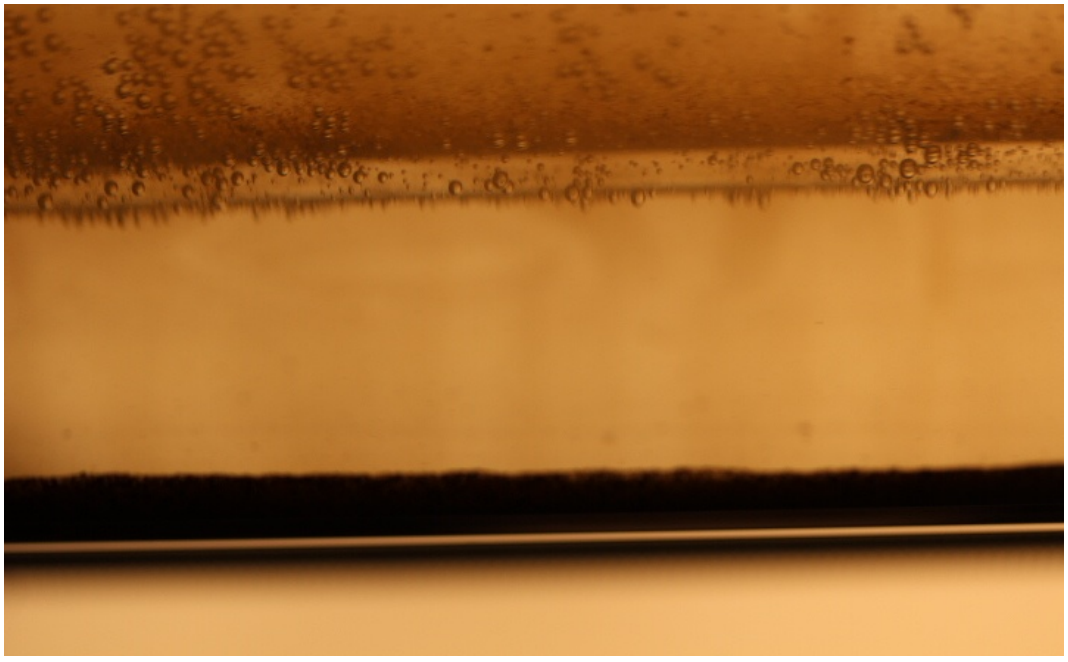

Figure 6 - 10. Stationary Bed of Particles - Mean Particle Diameter: 350 Microns.

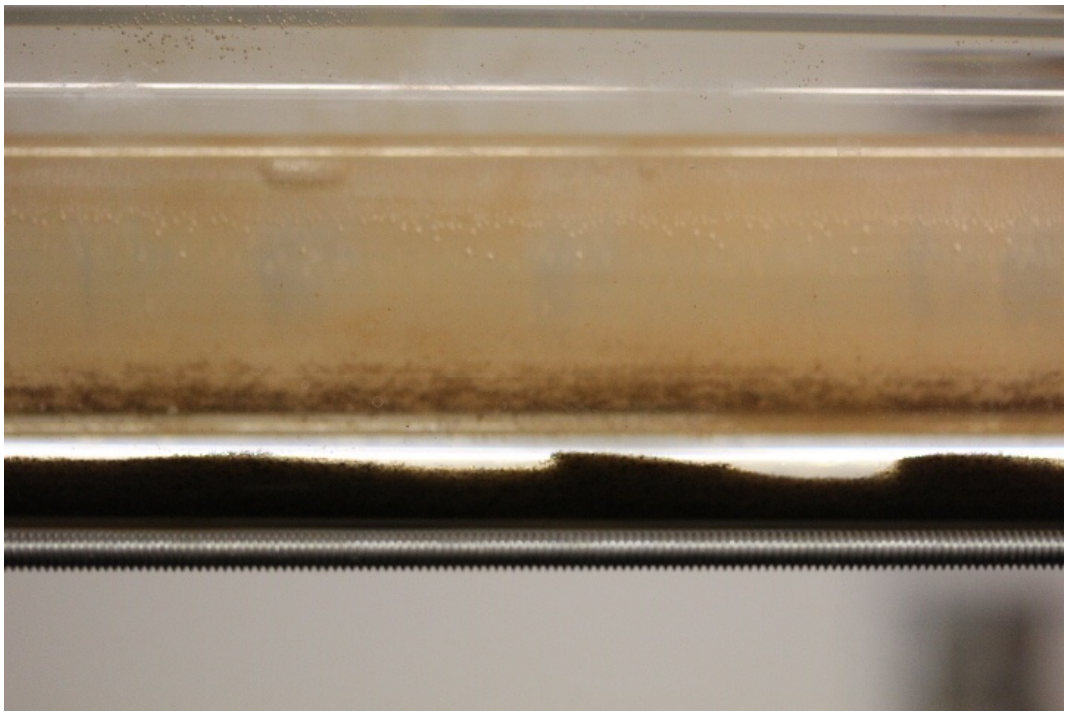

Figure 6 - 11. Dunes/Saltation Pattern Starts Forming at Velocity of 0.26 m/s - Water Flow - Mean Particle Diameter: 350 Microns - View from the Side of the Pipe.

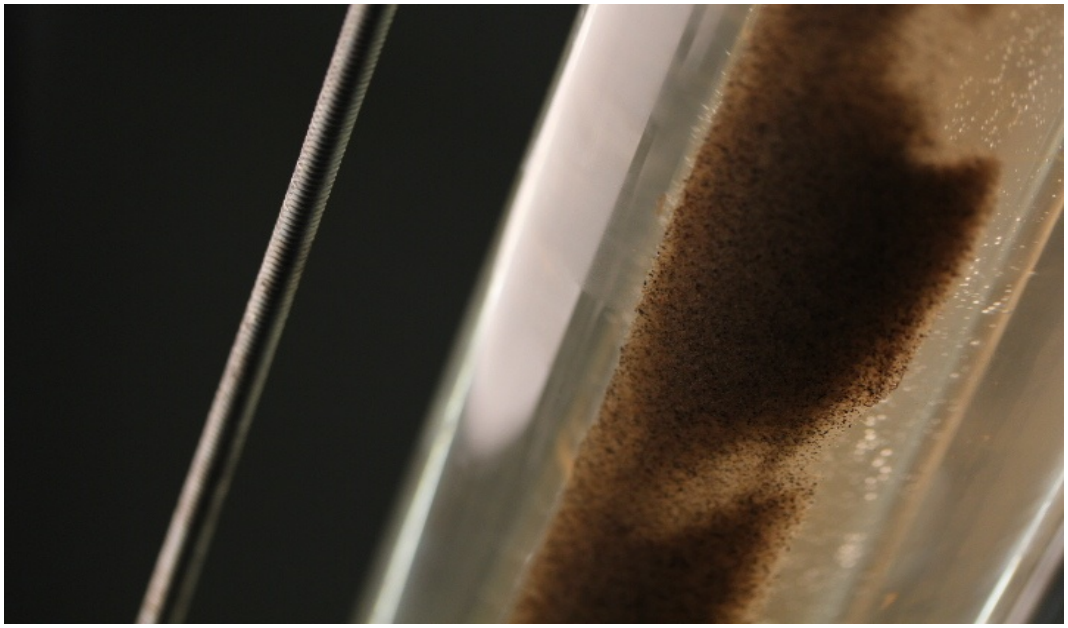

Figure 6 - 12. Dunes/Saltation Pattern Starts Forming at Velocity of 0.26 m/s - Water Flow– Mean Particle Diameter: 350 Microns - View from the Bottom of the Pipe.

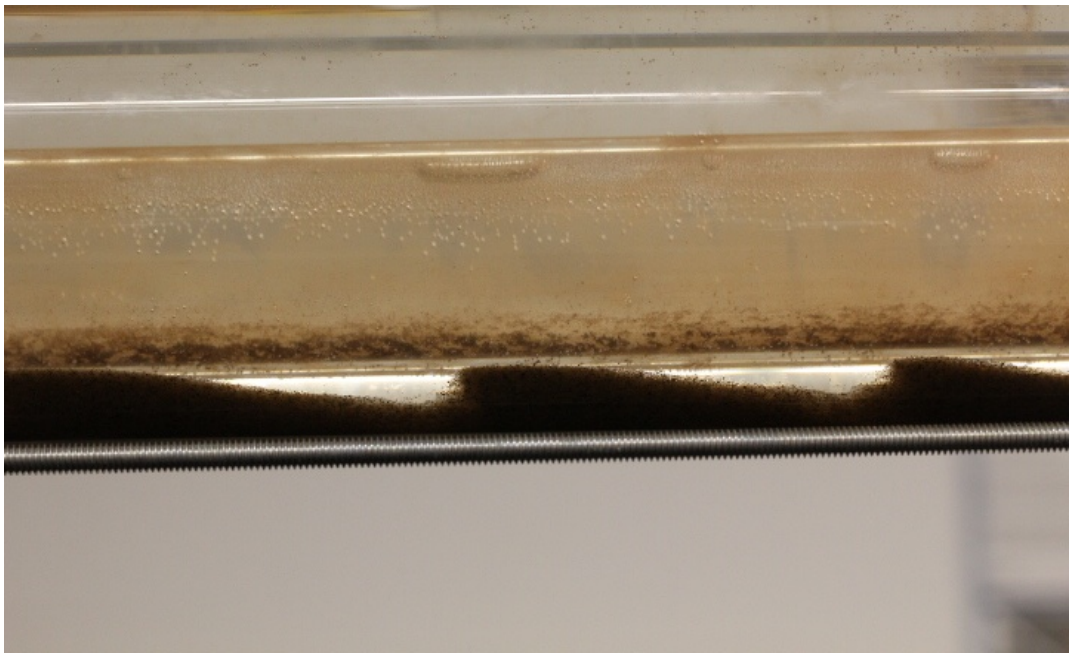

Figure 6 - 13. Dunes/Saltation Pattern at Velocity of 0.28 m/s - Water Flow - Mean Particle Diameter Equal to 350 Microns - View from the Side of the Pipe.

Figure 6 - 14. Dunes/Saltation Pattern at Velocity of 0.28 m/s - Water Flow - Mean Particle Diameter: 350 Microns - View from the Bottom of the Pipe.

Figure 6 - 15. Dunes/Saltation Pattern at Velocity of 0.33 m/s - Water Flow - Mean Particle Diameter: 350 Microns - View from the Bottom of the Pipe.

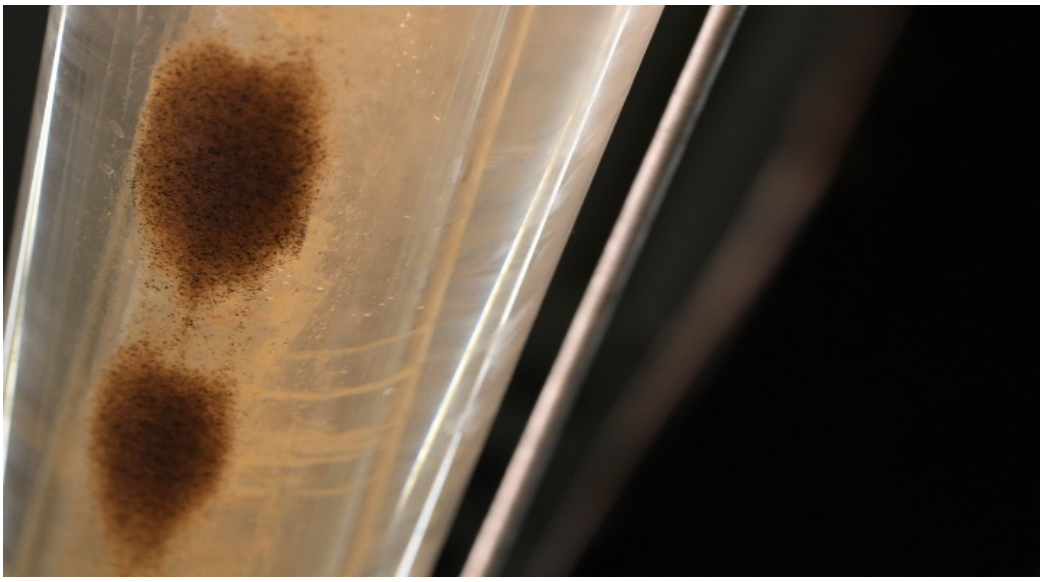

Figure 6 - 16. Dunes Pattern Formed at Velocity of 0.45 m/s - Water Flow -View from the Bottom of the Pipe - Mean Particle Diameter: 350 Microns.

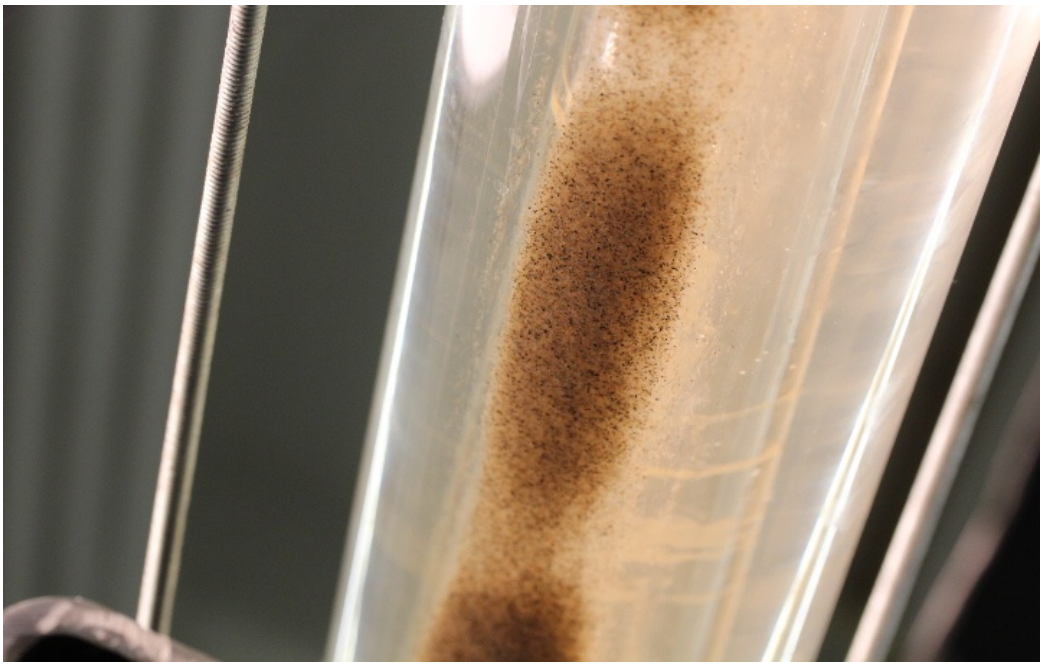

Figure 6 - 17. Transition from Dunes to Continuous Moving Bed/Heterogeneous Suspension Pattern Forming at Velocity of 0.5 m/s for -Water Flow - View from the Bottom of the Pipe - Mean Particle Diameter : 350 Microns.

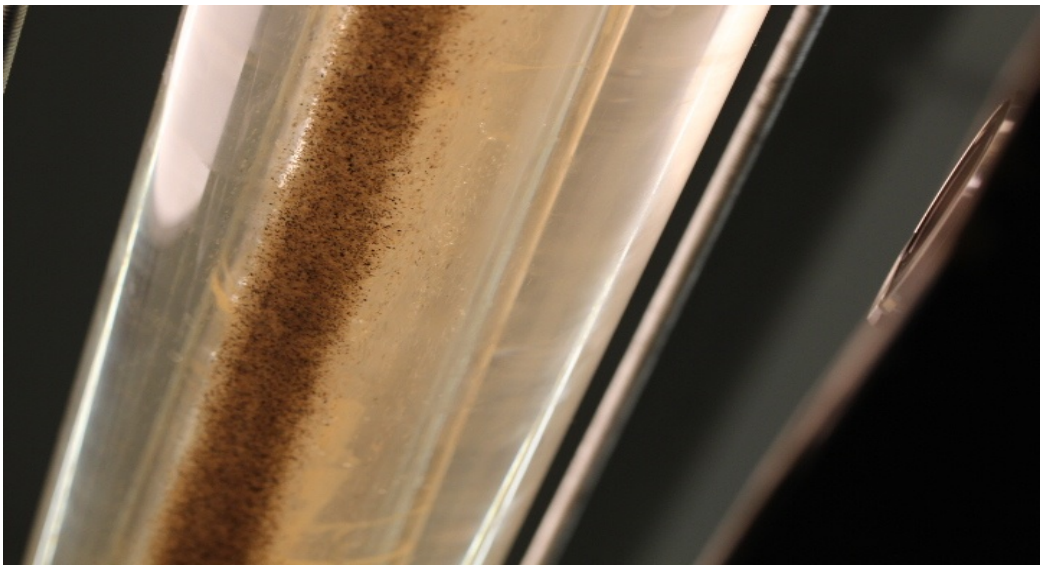

Figure 6 - 18. Heterogeneous Suspension Pattern at Velocity of 0.54 m/s - Water Flow - View from the Bottom of the Pipe - Mean Particle Diameter: 350 Microns.

6.3.3 Critical Velocity to Initiate Movement of Small Size Range Particles in Various Flow Patterns with Drag Reducing Fluid

Examples of the flow patterns obtained when transporting particles by using a carrier fluid with polymer concentration of 0.07%V/V are presented in figures 6-19 to 6-23

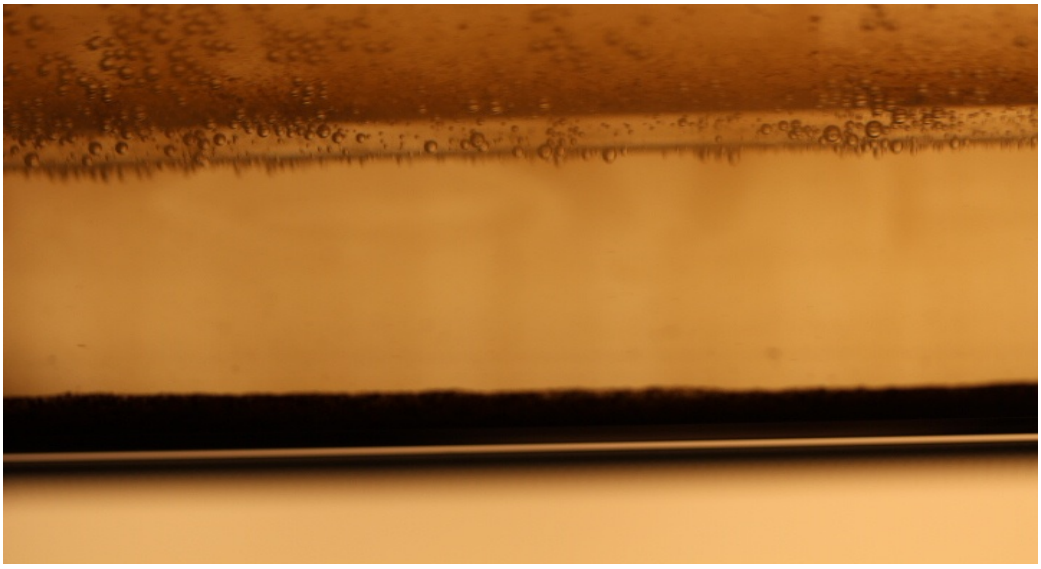

Figure 6 - 19. Stationary Bed of Particles - 0.07%V/V PHPA Solution - Mean Particle Diameter: 350 Microns.

Figure 6 - 20. Dunes/Saltation Pattern at Velocity of 0.96 m/s - 0.07%V/V PHPA Solution - View from the Side of the Pipe - Mean Particle Diameter: 350 Microns.

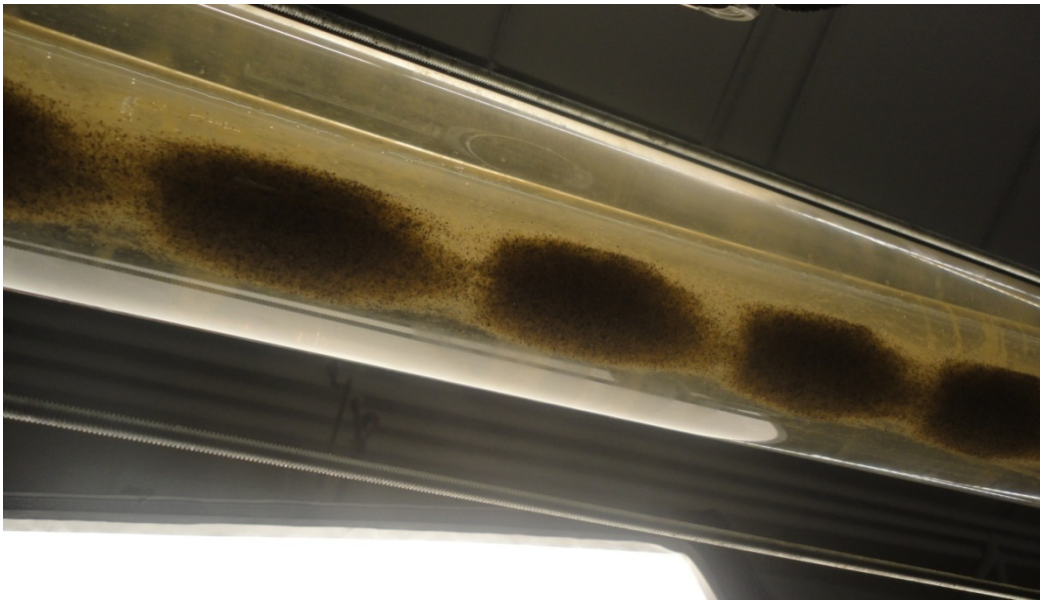

Figure 6 - 21. Dunes/Saltation Pattern at Velocity of 0.96 m/s - 0.07%V/V PHPA Solution - View from the Bottom of the Pipe - Mean Particle: 350Microns.

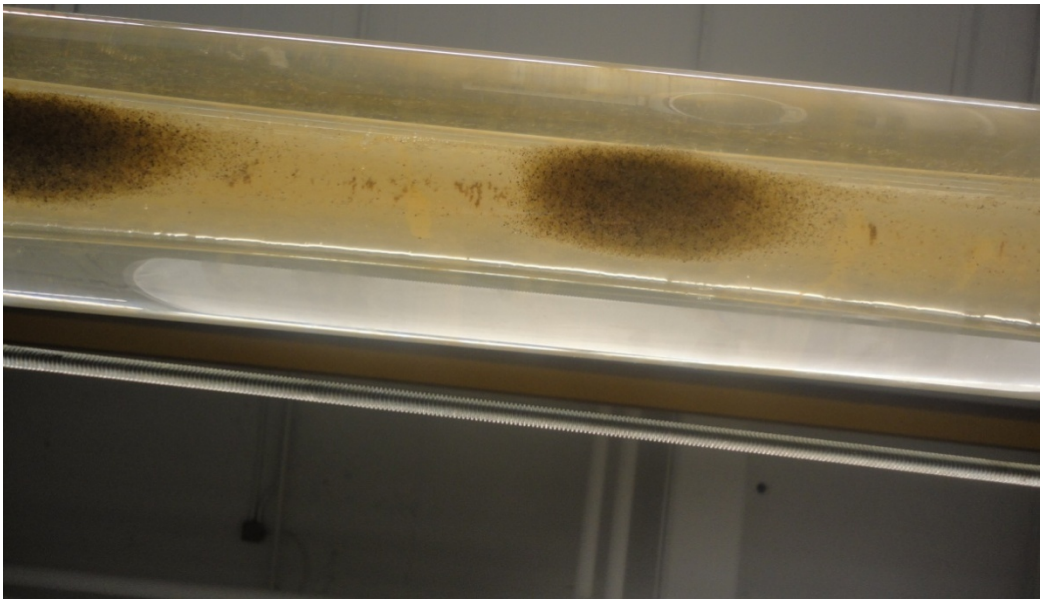

Figure 6 - 22. Dunes/Saltation Pattern at Velocity of 0.99 m/s - 0.07%V/V PHPA Solution - View from the Bottom of the Pipe – Mean Particle Diameter: 350 Microns.

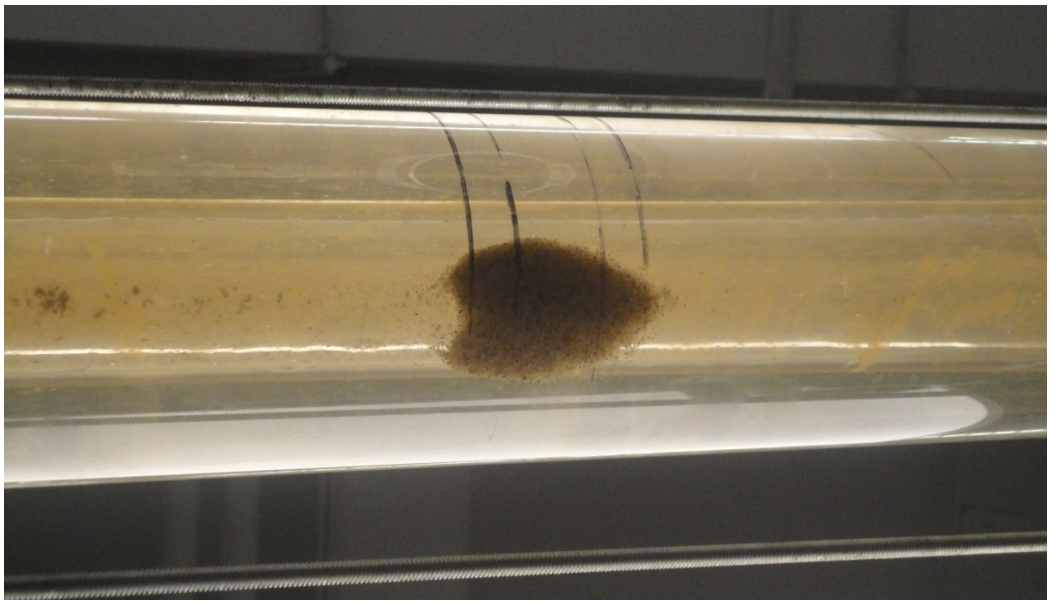

Figure 6 - 23. Dunes/Saltation Pattern at Velocity of 1.12 m/s - 0.07%V/V PHPA Solution - View from the Bottom of the Pipe - Mean Particle Diameter: 350 Microns.

It can be seen that at the low bulk fluid velocities (figures 6-20 and 6-21); the dunes are bigger and almost attached to each other. However, as the bulk fluid velocity increases, the dunes get smaller and start to get separated from each other as shown in figures 6-22 and 6-23. Comparing the particle transport with polymer fluid to that of the with water flow, it can be seen that dunes are smaller and more separated in the polymer fluid case. This is attributed to the bulk fluid velocity (as explained by Takahashi et al [8]) creating particle movement in saltation/dunes mode, which is higher in the polymer fluid flow than that of the case in water flow.

Table 6-8 and 6-9 present the summary of flow patterns observed when transporting particles with mean diameter of 350 microns by using drag reducing fluids. Table 6-8 shows the results obtained by using a carrier fluid with a polymer concentration of 0.07% V/V. Table 6-9 shows the results obtained by using a carrier fluid with a polymer concentration of 0.1%V/V.

Table 6 - 8. Flow Patterns Observed with 0.07% V/V PHPA Fluid – d_{50}: 350 Microns.

PHPA 0.07% V/V - 350 microns	
Velocity[m/s]	Bed Type
0.68	Stationary Bed
0.74	Stationary Bed
0.80	Stationary Bed
0.86	Stationary Bed
0.89	Critical Velocity - Rolling
0.91	Rolling
0.96	Dunes/Saltation
1.02	Dunes/Saltation
1.07	Dunes/Saltation
1.11	Dunes/Saltation
1.14	Dunes/Saltation
1.19	Dunes/Saltation
1.24	Dunes/Saltation

Table 6 - 9. Flow Patterns Observed - 0.1% V/V PHPA Fluid – d_{50}: 350 Microns.

PHPA 0.1% V/V - 350 microns	
Velocity[m/s]	Bed Type
0.66	Stationary Bed
0.71	Stationary Bed
0.76	Stationary Bed
0.82	Stationary Bed
0.88	Stationary Bed
0.91	Stationary Bed
0.94	Critical Velocity - Rolling
0.97	Rolling
0.99	Dunes/Saltation
1.04	Dunes/Saltation
1.07	Dunes/Saltation
1.12	Dunes/Saltation
1.15	Dunes/Saltation

The critical velocity to initiate particle movement in rolling was 0.89 m/s and 0.94 m/s for the fluids with 0.07% and 0.1% polymer concentrations, respectively. Dunes/saltation patterns were observed at bulk fluid velocities 0.96 m/s and 0.99 m/ when transporting particles with polymer fluids of 0.07% and 0.1% polymer concentrations, respectively. Suspension flow pattern was not observed in either fluid case within the range of experimental conditions (i.e., maximum fluid velocity achieved was 1.24 m/s and 1.15 m/s when pumping fluids of 0.07% and 0.1% polymer concentrations, respectively). As

the polymer concentration of the carrier fluid increased, higher critical velocity was required for the initiation of particle movements in all observed flow patterns. As compared to particle transport with water, significantly higher critical velocities were required when transporting particles by drag reducing fluids.

The following discussion is offered to explain the difference between critical velocity of solids transport when using water and a drag reducing fluid. Equation 10 can be used for calculating the viscous sub-layer thickness [16].

$$\delta_v = \frac{5 * \vartheta}{u_\tau} \tag{10}$$

Where;

δ_v=Boundary layer thickness

ϑ =Kinematic viscosity

u_τ=Friction velocity

As shown in figures 6-8 and 6-9, the viscosity of the drag reducing fluid is considerably higher than that of the water. In chapter 5, it was also reported that a significant decrease in the friction velocity (u_τ) was observed in the polymer fluid flow. Therefore, the boundary layer thickness is considerably higher in the polymer fluid cases. Taking into account the characteristics of the universal velocity profiles explained in chapters 4 and 5, the local velocities are significantly low in the viscous sub-layer. Therefore, if the particles are in the viscous sub-layer, they are exposed to very low local velocities and they may not be sufficient to commence particle movement. Therefore, the viscous sub-layer thickness should be reduced to the same order of magnitude of the particle diameter

(or less) in order to expose the particles to higher local velocities which would be sufficiently strong to commence particle movement.

This reduction in the viscous sub-layer thickness can be achieved by increasing the friction velocity (see equation 10) which is a function of the wall shear stress as explained in chapter 4 and 5. The wall shear stress is a direct function of flow velocity, so the viscous sub-layer thickness can be reduced by increasing the fluid velocity. Thus, in the polymer fluid flow, the particles will be immersed in the viscous sub layer which is thicker (i.e., higher fluid velocity is required in order to bring the viscous sub-layer thickness to the same size of the particle diameter) than in the water flow case. This explains why higher critical velocities are required in the polymer fluid cases.

Additionally, since higher viscosities are obtained as the polymer concentration is increased (see figures 6-8 and 6-9), higher values of viscous sub-layer thickness are presented in the 0.1% V/V polymer fluid flow case than that of the 0.07% V/V polymer fluid flow. This explains why higher critical velocities are required in the 0.1% V/V polymer fluid flow case.

6.3.4 Critical Velocity to Initiate Movement of Large Size Range Particles in Various Flow Patterns

Table 6-10 summarizes the flow patterns observed while transporting particles of 1.2 mm mean diameter range with water. The critical velocity to commence particle movement in rolling was 0.31 m/s. As the fluid velocity was increased slightly above the critical velocity of rolling (i.e., 0.33 m/s), dunes/saltation flow pattern were observed. The dunes/saltation flow pattern sustained for long time as the fluid velocity was increased stepwise up to 1.0 m/s. We were not able to observe suspension flow pattern as all the

particles were cleaned up from the annulus in dunes/saltation mode. Comparing these results with the results from experiments where small diameter particles were transported by water, it can be concluded that slightly higher critical velocity is required by increasing the particle diameter. This can be explained because of the fact that even though for particle diameters larger than the viscous sub-layer thickness, the particle will be in the outer region (Logarithmic zone) facing higher velocities, the change in the local velocity does not compensate the increase in the mass of the particle (weight of the particle is proportional to the cube as shown in equation 2) and therefore, in this case the critical velocity required to commence particle movement is higher for the larger particle diameters.

Table 6 - 10. Flow Patterns of Solids Transport Observed with Water – d_{50}: 1.2 mm.

Water – 1.2 mm	
Velocity[m/s]	Bed Type
0.16	Stationary Bed
0.21	Stationary Bed
0.25	Stationary Bed
0.27	Stationary Bed
0.29	Stationary Bed
0.31	Critical Velocity - Rolling
0.33	Dunes/Saltation
0.40	Dunes/Saltation
0.4-1.0	Dunes/Saltation

Table 6-11 and 6-12 summarizes the flow patterns observed while transporting particles with 1.2 mm mean diameter range using carrier fluids of 0.07%V/V polymer concentration, and 0.1%V/V polymer concentration, respectively. When 0.07%V/V polymer solution was used as carrier fluid, the critical velocity to initiate particle movement in rolling was 0.66 m/s. Following the particle movement in rolling mode, dunes were observed, forming a saltation flow pattern when the bulk fluid velocity was increased up to 0.76 m/s. We were not able to achieve particle movement in suspension mode as all the particles were cleaned up from the annulus in dunes/saltation mode.

When 0.1%V/V polymer solution was used as carrier fluid, the critical velocity to initiate particle movement in rolling was 0.80 m/s. Dunes were observed, forming a saltation flow pattern when the bulk fluid velocity was increased up to 0.91 m/s. We were not able to achieve particle movement in suspension mode as all the particles were cleaned up from the annulus in dunes/saltation mode.

The critical velocity to initiate particle movement in rolling increased from 0.66 m/s to 0.80 m/s when polymer concentration of the carrier fluid changed from 0.07%V/V to 0.1%V/V. As in the small particle size range case, the higher critical velocity was obtained at the higher polymer concentration. The reason for this behavior was explained earlier by taking into account the viscous sub-layer thickness, which becomes thicker as the polymer concentration increases.

Table 6 - 11. Flow Patterns of Solids Transport Observed with 0.07% V/V PHPA Solution – d_{50}: 1.2 mm.

PHPA 0.07% V/V - 1.2 mm	
Velocity[m/s]	Bed Type
0.60	Stationary Bed
0.63	Stationary Bed
0.66	Critical Velocity – Rolling
0.70	Rolling
0.76	Dunes/Saltation
0.82	Dunes/Saltation
0.87	Dunes/Saltation
0.91	Dunes/Saltation
0.97	Dunes/Saltation

Table 6 - 12. Flow Patterns of Solids Transport Observed with 0.1% V/V PHPA Solution - d_{50}: 1.2 mm.

PHPA 0.1% V/V - 1.2 mm	
Velocity[m/s]	Bed Type
0.73	Stationary Bed
0.77	Stationary Bed
0.80	Critical Velocity - Rolling
0.84	Rolling
0.91	Dunes/Saltation
0.96	Dunes/Saltation
1.01	Dunes/Saltation

Comparing these results from large particle size (d_{50} = 1.12 mm) experiments to the ones obtained from the small particle size (d_{50} = 350 micron) experiments, it was seen that much lower critical velocities were needed to move large size particles with polymer fluid than that of small size particles. As explained earlier, the viscous sub-layer thickness (where the local velocities are low) is higher in the polymer fluid flow than that of water flow, reaching a value larger than the particle diameter. The viscous sub-layer thickness need to be reduced to the same order of magnitude of the particle diameter, so that the particle can be exposed to higher local velocities, which would be strong enough to commence particle movement. It was also explained earlier that based on the definition of viscous sublayer thickness given by the equation 10, the viscous sub-layer thickness can be reduced by increasing the fluid flow rate. Therefore, in large particle size case, the flow rate required to reduce the viscous sub-layer thickness to the same order of magnitude of the particle diameter is lower than that of the smaller particle diameter case. This explains why lower critical velocities are required to commence movement of large size particles (as compared to small particle size case) with the polymer fluid flow.

6.3.5 Frictional Pressure Drop Measurement - Water and Polymer Fluid Flow with No Solids

Figure 6-24 shows the frictional pressure drop data measured at various velocities of water and polymer fluid flow without bed of particles.

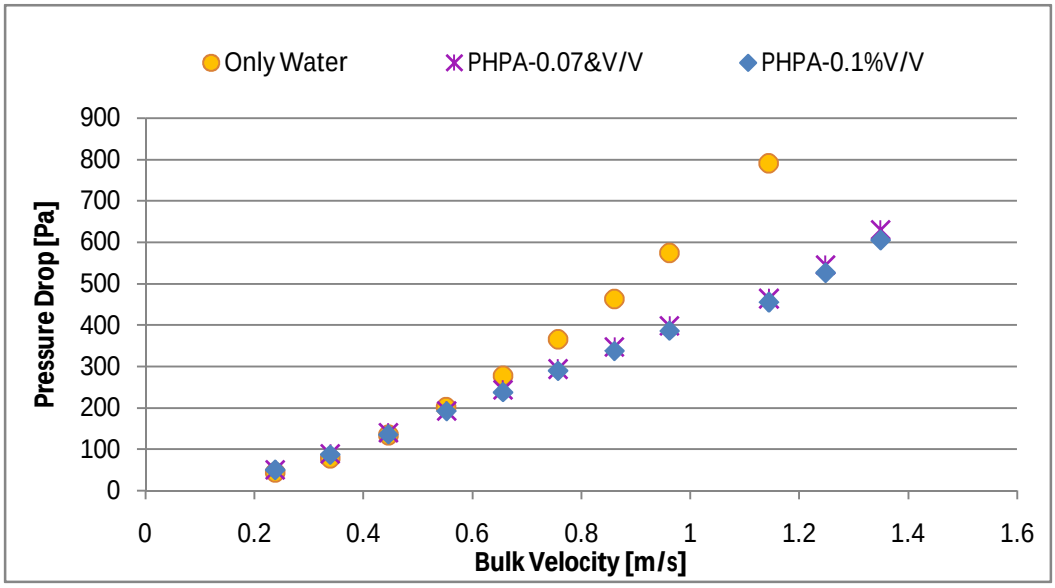

Figure 6 - 24. Pressure Drop for Water and Polymer Fluid Flow Without Solids.

It is observed that for velocities below 0.55 m/s the frictional pressure drop is very similar for water and polymer fluid flow. On the other hand, for velocities higher than 0.55 m/s, the drag reduction starts taking place, and lower pressure drops are obtained in the polymer flow cases, being the lowest in the 0.1%V/V polymer fluid case. This concentration was demonstrated to be the optimum polymer concentration in chapter 5.

Figure 6-25 shows the drag reduction obtained at different flow rates using polymer fluid with a concentration equal to 0.07%V/V and 0.1%V/V. It can be observed that in order to have a benefit of the polymer as a drag reducer, the fluid velocity should be higher than 0.55 m/s. After that velocity, the drag reduction is increased by increasing the flow rate. A maximum drag reduction of 42% is achieved for a polymer concentration equal to

0.1%V/V at the highest flow rate. As shown in chapter 5, even thought 0.1% V/V is the optimum concentration, the difference in drag reduction between the 0.1 and 0.07% V/V polymer solution is not bigger than 4%. .

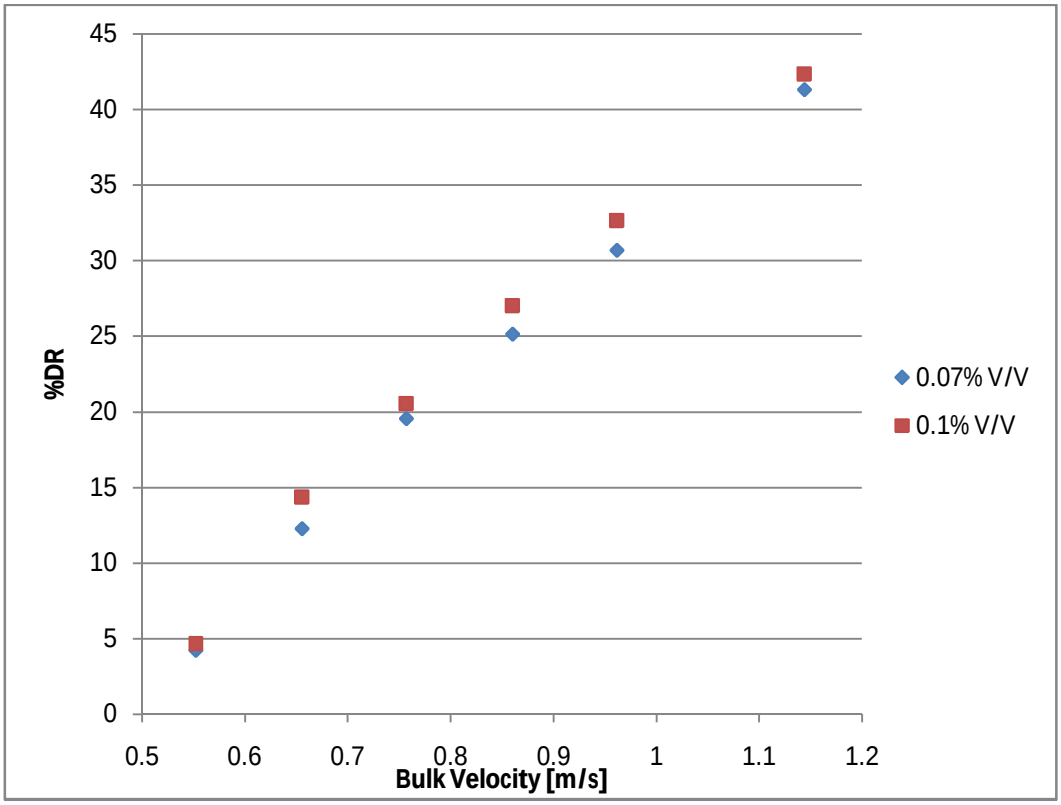

Figure 6 - 25. Drag Reduction Obtained by the Flow of Polymer Fluids.

6.3.6 Frictional Pressure Drop Measurement –Water and Polymer Fluid Flow with Solids

Figure 6-26 shows the pressure drop versus bulk velocity obtained for water flow using a bed of particles with a mean particle diameter of 350 microns. It can be noticed that the slope is different at each flow pattern. The changes in the slope allow us to identify the transition between different modes of solids transport. These results confirm the results obtained by the video camera.

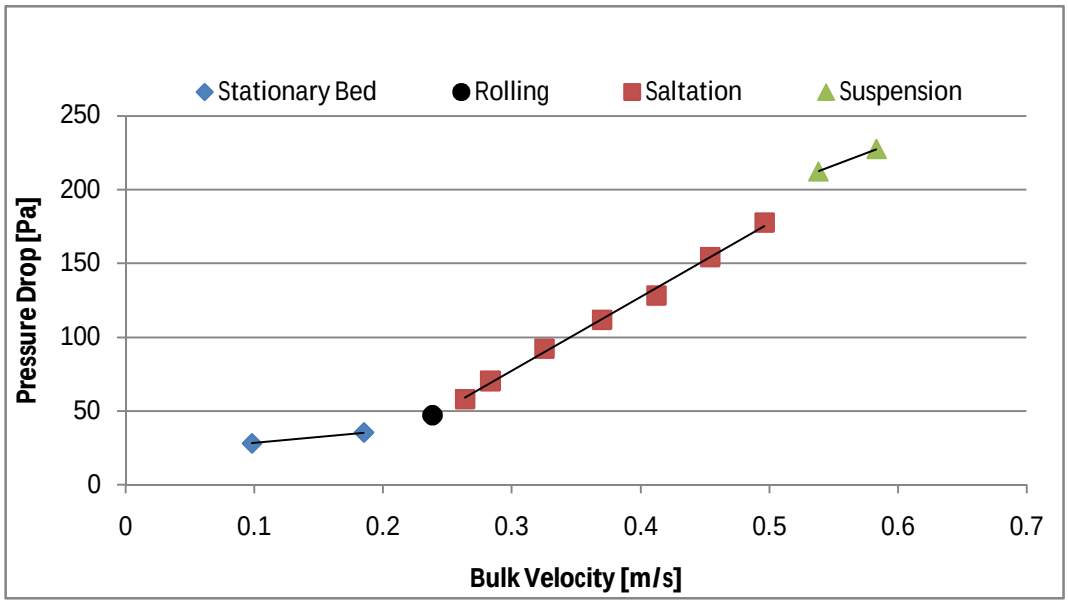

Figure 6 - 26. Pressure Drop Versus Bulk Fluid Velocity While Transporting Cuttings With Water - Mean Particle Diameter: 350 Microns.

The frictional pressure drop data measured at different bulk fluid velocity for the polymer fluid flow are shown in figure 6-27. As in the water case, different slopes of lines are obtained indicating the variation of the flow patterns of solids transport. These results also confirm the visual recordings of the flow patterns obtained by video camera. Lower pressure drops were obtained for the 0.07% V/V polymer fluid flow than that of the 0.1% V/V in the stationary bed condition. Higher frictional pressure drop (corresponding to higher critical velocity) was observed to initiate cuttings movement in rolling when using fluid with 0.1% V/V polymer concentration than that of fluid with 0.07%V/V polymer concentration.

As shown earlier in figures 6-22 and 6-23, the dunes get smaller and separated far from each other at high flow velocity. This produces high fluctuations in the pressure drop and therefore, obtaining a representative value of pressure drop after exceeding the bulk fluid velocity of 0.97 m/s was not possible.

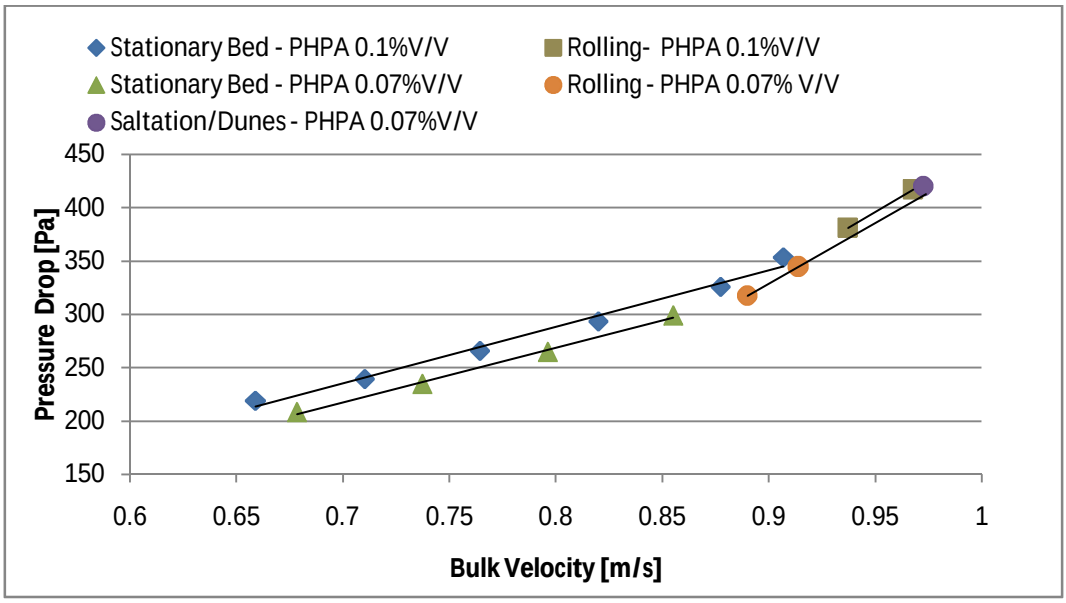

Figure 6 - 27. Pressure Drop Versus Bulk Fluid Velocity for Polymer Fluid Flow - Mean Particle Diameter: 350 Microns.

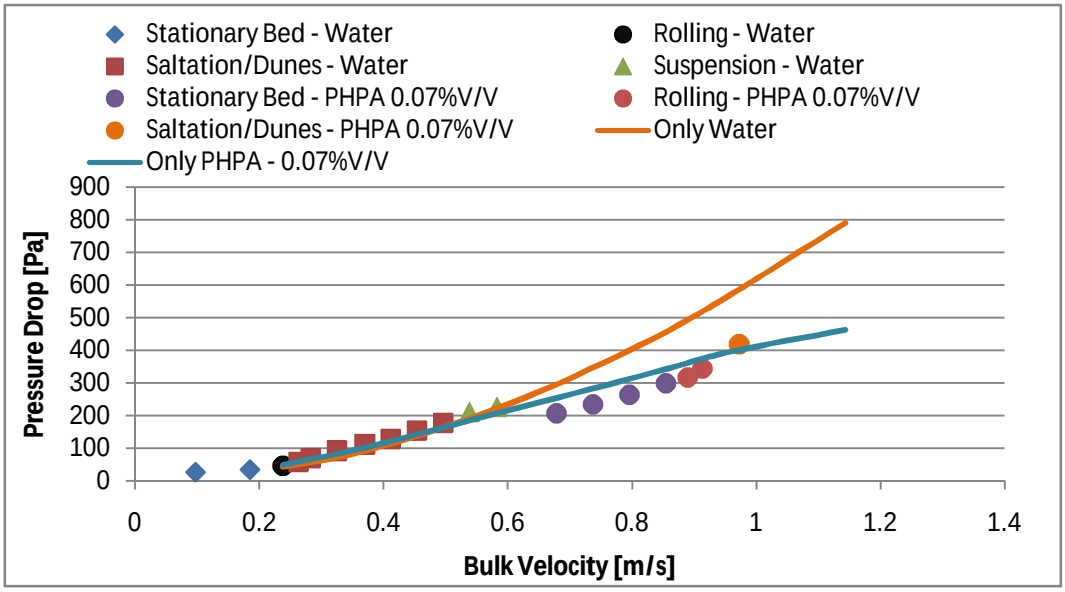

Figure 6 - 28. Pressure Drop Versus Bulk Fluid Velocity During Solids Transport Experiments - Comparison of Best Polymer Fluid Flow (0.07% V/V) and Water Flow - Mean Particle Diameter: 350 microns.

Figure 6-28 shows the comparison between the pressure drops obtained when transporting solids with water and with the best polymer fluid flow case. The best

polymer fluid was defined as fluid with the polymer concentration yielding to the smaller critical velocity to commence particle movement, which was 0.07% V/V. The data obtained when circulating water and polymer fluid without the presence of solid particles were also included in Figure 6-28 for comparison purposes.

Solids removal performance seems to be better in the water flow case than in the polymer fluid flow. The critical velocity (and hence, the associated frictional pressure drop) of initiation of particle rolling is much lower in the case of water than that of polymer fluid flow. For instance, at a bulk fluid velocity of 1 m/s, when we use polymer, fluid particles are transported in dunes/saltation mode. When we use water, however, the particles are transported in full suspension at a bulk velocity of 1 m/s. Therefore, a faster cleaning process is expected to occur in the water flow case.

However, it may not be possible to transport the cuttings in full suspension all the time, especially when cleaning long horizontal and extended reach wells where the frictional pressure drops encountered could be extremely high. Under these circumstances, it is required to minimize the frictional pressure drops in order to avoid operational problems such as exceeding the pump capacity or fracturing the formation, therefore, particle transport in dunes/saltation mode (yielding the lower pressure drop) would be more feasible.

Besides reaching the operational limits (i.e.; pump capacity, fracturing the formation), one of the major concerns associated with hole cleaning operations is the extended circulation time, which may be very costly in the case of long horizontal and extended reach wells. Therefore, when deciding on which fluid is the best for meeting the hole cleaning demands of the specific well design, we need to look into both anticipated pressure losses as well as the net transport velocity of solids.

When cuttings are transported in dunes/saltation mode, net transport velocity of solids can be faster (i.e., shorter time to clean the well) when using polymer fluids than that of using water as a carrier fluid. Therefore, we measured the velocity of the dunes under various fluid type/velocity conditions and the results will be discussed later in this chapter.

Figure 6-29 show the pressure drop versus bulk fluid velocity data obtained from solid transport experiments using water and particles with mean diameter of 1.2mm. As in the small particle diameter case, different slopes were obtained at each flow pattern. The first change in the slope was seen after achieving a fluid velocity of 0.31 m/s, which was the critical velocity to commence particle movement in rolling as reported in Table 6-10. These results also confirm the critical velocity and flow patterns obtained using the video camera.

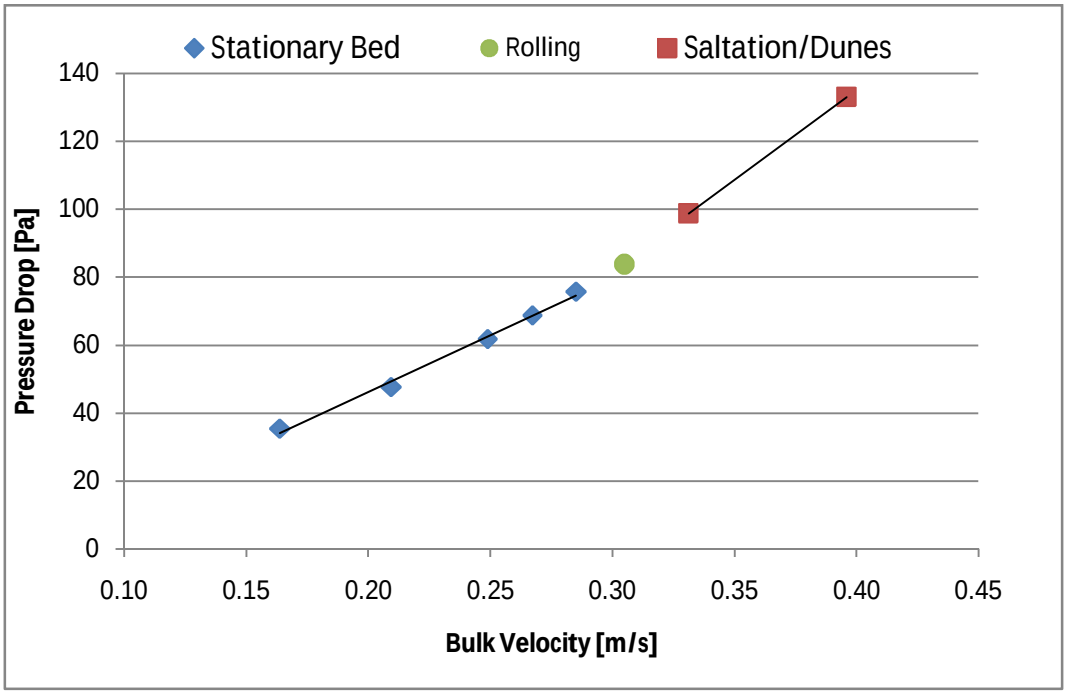

Figure 6 - 29. Pressure Drop Versus Bulk Fluid Velocity - Water Flow – Mean Particle Diameter: 1.2mm.

Figure 6-30 shows the pressure drop versus bulk fluid velocity obtained from experiments using polymer fluids and particles with mean particle diameter of 1.2 mm. Unfortunately, it was not possible to get pressure readings in the saltation domain due to the high pressure fluctuation. As it will be shown and discussed later, the dunes of the coarse particles are transported by the polymer fluid faster than dunes of the fine particles. This makes the pressure fluctuation increase significantly as explained by Takahashi et al., [8]. However, figure 6-30 shows an interesting finding. Although, the critical velocity to commence particle movement in rolling was higher with fluid of higher polymer concentration, the pressure drop obtained was very similar for both fluids at their critical velocities. This is because in this case the difference in drag reduction between the 0.1%V/V and 0.07%V/V polymer fluid flow got more noticeable and lower pressure drops were encountered when using 0.1%V/V polymer fluid flow.

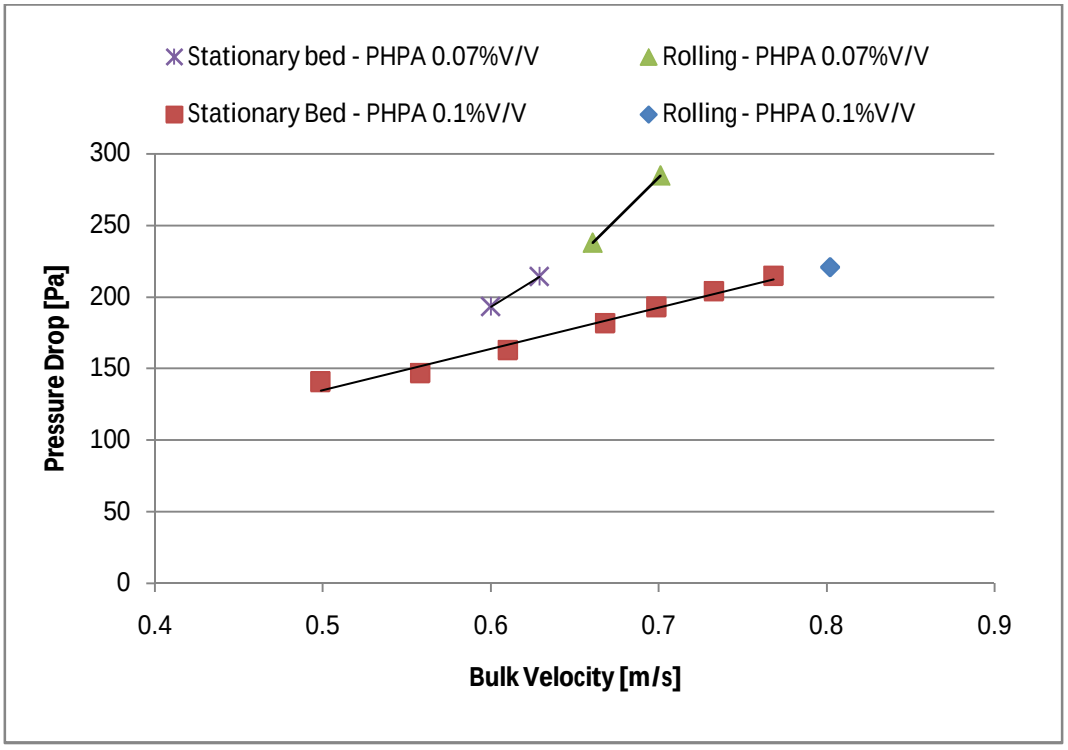

Figure 6 - 30. Pressure Drop Versus Bulk Fluid Velocity - Polymer Fluid Flow - Mean Particle Diameter: 1.2 mm.

Figure 6-31 shows a comparison of the results from solids transport experiments with water and with best polymer fluid case (0.07%V/V) using a mean particle diameter equal to 1.2 mm. Data obtained from experiments using water and polymer fluid without bed of particles were also presented in Figure 6-31 for comparison purposes.

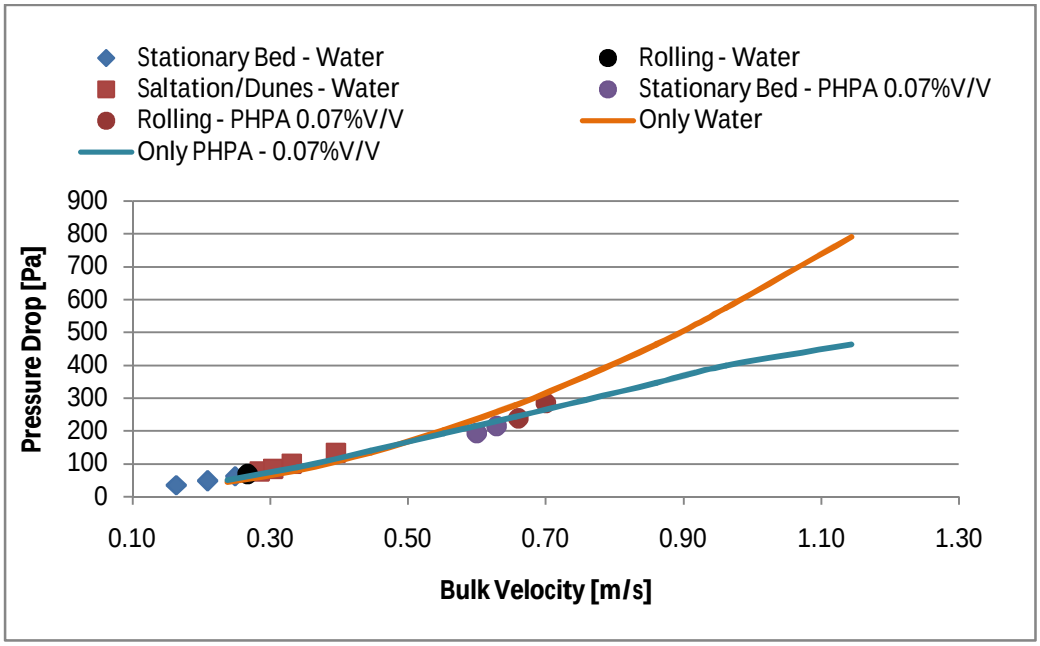

Figure 6 - 31. Comparison of the Pressure Drop Versus Bulk Fluid Velocity Data - Polymer Fluid (0.07% V/V) versus Water Flow - Mean Particle Diameter: 1.2 mm.

The benefit of using polymer in reducing the pressure drop (i.e., drag reduction effect) is only noticeable after bulk fluid velocity exceeds 0.7 m/s. Before that, the reduction in the pressure drop (as compared to water flow at the same rate) is almost insignificant.

The solids transport performance is much better in the water flow case. Critical velocity of initiating particle rolling with water (0.31 m/s) is much lower than that of with the polymer flow (0.66 m/s).

Close to critical velocity of the polymer fluid flow (i.e., between 0.66 and 0.7 m/s), the pressure drop is almost the same for both in water and polymer fluid flow. However, at this bulk fluid velocity range, the flow pattern observed in water flow was the dune/saltation with fully developed dunes, whereas in the polymer flow case the dunes just start to form.

Besides reaching the operational limits due to high frictional pressure losses(i.e.; pump capacity, fracturing the formation), one of the major concerns associated with hole cleaning operations is the extended circulation time, which may be very costly in the case of long horizontal and extended reach wells. Therefore, when deciding on which fluid is the best for meeting the hole cleaning demands of the specific well design, we need to look into both anticipated pressure losses as well as the net transport velocity of solids. When cuttings are transported in dunes/saltation mode, net transport velocity of solids can be faster (i.e., shorter time to clean the well) when using polymer fluids than that of using water as a carrier fluid. Therefore, we measured the velocity of the dunes under various fluid type/velocity conditions and the results will be discussed next in this chapter.

Table 6-13 shows a summary of the critical velocity and pressure drop required to initiate particle movement in Rolling for all the fluid cases (polymer fluid and water) using both mean particle diameters.

Table 6 - 13. Critical Velocities and Pressure Drop Required to Initiate Particle Movement in Rolling.

Fluid	Mean d_p [mm]	Critical Velocity for Rolling [m/s]	Critical Pressure Drop [pa]
Water	0.35	0.24	47
PHPA 0.07%V/V	0.35	0.89	318
PHPA 0.1%V/V	0.35	0.94	381
Water	**1.2**	**0.31**	**84**
PHPA 0.07%V/V	**1.2**	**0.66**	**238**
PHPA 0.1%V/V	**1.2**	**0.8**	**221**

It can be observed that the critical velocity and pressure drop required for initiating rolling movement are smaller for the water flow than that of the polymer fluid flow in both particle diameters.

For the water case, higher critical velocity and pressure drop are required to initiate rolling movement by increasing the mean particle diameter. However, Critical velocity and pressure drop required for initiating rolling movement of large size particles (d_{50}=1.12 mm) with polymer fluid are lower than that of required for moving smaller size particles (d_{50}=350 micron).

Higher critical velocity and pressure drop are required by increasing the polymer concentration in both particle sizes. This is because of the increased viscosity obtained when using the higher polymer concentration solution.

6.3.7 Dunes Velocity

Figures 6-32 to 6-34 show the dunes velocity obtained at different bulk fluid velocities for water and fluids with 0.07 % V/V and 0.1%V/V polymer concentrations, respectively. Particles with mean diameter of 350 microns (i.e., small particle size range) were used in these experiments.

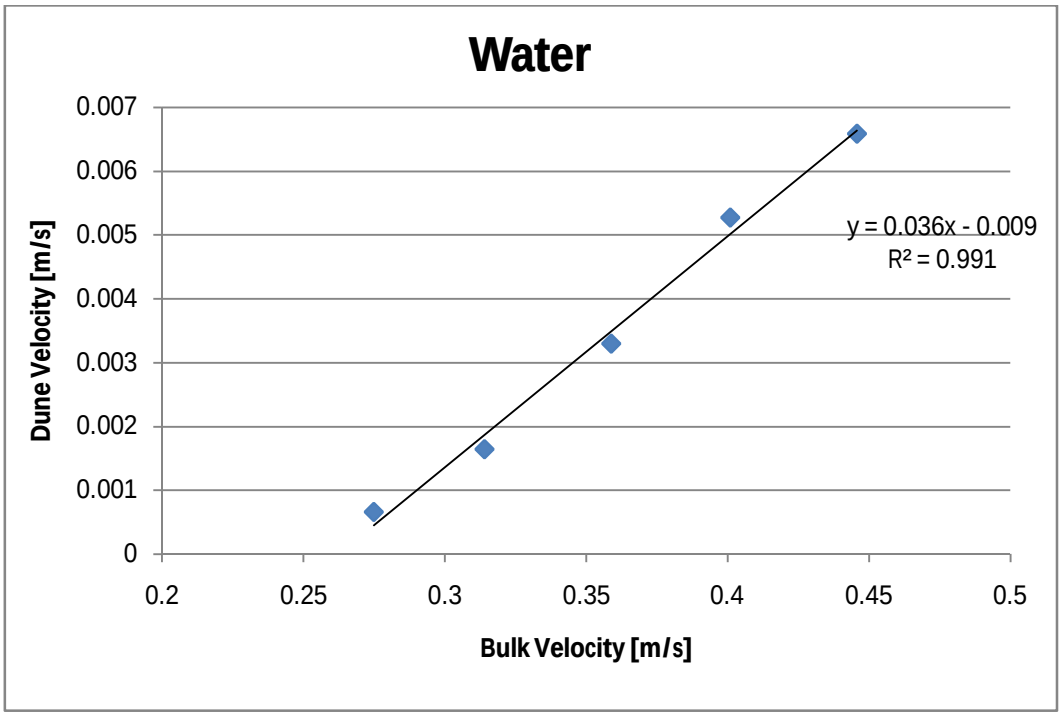

Figure 6 - 32. Dunes Velocity Versus Bulk Fluid Velocity - Water Flow - Mean particle Diameter: 350 Microns.

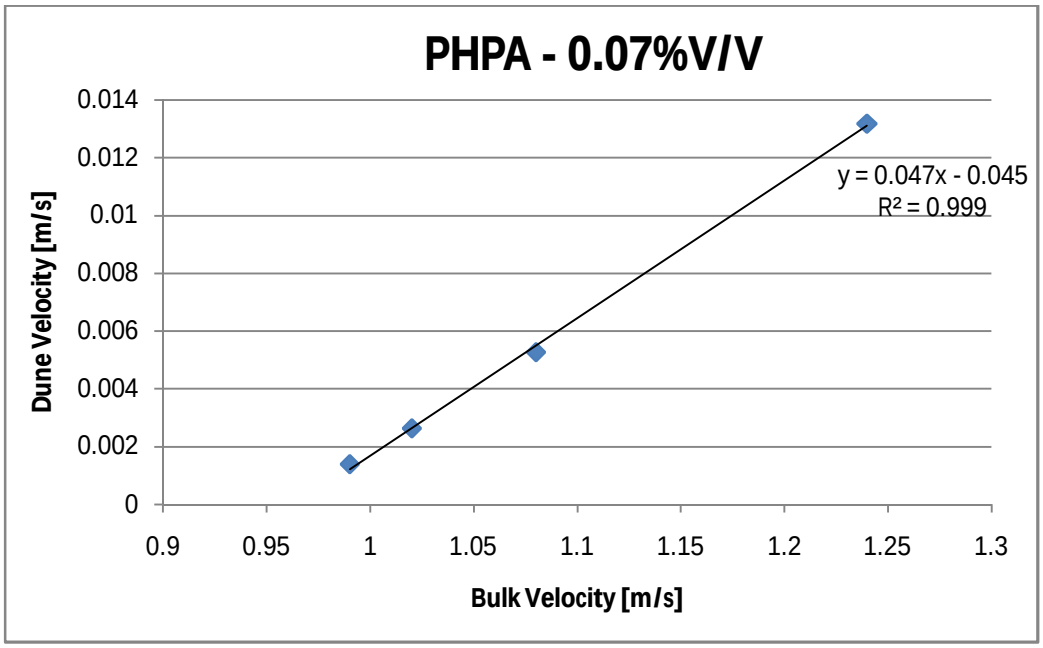

Figure 6 - 33. Dunes Velocity Versus Bulk Fluid Velocity - PHPA 0.07%V/V - Mean particle Diameter: 350 Microns.

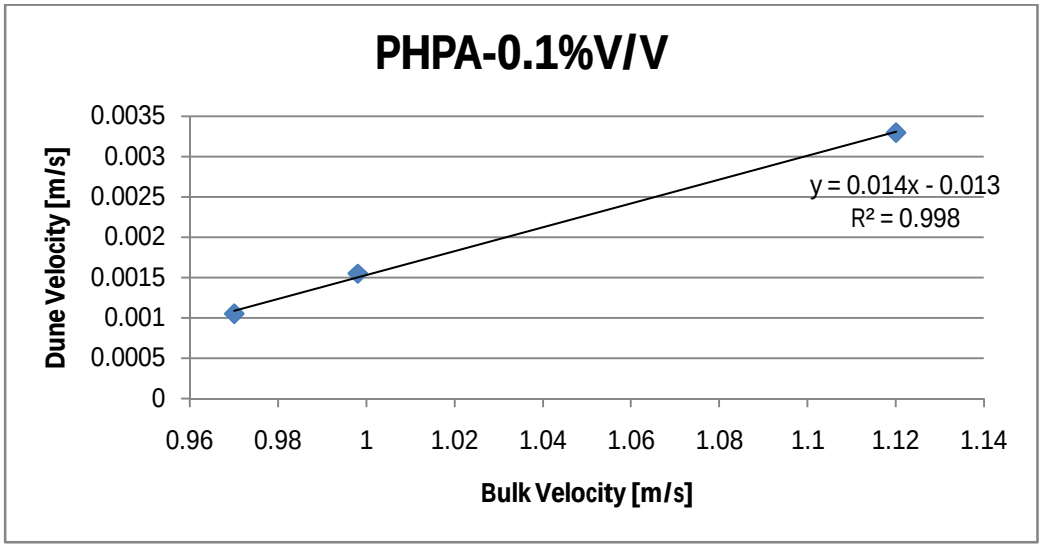

Figure 6 - 34. Dunes Velocity Versus Bulk Fluid Velocity - PHPA 0.1%V/V - Mean particle Diameter: 350 Microns.

In all cases investigated here, a linear correlation between the dunes velocity and the bulk fluid velocity was observed.

Figures 6-35 shows the comparison of the dunes velocity results from small size (d_{50}=350 micron) particles transport experiments conducted by using water and polymer fluid.

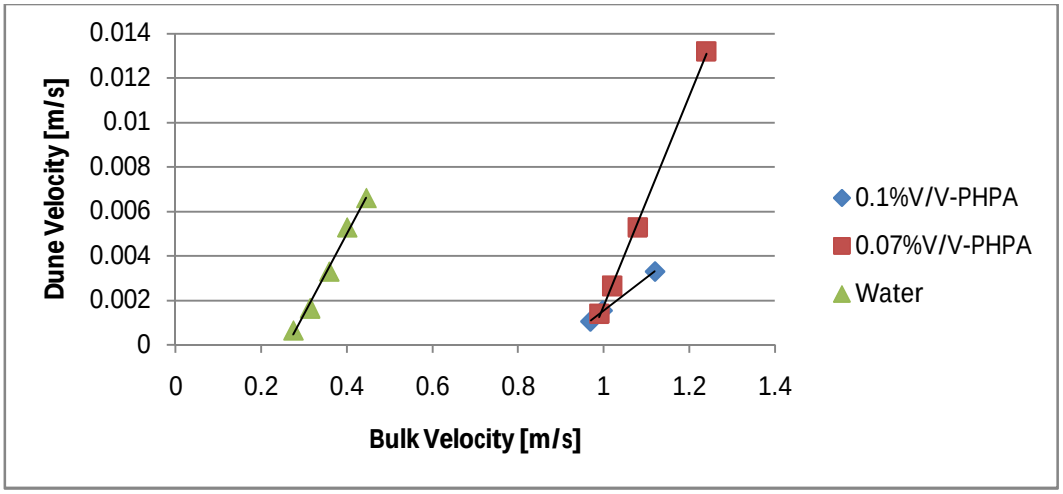

Figure 6 - 35. Comparison Between the Dunes Velocity Obtained for Polymer Fluid Flow and Water Flow - Mean Particle Diameter Equal to 350 Microns.

As we have discussed earlier, much lower critical velocities are required to initiate particle movement in rolling and or dunes/saltation mode when using water as carrier fluid. Ultimately, lower pressure losses are also anticipated when transporting particles with polymer as compared to water. However, when we compare the net transport velocity of dunes, we see that higher net transport velocities are achieved when using polymer fluids than that of with water. In other words, for the same transport mode of cuttings (let's say, saltation/dunes mode) cuttings can be transported much faster with polymer fluid than that of with water.

As long as we do not exceed the operational limits (i.e., pump pressure capacity, formation fracture pressure, etc.), hole cleaning can be achieved in shorter time by using polymer fluid. Faster net transport velocity means shortened hole cleaning time which might help reducing the cost associated with hole cleaning operations routinely conducted in horizontal and extended reach wells.

Figures 6-36 to 6-38 show the dunes velocity obtained at different bulk fluid velocities for water and fluids with 0.07 % V/V and 0.1%V/V polymer concentrations, respectively. Particles with mean diameter of 1.2 mm (i.e., large particle size range) were used in these experiments.

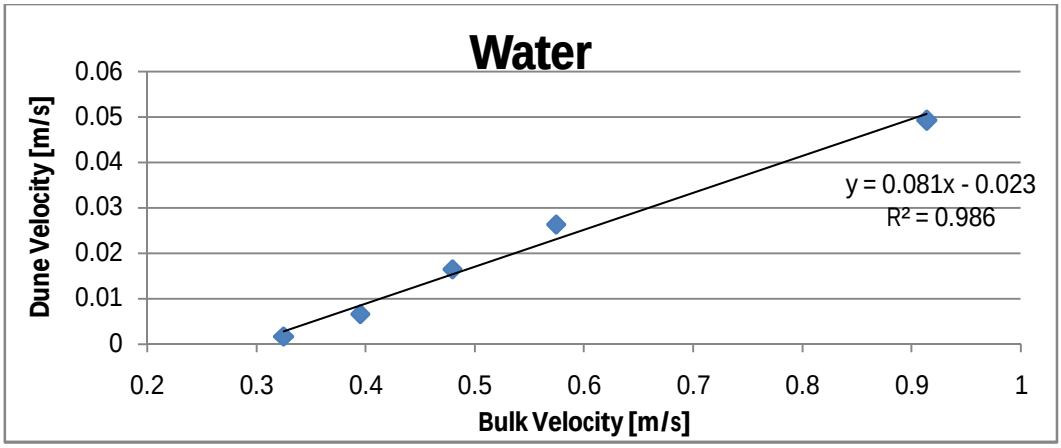

Figure 6 - 36. Dunes Velocity Versus Bulk Fluid Velocity - Water Flow - Mean particle Diameter Equal: 1.2 mm.

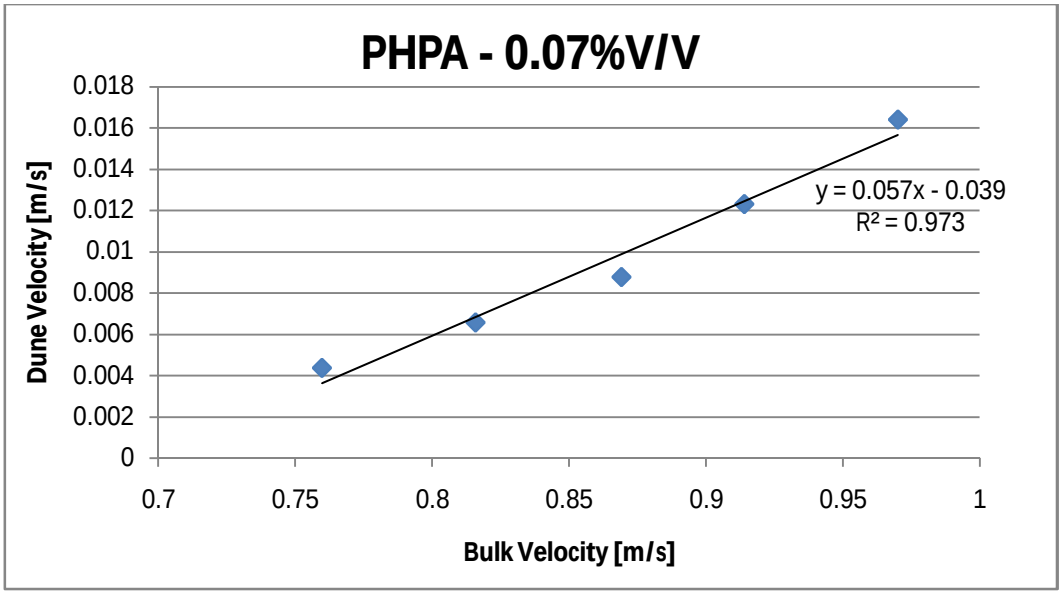

Figure 6 - 37. Dunes Velocity Versus Bulk Fluid Velocity - PHPA 0.07%V/V - Mean particle Diameter Equal: 1.2 mm.

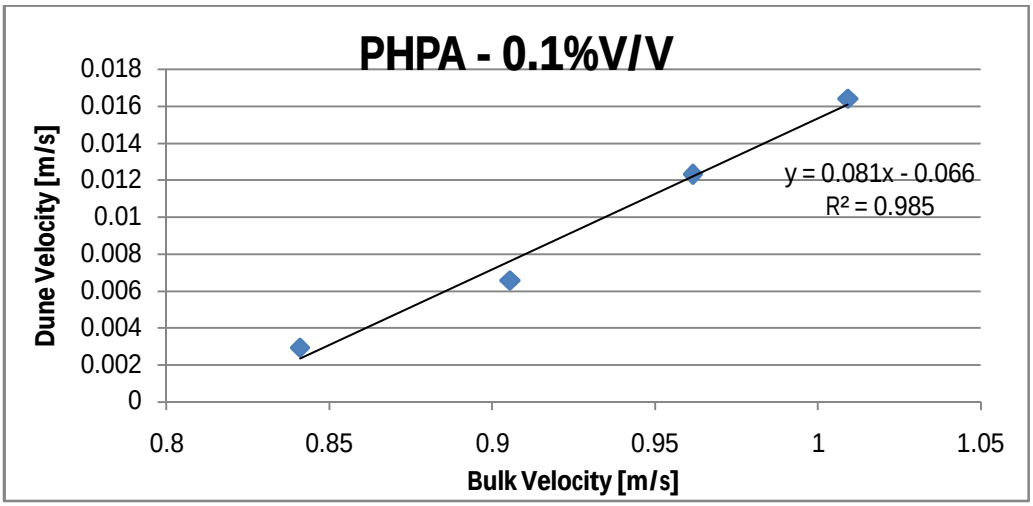

Figure 6 - 38. Dunes Velocity Versus Bulk Fluid Velocity - PHPA 0.1%V/V – Mean particle Diameter: 1.2 mm.

As in the small particle transport cases, it was observed that the dunes velocity increased linearly with the increasing bulk fluid velocity.

Figure 6-39 shows the comparison of the dunes velocity results from large size (d_{50}=1.12 mm) particles transport experiments conducted by using water and polymer fluid.

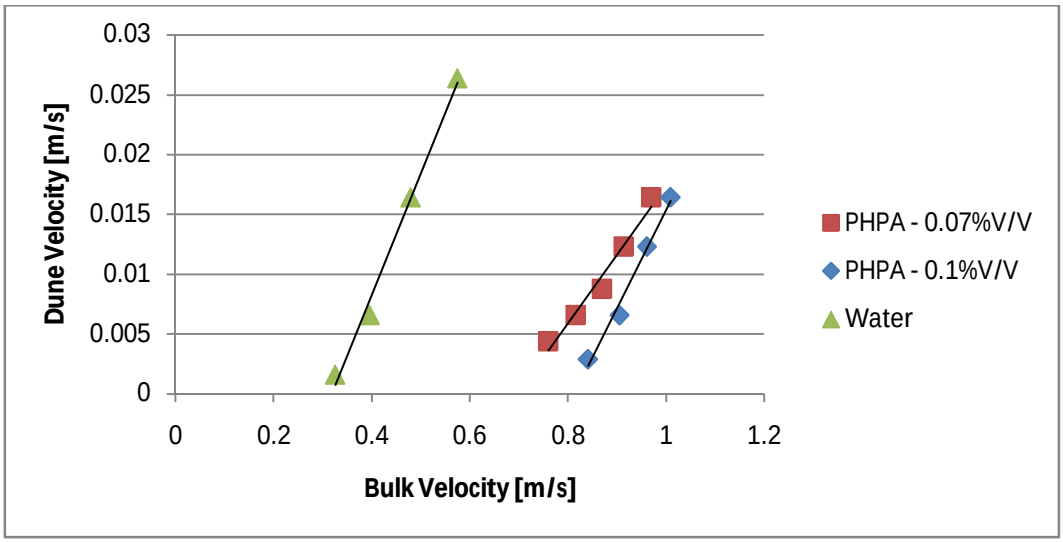

Figure 6 - 39. Comparison Between the Dunes Velocity Obtained for Polymer Fluid Flow and Water Flow - Mean particle Diameter: 1.2 mm.

Net transport velocities of dunes were found to be higher in water than in polymer fluids. This is in contrast to what we observed in experiments with small particle diameter range where the polymer fluid caused the highest net transport velocity. This is because in the small particle range dunes were obtained in water at low flow velocities $0.26 < U_b < 0.5$ m/s whereas in large particle range dunes were obtained for water at high flow velocities $0.3 < U_b < 0.91$ m/s.

The dunes were transported at slightly higher velocities with 0.07% V/V polymer fluid as compared to 0.1% V/V polymer fluid.

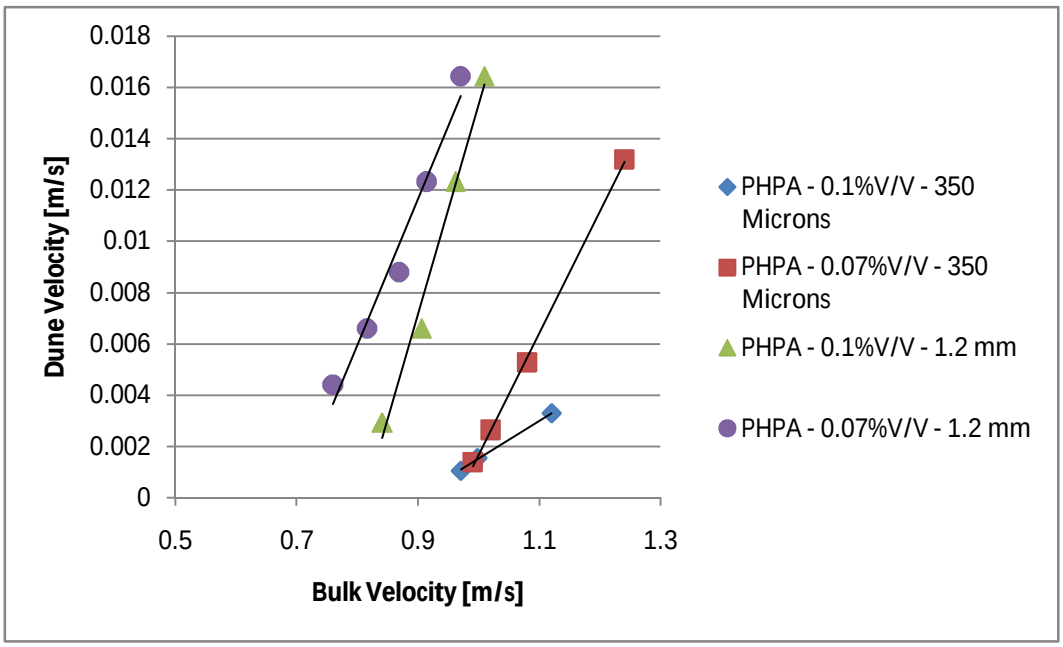

Figure 6 - 40. Comparison of the Dunes Velocity - Polymer Fluids – Small Particle Size Versus Large Particle Size.

Figure 6-40 shows comparison of the dunes velocities obtained by using both particles diameters (350 microns and 1.2 mm) and both polymer fluids. It can be noticed that the solid removal performance is much better with the coarser particles. For example at bulk fluid velocity around 1 m/s, the dunes velocity obtained for the finer particles is around

0.001 m/s in both polymer fluids; however, in the coarser particles the dunes velocity at that this bulk fluid velocity is much higher, being around 0.016 m/s. This is because at this bulk fluid velocity, the larger particles are more likely to stick out from viscous sub-layer (where the local velocities are low) and get exposed to higher fluid velocities within the logarithmic zone away from the wall.

Table 6-14 shows a summary of the critical velocity and pressure drop required for dunes formation and net Transport velocity of dunes at critical condition for all the fluid cases (polymer fluid and water) using both mean particle diameters.

Table 6 - 14. Critical Velocities for Dunes Formation and Net Transport Velocity of Dunes at Critical Condition

Fluid	Mean dp [mm]	Critical Velocity Dunes[m/s]	ΔP [Pa]	Net transport velocity of dunes at critical condition [m/s]
Water	0.35	0.26	58	0.00066
PHPA 0.07%V/V	0.35	0.97	420	0.001387
Water	**1.2**	**0.33**	**99**	**0.0016**
PHPA 0.07%V/V	**1.2**	**0.76**	**343**	**0.0043**

It can be observed that the critical velocity and pressure drop required for dunes formation are smaller for the water flow than that of the polymer fluid flow in both particle diameters. However, at critical conditions the net transport velocity of dunes is observed to be higher in the polymer fluid flow case.

For the water case, higher critical velocity and pressure drop are required for dunes formation by increasing the mean particle diameter. However, critical velocity and pressure drop required for dunes formation using larger size particles (d_{50}=1.12 mm) with polymer fluid are lower than that of required for dunes formation using smaller size

particles (d_{50}=350 micron). Additionally, when using polymer fluid at critical conditions for dunes formation, higher net transport velocity of dunes is obtained when removing larger particles than that of the smaller particles.

6.4 Practical Use of Solids Transport and Drag Reduction Results

While drilling long horizontal and extended reach wells, due to deposition of drilled solids on the low side of the well, drilling is often stopped and routine hole cleaning operations need to be conducted. Reaching the operational limits due to high frictional pressure losses (i.e., pump capacity, fracturing the formation) as well as the extended circulation time (which may be very costly in the case of long horizontal and extended reach wells) are the two major concerns associated with hole cleaning operations. Therefore, when deciding on which fluid is the best for meeting the hole cleaning demands of the specific well design, we need to look into both anticipated pressure losses as well as the efficiency of solids transport (i.e., net transport velocity of solids).

Cuttings transport performance of water and drag reducing fluid show some differences depending on the particle size. Therefore, we would like to discuss the practical implications of the experimental results presented here separately for small and large cuttings size categories.

6.4.1 Cuttings Transport Performance of Water/Drag Reducing Fluid (0.07% V/V PHPA) in Small Particle Size Range

As we have discussed earlier, much lower critical velocities are required to initiate particle movement in rolling and or dunes/saltation mode when using water as carrier fluid (0.24 m/s for rolling and 0.26 m/s for dunes formation) compared to drag reducing fluid (0.89 m/s for rolling and 0.97 m/s for dunes formation). Consequently lower

frictional pressure gradients are encountered with water flow (15.26 Pa/m for rolling and 18.8 Pa/m for dunes formation) as compared to drag reducing fluid flow (103.25 Pa/m for rolling and 136.36 Pa/m for dunes formation).However, when cuttings are transported in dunes/saltation mode, net transport velocity of solids can be faster (i.e., shorter time is required to clean the well) when using polymer fluids (0.001387 m/s at critical dunes formation condition) than that of using water (0.00066 m/s at critical dunes formation condition) as a carrier fluid.

Practical implication of this observation is that, as long as we do not exceed the operational limits (i.e., pump pressure capacity, formation fracture pressure, etc.), hole cleaning can be achieved in shorter time by using drag reducing fluids. Shortened hole cleaning time would help reducing the cost associated with hole cleaning operations routinely conducted in horizontal and extended reach wells.

6.4.2 Cuttings Transport Performance of Water/Drag Reducing Fluid (0.07% V/V PHPA) in Large Particle Size Range.

The results show that solids removal performance of drag reducing fluid was more efficient in the case of coarser particles than that of finer particles. Comparison of the velocity profiles for water and drag reducing solutions (as discussed in Chapter 5) shows that above the viscous sub-layer region(i.e., in core flow region), the local velocities due to drag reducing fluid flow are significantly higher than that of water flow. When cleaning bed deposits of large particle sizes (i.e, particle diameter > 3 mm), particles will be either in the buffer zone or in the core flow region for both water and drag reducing flow. Consequently, for the same bulk fluid velocity condition (i.e., average velocity), large particles will be exposed to higher local velocities when they are transported using drag reducing fluid than that of using water. Higher net transport velocities of dunes were

also observed when transporting large particle sizes using drag reducing fluid as carrier fluid. Practical implication of these results is that large particles can be mobilized at lower bulk fluid velocities (i.e., lower critical velocity for particle movement in rolling) using drag reducing fluid. Moreover, when we use drag reducing fluid, we may benefit from reduction of frictional pressure losses (in our particular case it was as high as 42%). Another advantage of adding polymer to the flow is that the viscosity is increased and therefore, all the cuttings removed from bed deposits (lying at the low side of the well) are more efficiently held within the fluid (i.e., lower particle-settling velocity) while being transported to the surface especially in the vertical section.

In summary, when removing large size cuttings (>3mm, which are commonly generated in drilling operations), better solids removal performance can be expected when using drag reducing polymer fluids as compared to water. Shorter hole cleaning times and lower pressure drop might be obtained using polymer fluid than that of using water. More experiments, however, need to be conducted by using large size cuttings (larger than the ones used in these; > 1.2 mm) to support the preliminary observations presented here.

6.5 Conclusions

As compared to particle transport with water, significantly higher critical velocities were required when transporting particles by drag reducing fluids. This is because the viscous sub-layer thickness (where the local velocities are low) is higher in drag reducing fluid flow than that of water flow, reaching a value larger than the size of the particles used. Therefore, higher bulk velocities are required to reduce the viscous sub-layer thickness to the same order of magnitude of the particles in order to expose the particles to higher local velocities, which would be strong enough to initiate particle movement.

Additionally, higher critical velocities were required after increasing the polymer concentration.

In the water flow case, higher critical velocities to initiate particle movement in rolling were obtained for the coarser particles than that of the finer particles. This is because of the fact that even though for particle diameters larger than the viscous sub-layer thickness, the particle will be in the outer region (Logarithmic zone) facing higher velocities, the change in the local velocity does not compensate the increase in the mass of the particle (weight of the particle is proportional to the cube) and therefore, in this case the critical velocity required to commence particle movement is higher for the larger particle diameters.

In the polymer fluid flow cases, lower critical velocities to initiate particle movement were obtained for the coarser particles. This is because when using drag reducing fluids as carrier fluids, the viscous sub-layer thickness is increased reaching a value larger than both of the particle sizes used. Therefore, the viscous sub-layer thickness need to be reduced to the same order of magnitude of the particle diameter, so that the particle can be exposed to higher local velocities, which would be strong enough to commence particle movement. The viscous sub-layer thickness can be reduced by increasing the fluid flow rate. Therefore, in the large particle size case, the flow rate required to reduce the viscous sub-layer thickness to the same order of magnitude of the particle diameter is lower than that of the smaller particle diameter case.

Pressure drop versus fluid velocity results shows that the slope obtained is different at each flow pattern. The changes in the slope allow us to identify the transition between different modes of solids transport. These results confirm the results obtained by the video camera.

Solids removal performance seems to be better in the water flow case than in the polymer fluid flow. The critical velocity (and hence, the associated frictional pressure drop) of initiation of particle rolling is much lower in the case of water than that of polymer flow. For instance, at a bulk fluid velocity of 1 m/s, when we use polymer fluid, particles are transported in dunes/saltation mode. When we use water, however, the particles are transported in full suspension at a bulk velocity of 1 m/s. Therefore, a faster cleaning process is expected to occur in the water flow case. However, it may not be possible to transport the cuttings in full suspension all the time, especially when cleaning long horizontal and extended reach wells where the frictional pressure drops encountered could be extremely high. Under these circumstances, it is required to minimize the frictional pressure drops in order to avoid operational problems such as exceeding the pump capacity or fracturing the formation, therefore, particle transport in dunes/saltation mode (yielding the lower pressure drop) would be more feasible.

Lower pressure losses are anticipated when transporting particles with polymer as compared to water. Moreover, when we compare the net transport velocity of dunes using the finer particles, we see that higher net transport velocities are achieved when using polymer fluids than that of with water. In other words, for the same transport mode of cuttings (let's say, saltation/dunes mode) cuttings can be transported much faster with polymer fluid than that of with water. As long as we do not exceed the operational limits (i.e., pump pressure capacity, formation fracture pressure, etc.), hole cleaning can be achieved in shorter time by using polymer fluid. Faster net transport velocity means shortened hole cleaning time which might help reducing the cost associated with hole cleaning operations routinely conducted in horizontal and extended reach wells.

When transporting the coarser particles, net transport velocities of dunes were found to be higher in water than that of polymer fluids. This is in contrast to what we observed in

experiments with small particle diameter range where the polymer fluid caused the highest net transport velocity. This is because in the small particle range dunes were obtained in water at low flow velocities $0.26 < U_b < 0.5$ m/s whereas in large particle range dunes were obtained for water at high flow velocities $0.3 < U_b < 0.91$ m/s.

In the polymer fluid flow cases, solid removal performance is much better for coarser particles than that of finer particles. For example at bulk fluid velocity around 1 m/s, the net transport velocity of dunes obtained for the finer particles is around 0.001 m/s in both polymer fluids; however, in the coarser particles the net transport velocity of dunes at this bulk fluid velocity is much higher, being around 0.016 m/s. This is because at this bulk fluid velocity, the larger particles are more likely to stick out from viscous sub layer (where the local velocities are low) and get exposed to higher fluid velocities within the logarithmic zone away from the wall.

Dunes were transported at higher velocities with 0.07% V/V polymer fluid as compared to 0.1% V/V polymer fluid.

6.6 References

[1] Kamp, A.M., and Rivero, M., 1999, "Layer Modeling for Cuttings Transport in Highly Inclined Wellbores," Proceedings of the 1999 SPE Latin American and Caribbean Petroleum Engineering Conference, Caracas, Venezuela.

[2] Clark, R.K and Bickham, K.L., 1994, "A Mechanistic Model for Cuttings Transport," Proceedings of the 1999 SPE 69th Annual Technical Conference and Exhibition, New Orleans, LA, USA.

[3] Ramadan, A., Skalle, P., and Saasen, A., 2005, "Application of a three-layer modeling approach for solids transport in horizontal and inclined channels," Chemical Engineering Science, 60 pp. 2557-2570.

[4] Nossair, A.M., Rodgers, P., Goharzadeh, A., 2012, "Influence of Pipeline Inclination on Hydraulic Conveying of Sand Particles," Proceedings of ASME 2012 International Mechanical Engineering Congress & Exposition, Houston, Texas, USA.

[5] Bello, K.O., Oyeneyin, M.B., Oluyemi, G.F and Gordon, R., 2011, "Minimum Transport Velocity Models for Suspended Particles in Multiphase Flow Revisted," SPE Annual Tehcinical Conference and Exhibition, Denver, Colorado, USA.

[6] Danielson, T.J., 2007, "Sand Transport Modelling in Multiphase Pipelines," 2007 Offshore Technology Conference, Houston, Texas, USA.

[7] Goharzadeh, A., Rodgers, P., and Touati, C., 2008, "Influence Of Slug Flow on Hydraulic Sand Dune Migration in Horizontal Pipelines," Proceedings of ASME 2008 International Mechanical Engineering Congress & Exposition, Boston, Massachusetts, USA.

[8] Takahashi, H., Masuyama, T., Noda, K. 1989, "Unstable flow of a solid-liquid mixture in a horizontal pipe," International Journal of Multiphase Flow, 15(5), pp. 831-841.

[9] Takahashi, H., and Masuyama, T., 1991, "Stability Criterion for the Surface of the Deposit Bed of Solid-Liquid Flows in Horizontal Pipes," Journal of Chemical Engineering of Japan, 24(3), pp. 319-325.

[10] Phillips, M., 1980, "A Force Balance Model for Particle Entrainment into a Fluid Stream," J. Phys. D, 13, pp. 221–233.

[11] Zeinali, H., Toma, P., and Kuru, E., 2012, "Effect of Near-Wall Turbulence on Selective Removal of Particles from Sand Beds Deposited in Pipelines," Journal of Energy Resources Technology, 134, pp. 021003-1 to 021003-9.

[12] Sil Industrial Minerals Inc., "Play Sand," Product Cataloge.

[13] H. Garcia, 2008, “Sedimentation Engineering: Processes, Measurements, Modeling and Practice”, American Society of Civil Engineers

[14] Wyatt, N.B., Gunther, C.M., and Liberatore, M.W., 2011, “ Drag reduction effectiveness of dilute and entangled xanthan in turbulent pipe flow,” J. Non-Newtonian Fluid Mech, 166, 25–31.

[15] Malvern Instruments Limited, 2005, “Bohlin C-VOR,” Product Catalogue.

[16] Kund, P. and Cohen I., 2008, “Fluid Mechanics, Fourth Edition,” Elsevier.

7 CONCLUSION AND FUTURE WORK

7.1 Conclusions

7.1.1 Turbulent Flow of Water in Horizontal Concentric Annuli

The following are the main conclusions from the study of turbulent flow of water in horizontal concentric annulus using particle image velocimetry (PIV) technique:

- New data analysing the position of maximum velocity and zero shear stress in concentric annular turbulent flow is provided to the literature in order to answer if both location coincide or not. This data is highly reliable since it agrees very well with previous experimental data obtained by using different measurement technique (hot wire anemometry).
- Additionally, experimental results were provided to analyse the shear production and viscous dissipation terms of the turbulent kinetic energy budget as well as the vorticity and root mean square (rms) of vorticity, which have not been extensively studied in the past for the concentric annular flow case.
- Axial mean velocity profile for the flow of water in the horizontal concentric annulus was found to be following the universal wall law in the viscous sub-layer ($y^+<10$).
- In the logarithmic zone ($y^+>30$), the axial velocity profile is close to the log wall ($u^+=2.5y^++5.5$). However, the best match is obtained for the highest Reynolds number used. Axial mean velocity values measured near outer pipe wall were found to be slightly higher than that of the ones measured near the inner pipe wall due to the transverse curvature effect.

- Unlike pipe flow, the velocity profile in the whole annular space is asymmetric. The radial position of maximum velocity was found to be placed closer to the inner pipe wall.
- The total shear stress profile was found to be curvilinear and asymmetric. Zero shear stress locations were placed closer to the inner wall for all the Reynolds numbers studied.
- No significant changes in the zero shear stress and maximum velocity locations were observed by varying the Reynolds number.
- Zero shear stress and maximum velocity locations were found to be different (± 0.5 mm). This difference varied from 1.3 to 3.3% . On average, the difference was 2%. Additionally, the zero shear stress location was found to be closer to the inner wall than that of the maximum velocity location.
- Axial and radial rms fluctuation velocities were found to be higher at the outer wall than at the inner wall. This is attributed to the curvature effect, suggesting that more turbulent kinetic energy is supplied by the outer wall to the same volume of flow.
- Peak values of axial rms fluctuation velocity are located in the buffer zone between 10 and 14 wall units.
- Reynolds stresses in the vicinity close to the wall are very similar at both inner and outer walls. However, further away from the wall, higher Reynolds stress values are obtained at the outer wall. The total shear stress was found to be very similar in the viscous sub-layer ($y^+<10$) for both walls. After $y^+=10$ the total wall shear stress is larger in the outer wall cases.
- The averaged vorticity results show that the vorticity is higher in the vicinity close to the pipe walls. The maximum vorticity is achieved for all the cases in the

viscous sub-layer between 4 and 6 wall units. No significant difference in the vorticity values was found between the outer and inner wall results.

- Root mean square of vorticity results show that the maximum values of rms vorticity are located in the viscous sub-layer. Higher maximum rms vorticity values were obtained at the inner pipe wall than at the outer pipe wall suggesting that more burst/sweep motions related to stream-wise vortices exist at the inner wall and therefore, higher wall shear stress regions are present at the inner pipe wall. These results were also confirmed with the wall shear stress calculations using the measured frictional pressure drops, in which the wall shear stress obtained at the inner pipe wall was higher than that of the outer pipe wall.
- The shear production term of the turbulent kinetic energy budget was found to be higher at the outer wall than at the inner wall, confirming the results obtained from the rms fluctuation velocities. The peak values were located in the buffer zone between 10 and 14 wall units.
- Maximum values of viscous turbulent kinetic energy dissipation are observed to occur at the pipe wall. These maximum values were found to be higher at the outer wall than at the inner wall.

7.1.2 An Experimental Study of Drag Reduction Phenomenon in Horizontal Concentric Annuli Using Particle Image Velocimetry Technique

The following are the conclusions obtained from the experimental study of drag reduction phenomenon in horizontal concentric annulus:

- PHPA concentration was varied from 0.07% V/V to 0.12%V. Based on the pressure drop measurements and Reynolds stress analyses, the optimum polymer concentration was found to be 0.1%V/V.

- The axial mean velocity profile was found to be following the universal law of the wall ($u^+=y^+$) in the viscous sub-layer ($y^+<10$) for both water and polymer fluid flow.
- In the logarithmic zone, the velocity profile was found to be following the log law ($u^+=2.5\ln(y^+)+5.5$) for water flow. However, in the polymer flow case, although the velocity profile remained logarithmic, it has higher slope than that of velocity profile of water, showing the drag reduction effect due to polymer addition.
- Comparison of the dimensionless velocity profile in the log-wall region near the inner and outer pipe walls shows that the velocity profile near the inner pipe wall has higher slope than that of the one near the outer pipe wall. This suggests that more drag reduction is taking place close to the inner pipe wall than the outer pipe wall.
- The thickness of the buffer zone for polymer fluid flow was much higher than that of observed in water flow.
- The drag reduction is enhanced by the increasing Reynolds number. The maximum drag reduction (26%) was obtained at the highest solvent Reynolds number studied (Res=56400).
- The effect of Reynolds number on the drag reduction was also proven by analyzing the velocity profile at different Reynolds numbers. The velocity profile in the logarithmic zone was shifted up (i.e., increasing slope) as the solvent Reynolds number was increased, indicating that the drag reduction was enhanced.
- Reynolds stresses were found to be reduced in the core flow region by the increasing polymer concentration. However, in the region close to the wall ($y^+<10$), no more reduction in the Reynolds stress was observed when the

polymer concentration exceeds the optimum value of concentration (0.1% V/V). This also explains, why above the optimum value of polymer concentration, more wall shear stress was present (since more viscosity is obtained at higher concentrations), and therefore no additional drag reduction was observed.

- In the viscous sub-layer, the Reynolds stresses were reduced to a value close to zero. The peak values obtained for water flow are significantly higher than that of the polymer fluid flow. Comparing the peak locations, it can be seen that the peak locations are closer to the wall in the polymer fluid flow. Moreover, higher Reynolds stresses are encountered at the outer pipe wall in both water and polymer fluid flow.
- A significant decrease in the radial turbulent intensities was observed as a result of adding drag reducer to the flow, which makes the flow more rectilinear. A greater decrease in the turbulent radial intensities was obtained at the inner pipe wall than at the outer pipe wall.
- The turbulent axial intensities were found to be almost the same in the region very close to the wall ($y^+<10$) for both water and polymer fluid flow. However, the axial rms velocity values obtained were higher for the polymer fluid flow between 10 and 60 wall units. Additionally, higher peaks values of axial intensities were obtained for the polymer fluid flow.
- The fluctuating velocity fields demonstrate that the addition of polymer to the flow results in dampening of the small scale motions and radial fluctuations, which produces an important effect on the near wall activities producing turbulence. The sweeps and bursts seen for the polymer fluid flow were less chaotic and less frequent than that of the water flow. These reductions affect the Reynolds stress, which is decreased significantly.

- Vorticity analyses show that the vorticity in water flow is very similar at both inner and outer walls. As polymer is added to the flow, the vorticity is reduced considerably. However, the vorticity reduction is higher at the inner wall. The vorticity is reduced almost to zero in both water and polymer fluid flow away from the wall.
- Rms of vorticity values show that lower rms vorticity is obtained in the drag reduction fluid flow case than that of the water flow case showing the drag reduction effect. In the water flow case, the rms vorticity values are lower at the outer wall than at the inner wall. Therefore, lower wall shear stress is expected at the outer wall. However, after adding polymer to the flow, the rms of vorticity is smaller at the inner wall and consequently, lower wall shear stress is expected at the inner wall. This also proved that more contribution to the overall drag reduction is supplied by the inner wall.
- The viscous dissipation and the shear production terms of the kinetic energy budget show a significant decrease after adding polymer to the flow. However, the higher decrease was obtained in the production term due to the great reduction in the Reynolds stress.
- The peak locations of the production term were found to be in the buffer zone, showing that the major changes in turbulence take place in the buffer zone. Moreover, both terms presented higher peak values at the outer wall, which demonstrates that more energy is produced and dissipated at the outer wall.
- Finally, it can be concluded that less energy is dissipated by the route of turbulence when drag reduction additives are supplied to the flow.

7.1.3 A Comparative Study of Solids Transport Performance - Water Versus Drag Reducing Fluids.

The main conclusions obtained from the experimentally study of solids transport performance of water and drag reducing fluids are summarized as follows:

- As compared to particle transport with water, significantly higher critical velocities were required when transporting particles by drag reducing fluids. This is because the viscous sub-layer thickness (where the local velocities are low) is higher in drag reducing fluid flow than that of water flow, reaching a value larger than the size of the particles used. Therefore, higher bulk velocities are required to reduce the viscous sub-layer thickness to the same order of magnitude of the particles in order to expose the particles to higher local velocities, which would be strong enough to initiate particle movement. Additionally, higher critical velocities were required after increasing the polymer concentration.
- In the water flow case, higher critical velocities to initiate particle movement in rolling were obtained for the coarser particles than that of the finer particles. This is because of the fact that even though for particle diameters larger than the viscous sub-layer thickness, the particle will be in the outer region (Logarithmic zone) facing higher velocities, the change in the local velocity does not compensate the increase in the mass of the particle (weight of the particle is proportional to the cube) and therefore, in this case the critical velocity required to commence particle movement is higher for the larger particle diameters.
- In the polymer fluid flow cases, lower critical velocities to initiate particle movement were obtained for the coarser particles. This is because when using drag reducing fluids as carrier fluids, the viscous sub-layer thickness is increased reaching a value larger than both of the particle sizes used. Therefore, the viscous

sub-layer thickness need to be reduced to the same order of magnitude of the particle diameter, so that the particle can be exposed to higher local velocities, which would be strong enough to commence particle movement. The viscous sub-layer thickness can be reduced by increasing the fluid flow rate. Therefore, in the large particle size case, the flow rate required to reduce the viscous sub-layer thickness to the same order of magnitude of the particle diameter is lower than that of the smaller particle diameter case.

- Pressure drop versus fluid velocity results shows that the slope obtained is different at each flow pattern. The changes in the slope allow us to identify the transition between different modes of solids transport. These results confirm the results obtained by the video camera.
- Solids removal performance seems to be better in the water flow case than in the polymer fluid flow. The critical velocity (and hence, the associated frictional pressure drop) of initiation of particle rolling is much lower in the case of water than that of polymer flow. For instance, at a bulk fluid velocity of 1 m/s, when we use polymer fluid, particles are transported in dunes/saltation mode. When we use water, however, the particles are transported in full suspension at a bulk velocity of 1 m/s. Therefore, a faster cleaning process is expected to occur in the water flow case. However, it may not be possible to transport the cuttings in full suspension all the time, especially when cleaning long horizontal and extended reach wells where the frictional pressure drops encountered could be extremely high. Under these circumstances, it is required to minimize the frictional pressure drops in order to avoid operational problems such as exceeding the pump capacity or fracturing the formation, therefore, particle transport in dunes/saltation mode (yielding the lower pressure drop) would be more feasible.

- Lower pressure losses are anticipated when transporting particles with polymer as compared to water. Moreover, when we compare the net transport velocity of dunes using the finer particles, we see that higher net transport velocities are achieved when using polymer fluids than that of with water. In other words, for the same transport mode of cuttings (let's say, saltation/dunes mode) cuttings can be transported much faster with polymer fluid than that of with water. As long as we do not exceed the operational limits (i.e., pump pressure capacity, formation fracture pressure, etc.), hole cleaning can be achieved in shorter time by using polymer fluid. Faster net transport velocity means shortened hole cleaning time which might help reducing the cost associated with hole cleaning operations routinely conducted in horizontal and extended reach wells.
- When transporting the coarser particles, net transport velocities of dunes were found to be higher in water than that of polymer fluids. This is in contrast to what we observed in experiments with small particle diameter range where the polymer fluid caused the highest net transport velocity. This is because in the small particle range dunes were obtained in water at low flow velocities $0.26 < U_b < 0.5$ m/s whereas in large particle range dunes were obtained for water at high flow velocities $0.3 < U_b < 0.91$ m/s.
- In the polymer fluid flow cases, solid removal performance is much better for coarser particles than that of finer particles. For example at bulk fluid velocity around 1 m/s, the net transport velocity of dunes obtained for the finer particles is around 0.001 m/s in both polymer fluids; however, in the coarser particles the net transport velocity of dunes at this bulk fluid velocity is much higher, being around 0.016 m/s. This is because at this bulk fluid velocity, the larger particles are more likely to stick out from viscous sub layer (where the local velocities are

low) and get exposed to higher fluid velocities within the logarithmic zone away from the wall.

- Dunes were transported at higher velocities with 0.07% V/V polymer fluid as compared to 0.1% V/V polymer fluid.

7.2 Future Work

in chapter 4 and 5, it was showed that the experimental results obtained using the PIV technique agree very well with results presented in previous experimental and simulation studies. This proves that PIV can be successfully implemented to analyze turbulent flow through concentric annulus. Therefore, further studies such as analyzing the effect of varying the inner to outer radius ratio and eccentricity of the pipes on the velocity profiles, position of maximum velocity and nature of the turbulence can be performed. Also, 3D PIV may be used to have a complete understanding of the topic.

In chapter 5, the optimum concentration of drag reducer, which was the concentration yielding to the lowest encountered pressure drop, was found to be 0.1% V/V. However, it can also be seen that the difference in drag reduction between the 0.1 and 0.07% V/V polymer fluid flow is not bigger than 4%. On the other hand, better solids removal was obtained for the 0.07% V/V drag reducing solution than that of the 0.1% V/V drag reducing solution as shown in chapter 6. Therefore, it is required to test lower drag reducer concentrations in order to find a concentration that still can provide a significant drag reduction and that also might result more effective in terms of the solids removal performance for the two specific particle diameters studied.

In chapter 6, it was shown that for drag reducer fluid flow cases, the solids transport performance obtained was more efficient for coarser particles than that of finer particles. Additionally, in chapter 5, a comparison between the velocity profiles obtained for water

and drag reducing solutions shows that after exceeding the viscous sub-layer region, the local velocities obtained in drag reducing fluid flow are significantly higher than that of water flow. For instance, for particle diameters of around 3 mm, it can be guaranteed that the particles will be either in the buffer zone or in the logarithm zone for both water and drag reducing flow. Consequently, as explained before, at these locations higher local velocities are obtained using drag reducing fluid flow than that of water flow, and therefore lower critical velocities to initiate particle movement in rolling are expected when using drag reducing fluid as carrier fluid. Higher net transport velocities of dunes can also be expected using polymer fluid as carrier fluid for the particle size rages suggested. In addition, the pressure drop reduction obtained can be as high as 42%. Consequently, transport experiments should be performed using bigger particle diameter ranges than the ones used in this research.